Structural and Biophysical Characterization of the Bacterial Homospermidine Synthase from *Blastochloris viridis* to Provide Insights into Substrate Recognition and Reaction Mechanism

Dissertation

Zur Erlangung des akademischen Grades
Doktor der Naturwissenschaften
(Dr. rer. nat.)
der Mathematisch-Naturwissenschaftlichen Fakultät
der Christian-Albrechts-Universität zu Kiel

Vorgelegt von

Sebastian Krossa

Kiel, 2015

Referent:	Prof. Dr. Axel Scheidig
Koreferent:	Prof. Dr. Dietrich Ober
Tag der Verteidigung:	07.09.2015
Zum Druck genehmigt:	_____

Erklärung

Hiermit erkläre ich, dass ich bis zum heutigen Tage weder an der Christian-Albrechts-Universität zu Kiel noch an einer anderen Hochschule ein Promotionsverfahren endgültig nicht bestanden habe oder mich in einem entsprechenden Verfahren befinde. Ich erkläre, dass die Abhandlung nach Inhalt und Form die eigene Arbeit ist und dass ich die Inanspruchnahme fremder Hilfen aufgeführt habe sowie, dass ich die wörtlich oder inhaltlich aus anderen Quellen entnommenen Stellen als solche gekennzeichnet habe. Ich erkläre, dass diese Arbeit weder ganz noch zum Teil schon einer anderen Stelle im Rahmen eines Prüfungsverfahrens vorgelegen hat. Ich erkläre, dass die Arbeit unter Einhaltung der Regeln guter wissenschaftlicher Praxis der Deutschen Forschungsgemeinschaft entstanden ist.
Kiel, den

Danksagung

Ich bedanke mich herzlich bei allen, die mich im Laufe dieser Arbeit sowie während meiner “Doktoranden-Zeit” unterstützt und zu deren Erfolg beigetragen haben:
Axel Scheidig - Vielen Dank für das Thema meiner Arbeit und die stetige Unterstützung und Förderung während der gesammten Zeit meiner Arbeit sowie die Ermöglichung und Förderung des paralellen “Akirin-Projekts”!
Dietrich Ober - Vielen Dank für das Projekt und die tolle Kooperation und Unterstüzung!
Janka Held-Feindt - Vielen Dank für die gesamte Förderung und Unterstützung bei dem “Akirin-Projekt”.
Annette Faust - Vielen Dank für die Unterstützung, insbesondere bei diversen Messzeiten an den Synchrotrons, Kristallization und Datenprozessierung
Christoph Plieth - Vielen Dank für die Unterstützung, insbesondere bei “Labor-Basteleien” in Form von Ratschlägen und “Bastel-Material”.
Meinen “Mit-Doktoranden” und (ehemaligen) Kollegen mit denen ich teils viel Zeit im Labor und/oder an den Beamlines verbracht habe möchte ich danken für ein produktives, kooperatives und freundschaftliches Arbeitsumfeld: Chrissy, Christian, Julia, Leslye, Livia, Monika, Renato, Sonja H., Sonja V., Susi, Uli.
Brigitte Schemmerling aus der AG Ober danke ich für die Durchführung der HSS-Aktivitäts-Tests.
Vielen Dank die Mitarbeiter der AG Held-Feindt, Brigitte Rehmke, Fereshteh Ebrahim und Jörg Krause, für die gesamte Förderung und Unterstützung bei dem “Akirin-Projekt” sowie an die Familie Mehdorn Stiftung für die finanzielle Förderung des “Akirin-Projekts”.
Ein ganz besonderer Dank gilt meiner Familie, die mich immer verständnisvoll unterstützt hat. Meiner Mutter und Schwiegermutter danke ich besonders für die Betreuung meines Sohnes während der letzen Phase dieser Arbeit. Veronica danke ich von ganzem Herzen für ihr Verständnis, ihre Unterstützung, Hilfe, Motivation und Diskussionen!!

0.1 Zusammenfassung

Die hochkonservierte bakterielle Homospermidin Synthase (HSS) ist ein Schlüsselenzym des Polyamin-Metabolismus vieler α-, γ-, und δ-Proteobakterien, wie beispielsweise den pathogenen Stämmen *Legionella pneumophila* und *Pseudomonas aeruginosa* und ist daher ein potentielles Ziel für neue Antibiotika. Die HSS aus *Blastochloris viridis* (*Bv*HSS) diente als Modell für die bakterielle HSS Familie in der hier vorgestellten detaillierten Analyse mehrerer Kristallstrukturen, u.a. mit gebundenem Substrat oder Inhibitor. Anhand dieser konnte eine tiefe Tasche identifiziert werden, welche zwei Substrat Bindestellen enthält, von denen eine hoch spezifisch für Putrescin ist. *Bv*HSS enthält eine Seitentasche in direkter Nähe zum aktiven Zentrum, welche aus konservierten Aminosäuren aufgebaut ist. Zudem ist ein potentieller Substrat Diskriminierungs-, Leit- und Detektionsmechanismus vorhanden. Anhand der Strukturen konnte die bekannte Substratspezifität bzw. Substratpräferenz sowie den aus diesen resultierenden Produkten der bakteriellen HSS auf struktureller Ebene erklärt werden. Die beschriebene kompetitive Hemmung der bakteriellen HSS durch 1,3-Diaminopropan konnte auf struktureller Ebene nachvollzogen werden. Die von den Strukturen abgeleitete Hypothese der detaillierten Reaktionsschritte legt eine Rolle des konservierten Tryptophans Trp-229 als Stabilisator hoch energetischer Übergangszustände durch Kation-π Interaktion nahe. Zusammenfassend vermitteln diese Erkenntnisse erstmals ein detailliertes Verständnis des Aufbaus der Bindetasche sowie der Funktionsweise der bakteriellen HSS auf struktureller Ebene und ermöglichen somit eine gezielte Wirkstoffentwicklung.

0.2 Abstract

The highly conserved bacterial homospermidine synthase (HSS) is a key enzyme of the polyamine metabolism of many α-, γ-, and δ-proteobacteria and, in particular, of that of pathogenic strains such as *Legionella pneumophila* and *Pseudomonas aeruginosa*; HSS might thus serve as a target for new antibiotic drugs. As a model for the bacterial HSS family, various crystal structures of *Blastochloris viridis* HSS (*Bv*HSS), including substrate and inhibitor bound structures, have allowed a detailed analysis of an identified deep cavity, including two substrate binding sites at the active site, one of which is highly specific for putrescine. *Bv*HSS features a side pocket in the direct vicinity of the active site formed by conserved amino acids and a potential substrate discrimination, guiding, and sensing mechanism. The structural basis for the reported substrate specificity and preference and their respective products could be determined. Additionally, the competitive inhibition by 1,3-diaminopropane could be explained on the structural level. The derived hypothesis of the detailed reaction steps for the catalysis of *Bv*HSS emphasizes cation-π interaction through the conserved residue Trp-229 as a key stabilizer of high energetic transition states. In conjunction, these results provide for the first time detailed insights into the structure of the binding pocket and the function of the bacterial HSS, thereby allowing a rational drug design.

Contents

List of Figures

List of Tables

0.3 Abbreviations

3D three dimensional

4MCHA trans-4-methylcyclohexylamine

AIH agmatine deiminase/amidohydrolase

AbeAdo 5'([(Z)-4-amino-2-butenyl]methylamino)-5'deoxy-adenosine

ADC arginine decarboxylase

AdoDATAD S-adenosyl-1,12-diamino-3-thio-9-azadodecane

AdoDATO S-adenosyl-1,8-diamino-3-thioactane

AGM agmatine

APAO acetylpolyamine oxidase

APCHA N-(3-aminopropyl)cyclohexylamine

***Bv*HSS** *Blastochloris viridis* HSS

CA(N)SDC carboxy(nor)spermidine decarboxylase

CA(N)SDH carboxy(nor)spermidine dehydrogenase

CAD 1,5-diaminopentane

CC correlation coefficient

cDNA complementary DNA

***Cs*GluDH** *Clostridium symbiosium* GluDH

CV column volumes

DABA DC L-1,4-diaminobutyrate decarboxylase

DAP 1,3-diaminopropane

dcSAM decarboxylated S-adenosylmethionine

ddH2O double-distilled water

DFMO 2-difluoromethylornithine

DHS deoxyhypusine synthase

GluDH glutamate dehydrogenase

HRV3C human rhinovirus 3C

HSP *sym*-homospermidine

HSS homospermidine synthase

IMAC immobilized metal ion affinity chromatography

IPTG isopropyl β-D-1-thiogalactopyranoside

MGBG Methylglyocal bis(guanyhydrazone)

***Mg*SacDH** *Magnaporthe grisea* saccharopine dehydrogenase/reductase

MR molecular replacement

NCPAH N-carbamoylputrescine amidohydrolase

NDSB-201 3-pyridin-1-ium1yl-propane-1-sulfonate

NSPD norspermidine

NTA nitrilotriacetic acid

OD_{6}00 optical density/absorbance at 600 nm

ODC ornithine decarboxylase

PCR polymerase chain reaction

PDB Protein Data Bank

PUT putrescine

RMSD root-mean-square distance

RSCC real space correlation coefficient

RSRZ resolution normalized real space R-values

SA simulated annealing

SAM S-adenosylmethionine

SAM486A/CGP48664 4-amidinoindan-1-one-2'-amidinhydrazone

SAMDC S-adenosylmethionine decarboxylase

SHR saccharopine

SMO spermine oxidase

SPD spermidine

SPDSyn spermidine synthase

SPN spermine

SPNsyn spermine synthase

SSAT spermidine/spermine-N1-acetyltransferase

1 Introduction

1.1 Polyamines and Polyamine Biosynthesis

Polyamines are small ubiquitous polycationic molecules essential for cell functioning, growth, proliferation, and apoptosis. They are found in nearly all living species (Di Martino *et al.*, 2013; Hamana *et al.*, 2007; Pegg, 2009). The prominent triamines (Fig. 1.1 b) in bacteria are *sym*-homospermidine (HSP), spermidine (SPD) and *sym*-norspermidine (NSPD) (Hamana and Matsuzaki, 1992; Hamana *et al.*, 2007; Hamana and Takeuchi, 1998). Eukaryotes generally utilize SPD or spermine (SPN) (Pegg, 2009).

1.1.1 1,3-Diaminopropane, Putrescine and Cadaverine Synthesis

1,3-Diaminopropane (DAP) is formed by decarboxylation of L-2,4-diaminobutyric acid via L-2,4-diaminobutyrate decarboxylase (DABA DC, EC 4.1.1.86). In a similar manner, cadaverine (CAD) is formed from L-lysine via L-lysine decarboxylase (EC 4.1.1.18). Putrescine (1,4-diaminobutanal, PUT, see Fig. 1.1) is a precursor for the triamine synthesis and is either formed by the ornithine decarboxylase (ODC, EC 4.1.1.17) or the arginine decarboxylase (ADC, EC 4.1.1.19) pathway. PUT can be directly generated from L-ornithine via ODC. Three species-dependent pathways are known for the generation of PUT from L-arginine, thereby decarboxylation to agmatine (AGM) via ADC is the first step in all pathways. Subsequently, AGM can be further processed by agmatine deiminase/amidohydrolase (AIH, EC 3.5.3.12) in order to yield N-carbamoylputrescine. In the following step, N-carbamoylputrescine can either be hydrolyzed by N-carbamoylputrescine amidohydrolase (NCPAH, EC 3.5.1.53) to form PUT, or converted by PUT transcarbamylase to form PUT. Alternatively, AGM can be hydrolyzed to PUT and urea by agmatinase (EC 3.5.3.11) (Pegg and Casero, 2011; Schneider and Wendisch, 2011).

1.1.2 Norspermidine, Spermidine and Spermine Synthesis

Mammalian cells, most eukaryotes, and many bacterial phyla synthesize SPD and SPN (Hanfrey *et al.*, 2011). SPD is synthesized by spermidine synthase (SPDSyn, EC 2.5.1.16) utilizing PUT and decarboxylated S-adenosylmethionine (dcSAM) generated from S-adenoslymethionine (SAM) by S-adenosylmethionine decarboxylase (SAMDC, EC 4.1.1.50). Subsequently, SPN can be formed by spermine synthase (SPNSyn, EC 2.5.1.22) from SPD again using dcSAM as aminopropyl-group donor (Pegg, 2009). Interconversion of SPN to SPD is possible via spermine oxidase (SMO, EC 1.5.3.16), generating SPD from SPN. Additionally, SPD and PUT can be formed from conversion of SPN or SPD to N1-acetylspermine or N1-acetylspermidine through spermine/spermidine-N1-acetyltransferase (SSAT, EC 2.3.1.57) and followed by the formation of SPD or PUT by acetylpolyamine oxidase (APAO, EC 1.5.3.13) (Pegg and Casero, 2011; Schneider and Wendisch, 2011).

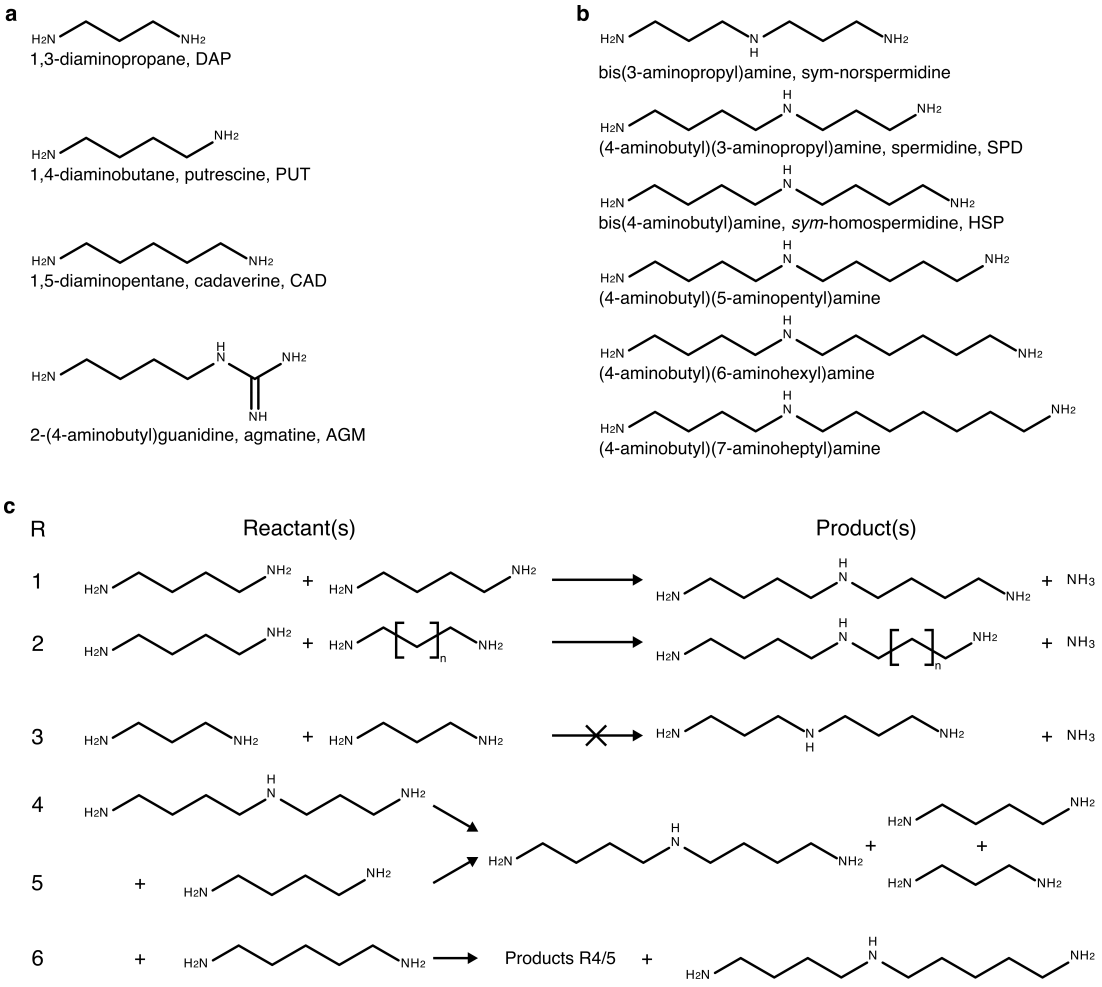

Figure 1.1: Overview of bacterial HSS-related polyamines and bacterial HSS-catalyzed reactions. (a) Two-dimensional structures of diamines (DAP, PUT, CAD) and agmatine (AGM). (b) Two-dimensional structures of triamines. (c) Known net reactions of the bacterial HSS (Ober et al., 1996): Reaction 1: HSP formation from 2 PUT; reaction 2: general triamine formation from PUT and a second diamine (with n=[1..5]); reaction 3: bacterial HSS does not produce sym-norspermidine from 2 DAP; reaction 4: HSP, DAP, and PUT formation from SPD; reaction 5: HSP, DAP, and PUT formation from SPD and PUT; reaction 6: (4-aminobutyl)(5-aminopentyl)amine, HSP, DAP, and PUT formation from SPD and CAD.

In bacteria known to produce SPD, for example in almost all ε-proteobacteria (Hamana and Matsuzaki, 1992; Hamana *et al.*, 2007; Hamana and Takeuchi, 1998), an alternative SPD biosynthetic pathway exists (Hanfrey *et al.*, 2011; Lee *et al.*, 2009; Tait, 1976). Lacking both SAMDC and SPNSyn, these bacteria utilize orthologs of carboxy(nor)spermidine dehydrogenase (CANSDH/CASDH, also annotated as saccharopine dehydrogenase, EC 1.5.1.43) and carboxy(nor)spermidine decarboxylase (CANSDC/CASDC, EC 4.1.1.96) to produce SPD or NSPD from PUT (Hanfrey *et al.*, 2011; Lee *et al.*, 2009). Whether SPD or NSPD will be produced, supposedly depends on the presence of the necessary enzymes in the bacterial strain to produce the NSPD precursor DAP from L-1,4-diaminobutyric acid or to produce the SPD precursor PUT via the ODC- or ADC-pathway (Hanfrey *et al.*, 2011; Lee *et al.*, 2009). SPD or NSPD is formed by attaching L-aspartatic-β-semialdehyde to either PUT or DAP by CANSDH/CASDH followed by a decarboxylation through CANSDC/CASDC (Hanfrey *et al.*, 2011; Lee *et al.*, 2009). Some extremophile bacteria that produce SPD use agmatine aminopropyltransferase (EC 2.5.1.104) to form N1-aminopropylagmatine from AGM and dcSAM. N1-aminopropylagmatine is hydrolyzed to SPD and urea by aminopropylagmatine ureohydrolase (EC 3.5.3.24) (Morimoto *et al.*, 2010; Ohnuma *et al.*, 2005).

1.1.3 Homospermidine Synthesis

HSP-containing bacteria, mostly α- as well as some γ- and δ-proteobacteria (Hamana and Matsuzaki, 1992; Hamana *et al.*, 2007; Hamana and Takeuchi, 1998), synthesize 1 mol HSP from 2 mol PUT via the enzyme homospermidine synthase (HSS, EC: 2.5.1.44) (Tait, 1979). The bacterial HSS is highly conserved and is proposed to be evolutionary related to carboxy(nor)spermidine dehydrogenase (CA(N)SDH, EC: 1.5.1.43) (Shaw *et al.*, 2010). Plants that produce HSP as an intermediate in pyrrolizidine alkaloid biosynthesis use an HSS (EC: 2.5.1.45) that evolved from deoxyhypusine synthase (DHS) after gene duplication (Kaltenegger *et al.*, 2013; Ober and Hartmann, 1999c; Reimann *et al.*, 2004). DHS is known to produce HSP as a side reaction (Ober and Hartmann, 1999a). In contrast to bacterial HSS, the HSS from plants and the DHS are not capable of producing HSP solely from PUT. Both enzymes depend on SPD as a 4-aminobutyl group donor to produce HSP together with PUT (Ober and Hartmann, 1999c; Park *et al.*, 2003). Some HSP-producing bacteria strains do not possess *hss* orthologs but potential *dhs* orthologs. In analogy to plant DHS or plant HSS, these proteins are thought to function as homospermidine synthase (Shaw *et al.*, 2010).

1.2 Characteristics of the Bacterial Homospermidine Synthase

A distinct feature of the bacterial HSS is its use of NAD(H) as a prosthetic group, which functions as a hydride acceptor and donor during the two-step reaction (Böttcher *et al.*, 1994). Bacterial HSS has been found to be active at neutral to basic pH with an optimum at pH 8.7 to 9 (Ober *et al.*, 1996; Yamamoto *et al.*, 1993). HSS from some but not all species are

potassium-dependent with an optimum of, for example, 50 mM for *Blastochloris viridis* HSS (*Bv*HSS) (Ober *et al.*, 1996; Yamamoto *et al.*, 1993). The enzyme is capable of catalyzing side reactions to produce a variety of N-aminobutyl-linked triamines utilizing PUT together with respective linear diamines with C3 to C7 carbon chains (see Fig. 1.1) (Ober *et al.*, 1996). The bacterial HSS can produce HSP from SPD as its sole substrate (Böttcher et al., 1994). 1,3-diaminopropane (DAP) is the only known diamine functioning as a strong competitive inhibitor of bacterial HSS (Ober *et al.*, 1996; Tait, 1979; Yamamoto *et al.*, 1993). The activity of bacterial HSS in producing HSP is slightly reduced under the administration of PUT together with either 1-aminopropane, 1-aminobutane, 1,2-diaminoethane, 1,5-diaminopentane (CAD), 1,6-diaminohexane, 1,7-diaminoheptane, or SPD (Ober *et al.*, 1996; Yamamoto et al., 1993). The bacterial HSS can produce HSP from SPD as sole substrate (Böttcher *et al.*, 1994), but is not capable to produce NSPD or bis(5-aminopentyl)amine from DAP or CAD respectively (Ober *et al.*, 1996; Yamamoto *et al.*, 1993).

1.3 Inhibitors of Polyamine Biosynthesis Pathways

Because the polyamines are essential to all living species, the enzymes of their biosynthetic pathways have been in the focus of the search for new targets in anti-microbial and anti-cancer therapies for quite some time now. A lot of inhibitors have been generated, mostly specifically targeting single enzymes of the SPD/SPN biosynthesis pathway via SAMDC and SPDSyn/SPNSyn (Wallace and Fraser, 2004). Many of them have been tested in anti-cancer therapy targeting the enzymes ODC and SAMDC and some are clinically approved (Casero and Marton, 2007; Nowotarski *et al.*, 2013). Some of these agents are:

- 2-difluoromethylornithine (DFMO) is a well-studied and clinically approved irreversible inhibitor of ODC resulting in decreased intracellular PUT and SPD levels (Casero and Marton, 2007; Metcalf *et al.*, 1978). DMFO could also effectively decrease PUT, thereby lowering HSP levels in the α-proteobacteria *Rhizobium leguminosarum* (Shaw *et al.*, 2010).
- Methylglyocal bis(guanyhydrazone) (MGBG), 4-amidinoindan-1-one-2'-amidinhydrazone (SAM486A/CGP48664) and 5'([(Z)-4-amino-2-butenyl]methylamino)-5'deoxy-adenosine (AbeAdo) are competitive (MGBG and SAM486A/CGP48664) or irreversible (AbeAdo) inhibitors of SAMDC, which both cause decreasing levels of SPD and SPN, while increasing levels of PUT (Byers *et al.*, 1993; Porter *et al.*, 1980; Regenass *et al.*, 1994).
- S-adenosyl-1,8-diamino-3-thioactane (AdoDATO, "transition-state analogue inhibitor") and trans-4-methylcyclohexylamine (4MCHA, competitive at PUT binding-site) are inhibitors of SPDSyn, which both cause decreasing levels of SPD, while increasing levels of PUT and SPN (Beppu *et al.*, 1995; Holm *et al.*, 1989; Pegg *et al.*, 1982).
- S-adenosyl-1,12-diamino-3-thio-9-azadodecane (AdoDATAD) and N-(3-aminopropyl)cyclohexylamine (APCHA, competitive at SPD-binding site) are inhibitors of

SPNSyn that lead to decreasing levels of SPN and PUT while increasing levels of SPD (Beppu *et al.*, 1995; Pegg *et al.*, 1989).

There are no specifically designed inhibitors available that target the bacterial HSS. DAP is the only known diamine that functions as a strong competitive inhibitor of bacterial HSS (Ober *et al.*, 1996; Tait, 1979). Bacterial HSS activity to produce HSP was slightly reduced under administration of PUT together with either 1-aminopropane, 1-aminobutane, 1,2-diaminoethane, CAD, 1,6-diaminohexane and 1,7-diaminoheptane or SPD (Ober *et al.*, 1996; Yamamoto *et al.*, 1993).

1.4 Bacterial HSS as Target for New Antibiotic Drugs

The bacterial HSS is present in many α-, γ-, and δ-proteobacteria and, in particular, in pathogenic strains such as *Legionella pneumophila*, *Brucella* spp., and *Pseudomonas aeruginosa* (Shaw *et al.*, 2010). *P. aeruginosa* is an important cause of nosocomial and healthcare-associated infections and is especially challenging for immunocompromised individuals, such as infants in neonatal intensive care units (Jefferies *et al.*, 2012; Parkins *et al.*, 2010). This is problematic because of its low antibiotic susceptibility and its ability to acquire new antibiotic resistance (Zilberberg and Shorr, 2013). Increasing numbers of multidrug resistant pathogens in general raise the need for new antibiotic targets (Nikaido, 2009). The essential function of HSP for growth, in addition to the difference in the mechanism and evolution of its synthesizing enzymes in bacteria and eukaryotes, suggests that bacterial HSS represents such a potential target (Ober and Hartmann, 1999c; Shaw *et al.*, 2010). Furthermore, polyamines are crucial in bacteria-host interactions and are involved in bacterial pathogenesis. The import of host polyamines alters bacterial growth and activates mechanisms for the evasion or repression of the host immune system (Di Martino *et al.*, 2013; Shah and Swiatlo, 2008). As an example, the inactivation of the alternative SPD biosynthetic pathway involving bacterial HSS-related CANSDH in the pathogenic strain *Vibrio cholerea* leads to a reduction in growth rate and biofilm formation (Lee *et al.*, 2009), whereas polyamines improve the intracellular growth of *L. pneumophila* (Nasrallah *et al.*, 2011). To assess its potential as an antibiotic drug target, the reaction mechanism of bacterial HSS needs to be investigated in detail based on its three dimensional (3D) structure. The structure of the bacterial HSS from *L. pneumophila* has been solved at 2.5 Å, but with no bound substrate (PDB ID 2PH5 (Forouhar)). Nevertheless, the obtained structure does not provide enough data to illuminate the underlying reaction mechanism or its differences from DHS/plant HSS. This PhD thesis presents high-resolution structures of *Bv*HSS and variants with various bound polyamines, providing a detailed insight into bacterial HSS substrate-binding properties and function.

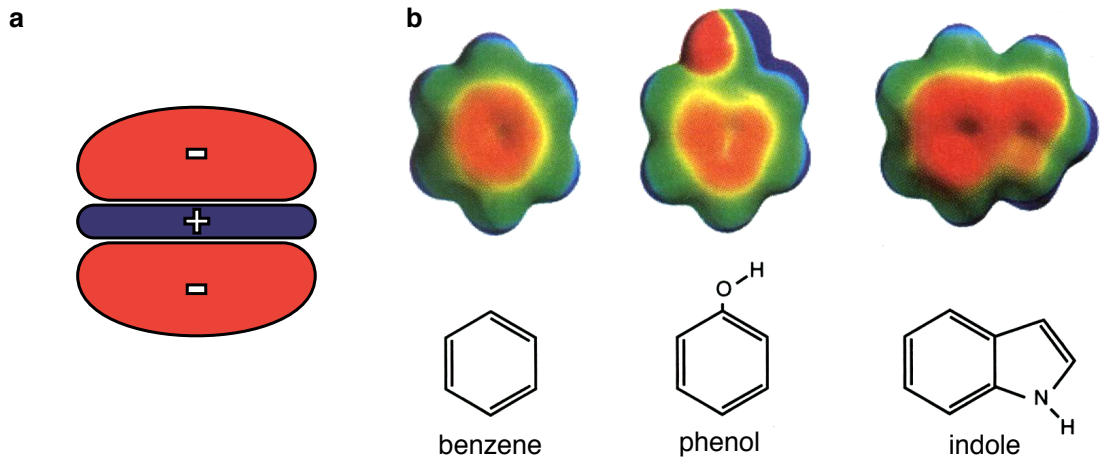

Figure 1.2: Charge distribution in aromatic rings. (a) Schematic of the quadrupole moment of benzene, viewed edge-on, showing regions of relative positive (blue) and negative (red) partial charge. (b) Electrostatic potential surfaces for benzene, phenol, and indole, the aromatic components of Phe, Tyr, and Trp, respectively. Values are calculated from ab initio 6-31 G** calculations and are color-coded from red (-25 kcal/mol) to purple (+25 kcal/mol). From Dougherty (1996). Reprinted with permission from AAAS.

1.5 Cation-π Interaction

The π electrons of aromatic rings are delocalized over all atoms forming the ring (as proposed by Kekulé in 1865). Thus, the electron density distribution can be modeled as a quadrupole charge distribution with a negatively charged area above and below, and a positively charged area in the plane of the planar ring as illustrated in Fig. 1.2 (Ma and Dougherty, 1997). These aromatic π systems allow for non-covalent interactions – the so-called π-interactions. The π system, like any negative charge, can electrostatically interact with a positive charge leading to a variety of π-interactions, like π-stacking, ion-π, and polar-π interaction (Raju *et al.*, 2011).

The cation-π interaction is the non-covalent interaction of the faces of the aromatic ring with a cation. The strength of this interaction is, depending on the orientation and environment, comparable to that of a salt bridge or a hydrogen bond (Gallivan and Dougherty, 2000). An increase in charge density of the cation is correlated with an increase in binding energy (Ma and Dougherty, 1997). The binding energy is affected by the solvent polarity – the highest energy is observed in the gas phase and decreases with increasing solvent polarity (Gallivan and Dougherty, 2000). The optimal position for a cation is centred over the ring with a distance dependence of $1/r^n$ where $n < 2$. Nevertheless, some off-centered positions can have significant binding energies (Dougherty, 1996; Marshall *et al.*, 2009). Additionally, the binding energy of benzene is modified through substituents – electron withdrawing substituents (-CN, -F) lower the binding energy, while electron donating substituents ($-NH_2$) raise the binding energy (Mecozzi *et al.*, 1996; Raju *et al.*, 2011). The cation-π binding energy of heteroaromates can be increased when the lone pair of the heteroatom contributes to the aromaticity, as in indol, and can be decreased in the opposite case, as in pyridine. The cation-π binding energy can be approximated

by using the electrostatic charge distribution instead of using complex calculations based on various intermolecular forces (Mecozzi *et al.*, 1996). In proteins, the cation-π interaction through Tyr, Trp and Phe are crucial for protein-protein interactions, substrate recognition and selectivity and are discussed to take part in enzyme catalysis (Dougherty, 2013).

1.6 Structure Determination of Proteins via X-ray Crystallography

The following sections give a brief introduction and overview of the structure determination of proteins by using X-ray crystallography. The method of molecular replacement (MR) used for phasing of all data sets presented in this PhD thesis, and its implications on biasing the phases are described in more detail in the subsection “Molecular Replacement” on page 10. All information subsequently presented, if not indicated otherwise, is based on textbook knowledge and can be found in detail in Rupp (2010).

1.6.1 X-ray Diffraction Basics

The basic principle of the structure determination of proteins via X-ray crystallography is the scattering of high energy electromagnetic radiation – the X-rays. Based on the wave-particle duality, the wave packet representing a single X-ray photon can induce oscillation in electrons within the coherence length of its electric field vector. This results in coherent circular emanating waves from the oscillating electrons, which – depending on the direction – constructively or destructively interfere to a scattered wave. Maximal constructive interference occurs at a phase difference of

$$\Delta\varphi_{max} = n \cdot 2\pi \tag{1}$$

with n being a positive integer. The phase difference between scattered waves is

$$\Delta\varphi = 2\pi\left(\mathbf{s}_0 - \mathbf{s}_1\right) \cdot \mathbf{r} = 2\pi\mathbf{S} \cdot \mathbf{r} \tag{2}$$

with the incoming wave vector $\mathbf{s}_0$, the outgoing wave vector $\mathbf{s}_1$, and the distance vector $\mathbf{r}$ between the origins of the outgoing waves. Combination of equations 1 and 2 lead to the Laue equations describing conditions for maximal constructive interference in a 3-dimensional crystal lattice (with **a**, **b**, and **c** as unit cell base vectors):

$$\mathbf{S} \cdot \mathbf{a} = n_1 \tag{3}$$

$$\mathbf{S} \cdot \mathbf{b} = n_2 \tag{4}$$

$$\mathbf{S} \cdot \mathbf{c} = n_3 \tag{5}$$

The probability of a scattered X-ray photon to appear in a certain direction is proportional to the amplitude of the scattered, superimposed wave in that direction. In total, all scattering events of

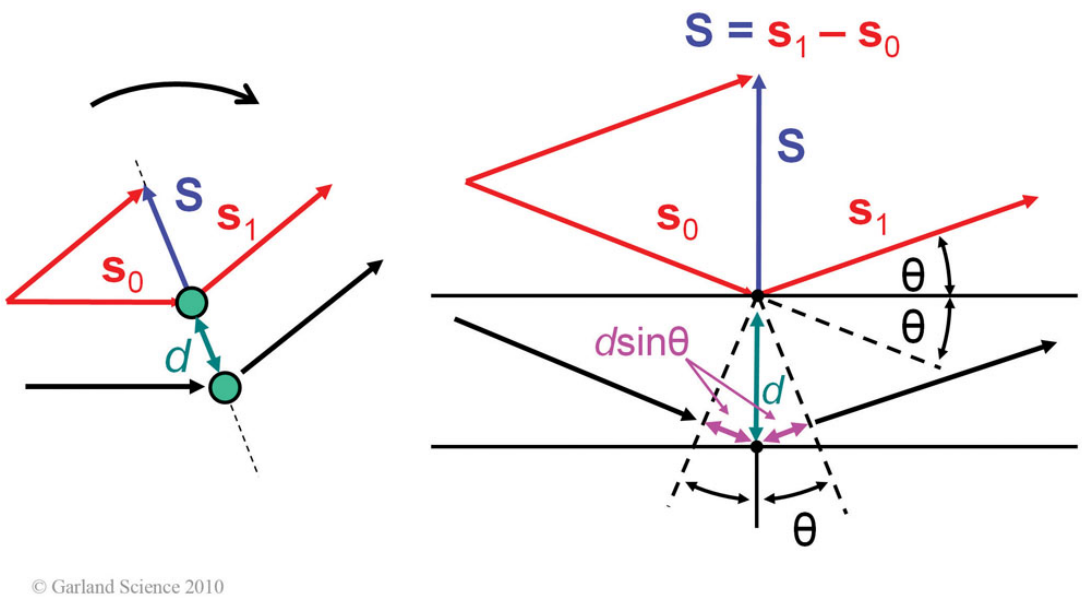

Figure 1.3: Illustration of the assumption of X-ray reflection on lattice planes of a crystal by Bragg leading to the Bragg equation. Reproduced with permission from Biomolecular Crystallography by Bernhard Rupp, ©2009-2014 Garland Science/Taylor & Francis LLC.

X-ray photons on the regular array of electrons of the atoms in protein crystals lead to a discrete scattering pattern – also named diffraction pattern. This diffraction can also be interpreted as reflection of X-rays on the lattice planes of the crystal. Based on this assumption, the Bragg equation describes the condition for maximal constructive interference (see also Fig. 1.3):

$$n\lambda = 2d_{hkl}\sin\theta \tag{6}$$

For maximum diffraction, the path difference, expressed as two times the interplanar distance d_{hkl} of the reflecting plane *hkl* multiplied with the sine of the scattering angle θ, must be an integer multiple (n) of the wavelength λ.

The scattering of a single atom can be described by the empirical approximation as proposed by Cromer and Mann (1968):

$$f_S^0 = \sum_{i=1}^{4} a_i e^{-b_i(\sin\theta/\lambda)^2} + c \tag{7}$$

The Cromer-Mann coefficients (a_i, b_i,and c) for each single atom are listed in the International Tables for Crystallography, IUCr (2006).

Superposition of the partial waves of the atoms of a molecule results in the molecular scattering function $\mathbf{F}_s$ with a relative phase of each partial wave as $\varphi = 2\pi\mathbf{S}\mathbf{r}_\mathbf{j}$, and each atomic scattering

factor as $f^0_{S,j}$

$$\mathbf{F_s} = \sum_{j=1}^{atoms} f^0_{S,j} \cdot e^{2\pi i \mathbf{S r_j}} \tag{8}$$

The scattering of a protein crystal is proportional to the scattering from the unit cell content, which can be described by the scattering function in Eq. 8 simply by using all atoms of the unit cell. The substitution of the scattering vector **S** by the reciprocal Miller indices *hkl* (expressed as vector **h**) of the reflecting planes, and positional vector **r** with the fractional coordinates **x** lead to the structure factor $\mathbf{F}_h$ of a reflection **h**:

$$\mathbf{F_h} = \sum_{j=1}^{atoms} f^0_{S,j} \cdot e^{2\pi i \mathbf{h x_j}} \tag{9}$$

The function for the electron density $\rho(\mathbf{x})$ can be obtained through a Fourier transformation (FT) of the structure factor function $\mathbf{F}_h$ given in Eq. 9:

$$\rho(\mathbf{x}) = \frac{1}{V} \sum_{\mathbf{h}=-\infty}^{+\infty} \mathbf{F_h} \cdot e^{-2\pi i \mathbf{h x}} \tag{10}$$

The diffraction patterns of protein crystals are typically detected by photon counting or charged-coupled devices, which result in intensity values for each reflection, however, no phase information. The intensity is proportional to the square of the structure factor amplitude (F_h). Thus, the missing phase information for each reflection (α_h) prevents the calculation of the electron density and has to be acquired by different approaches – this is also known as the crystallographic phase problem (directly apparent from Eq. 11).

$$\rho(\mathbf{x}) = \frac{1}{V} \sum_{\mathbf{h}=-\infty}^{+\infty} F_h \cdot e^{i\alpha_h} \cdot e^{-2\pi i \mathbf{h x}} \tag{11}$$

1.6.2 Phasing Methods

To solve the crystallographic phase problem, a variety of methods (or their combinations) exists. These methods can be divided into four groups (for details see Rupp (2010) or the following section “Molecular Replacement”):

- Substructure determination of specific marker atoms from difference data – the so-called *de novo* methods. They do not rely on prior knowledge of the protein structure and include methods like single or multiple isomorphous replacement (SIR/MIR), and single- or multiple-wavelength anomalous diffraction (SAD/MAD). SIR/MIR utilize the intensity differences of the diffraction pattern of native protein crystals and isomorphous, for example heavy metal atom, derivates of these crystals (Green *et al.*, 1954; Kendrew *et al.*, 1958). SAD/MAD utilize the anomalous scattering of (heavy) atoms generating differences in the

magnitude of the structure factors $\mathbf{F}_h$ and its symmetry related structure factor $\mathbf{F}_{-h}$ (Bijvoet pair) at specific wavelengths (depending on the type of atom and its environment) (Hendrickson, 1991; Matthews, 1966; Wang, 1985).

- Modification of the electron density. Density modifications, like solvent flattening, histogram matching, and density averaging, are mostly used to improve an initial electron density map obtained by other phasing methods. The solvent flattening methods, introduced by Wang (1985), improves the electron density map by masking (large) solvent areas in protein crystals discriminated from protein areas through differences in the average electron density of solvent (water) and protein. Histogram matching improves the electron density map by matching the electron density histogram of a low-quality map to that of a high-quality map (Lunin, 1988; Yong *et al.*, 1990). Density averaging uses non-crystallographic symmetry to average the electron density of multiple copies of the same molecule in the asymmetric unit.

- Direct methods – or *ab initio* structure determination – use phase relationships based on the observed intensities. These methods require data at atomic resolution (interatomic distance $>$ *d*-spacing, corresponding to resolutions of $\sim$1.2 Å or better for proteins (Sheldrick, 1990)), often only achievable for small and/or sturdy proteins and are generally used in small molecule structure determination. Direct methods in protein structure determination can be used to identify substructures of marker atoms. The interatomic distance between the generally used marker atoms (heavy atoms or anomalous scattering atoms) is unlikely below $\sim$3.5 Å. Thus, data sets up to this resolution are generally available and sufficient for substructure determination.

- Molecular replacement utilizes structurally similar proteins to calculate initial phases and is described in the following section “Molecular Replacement” in detail.

1.6.3 Molecular Replacement

In contrast to experimental phasing, molecular replacement is a method to obtain initial phases without the need of – not always trivial and often laborious – crystal derivatization or protein modification and anomalous data collection. The method exploits the fact that a certain amount of sequence similarity ($\sim$30 % and higher) is often a strong indicator for structural similarities between two proteins. Thus, a known protein structure can directly be used as starting model or as template for a homology model, which subsequently is rotated and translated in the unit cell or asymmetric unit (of a data set belonging to the protein with an unknown structure) until a best fit between observed and calculated structure factors is found.
The search for a best fit can be performed via six-dimensional search methods or rotation-translation methods. The simplest approach of a six-dimensional search – placing the model at n grid points with all possible orientations in the asymmetric unit and subsequent structure fac-

tor and correlation coefficient/R-factor calculation – results in a computationally intensive task. Over the past years, improved algorithms, such as evolutionary or stochastic search, in addition to rapidly increasing computer power have made this method applicable. Its major advantage compared to the computationally less intensive, rotation-translation search, is that the method will surely find the correct solution (given enough time and the existence of a solution). The rotation-translation search divides the search into two routines: The first step is a 3-dimensional rotation search followed by a 3-dimensional translation search. Both are rated by the correlation of the intra- (rotation) or intermolecular (translation) vectors of the respective Patterson maps calculated with the observed and the search model structure factors.
The calculation of the Patterson maps, required for a rotation-translation search, is based on the Patterson function, which is the autocorrelation of the electron density ρ of the unit cell (Patterson, 1934):

$$P(\mathbf{u}) = \int_R \rho(\mathbf{r})\,\rho(\mathbf{r}+\mathbf{u})\,d\mathbf{r} \tag{12}$$

$$= \rho(\mathbf{r}) * \rho(-\mathbf{r}) \tag{13}$$

$$= FT^{-1}\left(F_{\mathbf{h}}^2\right) \tag{14}$$

$$= \sum_{\mathbf{h}=-\infty}^{+\infty} F_{\mathbf{h}}^2 e^{-2\pi i \mathbf{h}\mathbf{u}} \tag{15}$$

Thus, the Patterson map can solely be calculated from the squares of the structure factor amplitudes and contains *N(N-1)* peaks for interatomic distance vectors for *N* atoms (without the self-vectors). Based on their magnitude, sets of intra- und intermolecular vectors can be defined. The intramolecular vectors are independent of the translation of the molecule and can therefore be used in a rotation search.
The downside of the rotation-translation search, especially compared to the six-dimensional search, is the fact that the solution of the rotation search with the highest correlation coefficient is not always the correct solution. In addition, even with a correct translation, minor errors in the rotation can lead to inconclusive solutions. In advantage over the six-dimensional search, the computational cost to find a correct solution by using the rotation-translation search is significantly reduced and various software solutions have implemented this method.
The absence of experimental phases in combination with phases generated with a most likely incomplete or inaccurate model molecule makes the obtained structure/electron density prone to the so-called model bias. Several methods exist to minimize this problem during subsequent model building and refinement.

1.6.4 Maximum Likelihood Map Coefficients

The bias of the electron density can be minimized by generating the maps with maximum likelihood (ML) map coefficients. The resulting σ_A-weighted maps account for model incompleteness

and model error. They were initially presented by Read (1986) based on the work of Main (1979) (with the variance of the structure factor probability distribution for the complete structure with N atoms Σ_N and for the partial model with P atoms Σ_P, the figure-of-merit $m = \langle \cos \Delta\varphi \rangle$, the Luzzanti factor D, and the weighted phase φ_{wt}):

$$\sigma_A = D(\Sigma_P / \Sigma_N)^{1/2} \tag{16}$$

$$\rho_{ML}(\mathbf{x}) = \sum_{\mathbf{h}=-\infty}^{+\infty} \mathbf{F_{ML}} \cdot e^{-2\pi i \mathbf{hx}} \tag{17}$$

$$\mathbf{F_{ML}} = (2mF_{obs} - DF_{calc}) \cdot e^{\varphi_{wt}} \text{ (acentric reflections)} \tag{18}$$

$$\mathbf{F_{ML}} = mF_{obs} \cdot e^{\varphi_{wt}} \text{ (centric reflections)} \tag{19}$$

The resulting map is generally used for subsequent model building and refinement, often augmented by the usage of difference maps:

$$\mathbf{F_{ML}} = (mF_{obs} - DF_{calc}) \cdot e^{\varphi_{wt}} \tag{20}$$

1.6.5 Omit Maps

The omit maps account for the model bias by a “memory effect” of the model: Incorrectly placed atoms affect correctly placed atoms in their vicinity during refinement through geometric restraints. Thus, simply removing the incorrectly placed atoms does not completely remove the incorrect information from the model. Omit maps are in general calculated by omitting larger parts of the model, followed by phase calculation and remodeling of the omitted area. Various variations and enhancements of this concept exists, like simulated annealing (SA) (Hodel *et al.*, 1992) or composite iterative-build omit maps (Terwilliger *et al.*, 2008). The SA omit maps are obtained by a combination of omitting a questionable part of the model or a ligand, restraining the atoms of the surrounding space to avoid migration into the omitted region, and a SA refinement. The advantage of this method is its ability to overcome the mathematical problem of "local-minima-solution" situations by including the SA step, which makes it more effective in removing the model bias than the "simple" omit map. The SA algorithm imitates the slow cooling process of melted metal by a slow decrease of the probability of a variable to obtain worse solutions during a solution search. Thus, SA can overcome barriers between local minima and can be more efficient than a brute-force search.
A recent and computationally intensive approach is the (composite) iterative-build omit map (Terwilliger *et al.*, 2008). An iterative-build omit map is calculated by setting the occupancy of the atoms of an omitted region (incl. a border) to zero while performing an iterative model-building, refinement, and density-modification procedure. Thereby, the atoms in the omitted regions do not contribute to the structure factor calculation, but take part in geometry calcu-

lations. A composite iterative-build omit map is generated by calculating several iterative-build omit maps covering the complete asymmetric unit in total and the subsequent composition of the map by combining all maps of the omitted regions.

1.6.6 Data Quality and Model Validation

The refinement progress of the model and the model-to-data fit can be "monitored" and validated by several coefficients to check for over- or under-fitting of the measured data.
The frequently used R-factor is defined as:

$$R = \frac{\sum_{\mathrm{hkl}} |\mathrm{F_{obs}}\,(\mathrm{hkl}) - \mathrm{F_{calc}}\,(\mathrm{hkl})|}{\sum_{\mathrm{hkl}} \mathrm{F_{obs}}\,(\mathrm{hkl})} \tag{21}$$

It is generally calculated from two sets of the reflections for cross-validation (Brünger, 1992): 5-10 % of the reflections are used to calculate R_{free} and are not used for F_{calc} calculation during refinement. The remaining reflections are used to calculate R_{work} and are used during refinement. A decrease of R_{work} without corresponding decrease of R_{free} indicates overfitting.
The real space correlation coefficient (RSCC) is derived from the observed and the calculated electron density map [using observed and calculated structure factors, respectively (Brändén and Jones, 1990; Jones *et al.*, 1991)]. In advantage over the R-factor, it allows for quick identification of problematic regions of a model (in conjunction with B-factors and occupancies).
Inspection of the model stereochemistry and comparison to known restrictions or most likely states is often used, especially for low-resolution structures, to measure the validity of a model. Examples are the Ramachandran plot statsistic [φ and ψ angle distribution of the C_α backbone (Ramachandran *et al.*, 1963)], steric clashes, χ-angle rotamer outliers of the side chains, and deviation from ideal bond length, angle or planarity.
The quality of the model depends on the quality of the data used to build it. The quality of the crystallographic data can be measured with different R-factors: $\mathrm{R}_{merge/sym}$, R_{meas} [multiplicity corrected R_{merge} (Diederichs and Karplus, 1997)], and R_{pim} [precision-indicating R_{merge} (Weiss, 2001)], all calculated from the intensities (I).

$$R_{merge} = \frac{\sum_{\mathbf{h}} \sum_{i=1}^{n} |I_i\,(\mathbf{h}) - \langle I\,(\mathbf{h})\rangle|}{\sum_{\mathbf{h}} \sum_{i=1}^{n} I_i\,(\mathbf{h})} \tag{22}$$

These R-factors (values above ∼0.6-0.8), together with the signal-to-noise ratio $\left\langle \frac{\langle I\rangle}{\sigma(\langle I\rangle)} \right\rangle$ (values below ∼2.0), are often used to define a (high) resolution cut-off with the intention to exclude weak data supposedly decreasing model quality (Evans, 2011; Karplus and Diederichs, 2012). These criteria are a matter of debate. The R-factors (in contrast to R_{work}/R_{free}) above mentioned converge independently from data quality towards infinity for high resolution. This originates from the decrease of the atomic scattering factor at increasing scattering angles (see Eq. 7) resulting in a principle decrease of signal intensity at higher resolution. As a consequence, the

denominator converges towards zero and the numerator converges towards a constant value (see Eq. 22). Thus, Karplus and Diederichs (2012) introduced new coefficients to measure data quality and over- or underfitting of the model based on the Pearson correlation coefficient (CC): $CC_{1/2}$, CC^*, CC_{work}, and CC_{free}. The $CC_{1/2}$ is the CC calculated between the average intensities of each of the halves of the data set, each containing randomly assigned unique reflections. The CC^* is an estimation of the true CC between the noise-free true signal and the averaged (complete) data set:

$$CC^* = \sqrt{\frac{2CC_{1/2}}{1 + CC_{1/2}}} \tag{23}$$

CC_{work} and CC_{free} are the standard and cross-validated CCs between the observed and model intensities (in analogy to R_{free}/R_{work}). The model quality can be validated by comparing CC^* with CC_{work} and CC_{free}:

- $CC_{work} > CC^*$ indicates overfitting
- $CC_{free} > CC^*$ indicates underfitting
- $CC_{free} \approx CC^*$ data quality limits model improvement

2 Material and Methods

2.1 Materials

DNA oligonucleotides/primers were obtained from Eurofins Genomics (Ebersberg, Germany); DNA-purification reagents and kits were obtained from Qiagen (Hilden, Germany) or Macherey-Nagel (Düren, Germany); if not stated otherwise, all other reagents were obtained from Sigma-Aldrich (St. Louis, Missouri, USA) or Carl Roth (Karlsruhe, Germany).

2.2 Generation of Expression Plasmids for *Bv*HSS and *Bv*HSS Variants

The *Bv*HSS cDNA was amplified by touchdown polymerase chain reaction (PCR, for primers see Table 2.1) by using a previously generated plasmid containing *Bv*HSS cDNA (Tholl *et al.*, 1996) as template and *pfu* DNA polymerase (Promega, Fitchburg, Wisconsin, USA) to introduce NcoI and XhoI restriction sites at the 5' and 3' ends, respectively. The PCR product was digested with NcoI and XhoI endonucleases (Promega, Fitchburg, Wisconsin, USA). The *Bv*HSS cDNA was ligated into the NcoI/XhoI opened expression vector pETM14 (EMBL, providing an N-terminal 6xHis-tag followed by a human rhinovirus 3C (HRV3C) protease cleavage site). Ligation was performed with T4 DNA ligase (Invitrogen, now Life Technologies, Thermo Fisher Scientific, Waltham, Massachusetts, USA). The resulting plasmid pETM14-*Bv*HSS was transformed into the *E. coli* TOP10 strain for subsequent screening and control sequencing. Variants

Table 2.1: Primers used in the PCRs to generate expression plasmids for *Bv*HSS and *Bv*HSS variants.

Description	Sequence
*Bv*HSS subcloning into pETM14 forward (red: NcoI site)	5'-ATA TAC CAT GGG AAC CGA TTG GCC GGT TTA TCA CCG CAT-3'
*Bv*HSS subcloning into pETM14 reverse (red: XhoI site)	5'-ATA TAC TCG AGT CAG TCC CGC ACC AGC ACG TTG CGG AA-3'
*Bv*HSS variant N162D forward	5'-GTG CTG CGG CGC CGA TCC CGG CAT GGT G-3'
*Bv*HSS variant N162D reverse	5'-CAC CAT GCC GGG ATC GGC GCC GCA GCA C-3'
*Bv*HSS variant E237Q forward	5'-GGT TTC GTG TCG CAG GGC CTG CAG C-3'
*Bv*HSS variant E237Q reverse	5'-GCT GCA GGC CCT GCG ACA CGA AAC C-3'
*Bv*HSS variant H296S forward	5'-TAC GGC TTC CTG GTC ACC TCC AAC GAA TCG ATC TCG AT-3'
*Bv*HSS variant H296S reverse	5'-ATC GAG ATC GAT TCG TTG GAG GTG ACC AGG AAG CCG TA-3'
*Bv*HSS variant E298Q forward	5'-GGT CAC CCA CAA CCA ATC GAT CTC GAT C-3'
*Bv*HSS variant E298Q reverse	5'-GAT CGA GAT CGA TTG GTT GTG GGT GAC C-3'

of *Bv*HSS were generated via side-directed mutagenesis according to the Quikchange protocol from Stratagene by using phusion high-fidelity DNA polymerase (Fermentas, now part of Thermo Fisher Scientific, Waltham, Massachusetts, USA) or *pfu* DNA polymerase (Promega, Fitchburg, Wisconsin, USA) with pETM14-*Bv*HSS plasmid as template and the primers given in Table 2.1. Template plasmid was digested with restriction endonuclease DpnI prior to transformation of the reaction mixture into *E. coli* XL1 or TOP10 strains for subsequent screening and control sequencing. For *Bv*HSS expression, plasmids were transformed into the *E. coli* BL21 (DE3) expression strain.
The transfer of the *Bv*HSS cDNA into the pETM14 vector and the generation of the *Bv*HSS variant H296S have been performed by the group of Prof. Dr. Dietrich Ober at the Botanical Institute – Biochemical Ecology and Molecular Evolution, Kiel University.

2.3 Expression and Purification of *Bv*HSS

The BL21 (DE3) cells were cultivated in 1 L LB-Media (including 30 µg/ml kanamycine) in 5 L baffled Erlenmeyer flasks (at 37℃ in a standard laboratory shaking incubator) inoculated with an overnight culture to give a starting absorbance at 600 nm (OD_{600}) of approximately 0.05. Alternatively, cells were cultivated in 5 L LB-Media (incl. 30 µg/ml kanamycine) in a 10 L bioreactor (Biostat Bplus, Sartorius AG) at 37℃ with monitored and controlled oxygen concentration. Induction occurred at an OD_{600} of approximately 0.6 with 1 mM isopropyl β-D-1-thiogalactopyranoside (IPTG) followed by a 4 h incubation at 25℃. Cells were harvested by centrifugation (10 min, 7000 g, 4℃) and either stored at -80℃ or kept on ice for immediate processing. Raw *E. coli* extract was prepared by disintegrating resuspended cells (1:10 (w:v) ratio in 50 mM BIS-TRIS propane pH 9, 25 mM KCl, 25 mM imidazole, 10 mM dithiothreitol (DTT), 1 mM phenylmethanesulfonyl fluoride (PMSF)) in an Avestin Emulsiflex C3 (1 passage using pulses of approximately 1200 bar) and two subsequent centrifugation steps (30 min, 75600

g, 4℃). The *Bv*HSS was purified from the raw extract via immobilized metal ion affinity chromatography (IMAC) with the N-terminal 6xHis-tag by using a HisTrap HP 5 ml column and an ÄKTA Purifier FPLC system (both GE Healthcare, Little Chalfont, United Kingdom). Protein was bound to the equilibrated Ni(II)-nitrilotri-acetic acid (NTA) matrix (10 column volumes (CV) of 50 mM BIS-TRIS propane pH 9, 25 mM KCl, 10 mM DTT (standard buffer)) followed by a washing step of 10 CV (25 mM imidazole in standard buffer) and a linear elution gradient over 5 CV to a final concentration of 500 mM imidazole in standard buffer. The *Bv*HSS eluted as a single, sharp, and symmetric peak at approximately 200 mM imidazole. In order to separate the 6xHis-tag from *Bv*HSS, the *Bv*HSS was incubated at 4℃ overnight with GST-tagged HRV3C protease (1:100 (w:w) ratio) in fresh standard buffer. The buffer was exchanged according to the manufacturer's recommended standard procedure with HiTrap Desalting columns (GE Healthcare, Little Chalfont, United Kingdom). The HRV3C protease and the 6xHis-tag were removed by coupled GSTrap and HisTrap columns. Purity of the *Bv*HSS was verified by analytical size-exclusion chromatography (Superdex 75, 10/30HR, GE Healthcare, Little Chalfont, United Kingdom) and photon correlation spectroscopy/dynamic light scattering (Zetasizer Nano-S, Malvern Instruments, Malvern, Worcestershire, United Kingdom). *Bv*HSS was stored in aliquots at a concentration between 5-6 mg/ml in standard buffer supplemented with 2 mM NAD^+ at -80℃.
Sodium dodecyle sulfate polyacrylamid gel electrophoresis (SDS-PAGE) for process and purity control was performed according to Laemmli (1970) using the Mini-PROTEAN system (Bio-Rad). Stacking gel (5 % acrylamide) and separation gel (15 % acrylamide) were prepared from Rotiphorese gel 30 acrylamide solution (Carl Roth, Karlsruhe, Germany, 30 % acrylamide:bis-acrylamide 37,5:1). Samples were mixed in a 4:1 ratio with 4x reducing SDS-PAGE loading buffer (250 mM TRIS-HCl pH 6.8, 20 % (w/v) glycerol, 8 % (w/v) SDS, 0.2 % (w/v) bromphenole blue, 20 % (v/v) β-mercaptoethanol), heated to 95℃ for 5 min and subsequently cooled on ice prior loading onto gels. The low molecular weight marker (GE Healthcare, Little Chalfont, United Kingdom) was used as protein standard. The electrophoresis was performed at a constant voltage of 250 V for 45-60 min. After separation gels were fixed and stained in a Coomassie Brilliant Blue R-250 staining solution (20 % (v/v) ethanol, 10 % (v/v) acetic acid, 0.1 % (w/v) Coomassie Brilliant Blue R-250) until a sufficient staining was reached. Destaining was done in destaining solution (20 % ethanol, 10 % acetic acid) until a sufficient destaining was acquired.

2.4 HSS Activity Assay

*Bv*HSS activity was tested according to a modified protocol published in Ober *et al.* (1996). Briefly, enzyme assays were performed in a total volume of 25 µl in 100 mM glycine NaOH buffer pH 9.0 containing 1 mM [1,4-^{14}C]-putrescine (0.025 µCi/assay) and 2 mM NAD^+. Assays were incubated for 2 to 8 min at 37℃. Formation of HSP was followed quantitatively by thin layer chromatography equipped with a radio-scanner (RITA, Raytest, Straubenhardt, Germany). These assays were exclusively carried out by the group of Prof. Dr. Dietrich Ober at the Botanical Institute – Biochemical Ecology and Molecular Evolution, Kiel University.

2.5 Qualitative HSS Activity Assay for HPLC-based Polyamine Analysis

The enzyme (0.5 mg/ml) was incubated at 37 °C for 1 h with 2 mM PUT in standard buffer supplemented with 2 mM NAD^+ in a total volume of 100 µl. The reaction was stopped by precipitation with trichloroacetic acid and analyzed by high-pressure liquid chromatography (HPLC; sample preparation according to the preparation of samples from *Bv*HSS crystals as described under section "Sample Preparation for HPLC Analysis").

2.6 Sample Preparation for HPLC Analysis

For polyamine content analysis of *Bv*HSS crystals, the soaking of crystals obtained from the co-crystallization of *Bv*HSS with DAP was performed with PUT for 300 s as described under crystallization and data collection. Samples from *Bv*HSS crystals were prepared by transferring single or multiple crystals with minimal amounts of mother liquor from the drop of the crystallization or soaking solution into a 0.5 µl drop of 0.2 M borate buffer pH 8.5 followed by immediate protein precipitation via addition of 0.5 µl 0.6 M trichloroacetic acid. Precipitated protein was removed by centrifugation for 1 min at 16000 g. The supernatant was transferred to a new tube and brought to approximately pH 8.5 with a final volume of 10 µl by addition of 9 µl 0.2 M borate buffer pH 8.5.
Each sample was derivatized for 5 min in the dark at room temperature by addition of a 10 mM 6-aminoquinolyl-N-hydroxysuccinimidyl carbamate (Synchem UG & Co. KG, Altenburg, Germany) solution in anhydrous acetonitrile at a 1:2.5 (v:v) ratio followed by immediate analysis.

2.7 HPLC-based Polyamine Analysis

Polyamine composition was analyzed according to Weiss *et al.* (1997). Separations were performed on a C18 column (250 x 4.6 mm, ProntoSIL Hypersorb ODS, F180PY050, Bischoff Analysetechnik und -geräte GmbH, Leonberg, Germany) by using an Agilent 1100 Series HPLC system (Degasser G1379A, Quat Pump G1311A, Man. Inj. G1328B, COLCOM G1316A, DAD G1315B, FLD G1321A, RID G1362A, Agilent Technologies, Santa Clara, California, USA) controlled by ChemStation software version B.01.03 (Agilent Technologies, Santa Clara, California, USA).
The mobile phase consisted of a gradient (details see Weiss *et al.* (1997)) of solvent A (25 mM triethylamine, titrated to pH 4.8 with acetic acid), solvent B (acetonitrile:water 80:20 (v/v)), and solvent C (methanol). Samples of 10 µl were injected into the column and analyzed at a flow rate of 1.3 ml/min at 33 °C with online UV detection at 210 nm and online fluorescence detection at λ_{Ex} = 248 nm, λ_{Em} = 398 nm.
Retention times were verified by analysis of calibration mixtures containing approximately 0.8, 8, or 80 pmol DAP, PUT, SPD, and HSP at appropriate time points during the analysis. The general applicability of sample preparation and polyamine content analysis of samples contain-

ing *Bv*HSS was verified by performing qualitative HSS activity assays followed by HPLC-based analyses.

2.8 Crystallization and Data Collection

*Bv*HSS without additional polyamines could be crystallized at 18 °C by the hanging-drop vapor-diffusion method by using drops consisting of 1 µl protein solution (4 mg/ml in standard buffer) and 1 µl reservoir solution equilibrated against 500 µl reservoir solution (100 mM sodium acetate pH 4.6, 100 mM ammonium acetate, 34 % (w/v) PEG 3350). *Bv*HSS and *Bv*HSS variants with polyamines could be crystallized at 18 °C by the hanging-drop vapor-diffusion method by using drops consisting of 1 µl protein solution (4 mg/ml in 33 mM BIS-TRIS propane pH 9, 17 mM KCl, 6.7 mM DTT, 1.3 mM NAD) including 0.2 M of each polyamine (1:2650 molecular ratio to guarantee substrate saturation, see Table 3.1 for details) and 1 µl reservoir solution equilibrated against 500 µl reservoir solution (100 mM sodium acetate pH 4.6 – 4.8, 150 mM ammonium acetate, 22-26 % (w/v) PEG 10000, 150 – 300 mM 3-pyridin-1-ium-1-ylpropane-1-sulfonate [NDSB-201]). Crystals appeared after 3-5 days. In contrast to *Bv*HSS without polyamines growing as single crystals, the *Bv*HSS and *Bv*HSS variants with polyamines exclusively led to rod-shaped crystal clusters. Clustered crystals were carefully manually disintegrated to obtain single rod-shaped crystals. In the case of *Bv*HSS without additional polyamines, the crystals were cryoprotected by short equilibration in 60 % (v/v) reservoir solution in double-distilled H_2O (ddH_2O) supplemented with 10 % (v/v) PEG 400 prior to flash-cooling in liquid N_2. The soaking of *Bv*HSS crystals with polyamines was performed by transferring crystals into a 0.2 M polyamine solution in a 2:3 dilution of the respective reservoir solution with ddH_2O (67 mM sodium acetate pH 4.6 – 4.8, 100 mM ammonium acetate, 14.7-17.3 % (v/v) PEG 10000, 100 - 200 mM NDSB-201) followed by an incubation for 5 min at 18 °C prior to cooling. *Bv*HSS and *Bv*HSS variants with polyamines were flash-cooled in liquid N_2 without any cryoprotectant.
The initial crystallization screenings have been performed by using the HTX crystallization facility at the EMBL Hamburg, Germany.
Diffraction data were collected at beam line 14.2 (Joint Berlin MX Lab, BESSY II, Berlin-Adlershof, Germany) by using a RAYONIX MX-225 CCD detector (structure with PDB ID 4PLP), beam lines P13 and P14 (EMBL, DESY PETRA III, Hamburg, Germany) by using a Pilatus 6M-F detector (structures with PDB ID 4TVB, PDB ID 4XR4, PDB ID 4XQC, PDB ID 4XQE, PDB ID 4XRG, and PDB ID 4XQG) and beam line ID23 (ESRF, Grenoble, France) by using a ADSC Quantum Q315R detector (structure with PDB ID 4XQ9). X-ray diffraction was performed at a temperature of 100 K.

2.9 Structure Determination, Interpretation and Representation

Diffraction data were indexed and integrated by using the software XDS (Kabsch, 2010). The space group was determined with the program Pointless of the CCP4 program suite (Evans,

2011; Potterton *et al.*, 2003). Data were scaled and merged together by applying the FreeR-flag to 5 % of reflections by using the software SCALA within the CCP4 program suite (Evans, 2011; Potterton *et al.*, 2003). The structure of *Bv*HSS without polyamines (PDB ID 4PLP) was solved via molecular replacement (MR; resolution range of used data: 47.59 – 3.0 Å; resulting correlation coefficient: 0.312 [correct solution], 0.186 [second unrelated peak]; resulting R-factor: 0.527 [correct solution], 0.570 [second unrelated peak]) by using the software MOLREP within the CCP4 program suite (Murshudov *et al.*, 1997; Potterton *et al.*, 2003; Vagin and Teplyakov, 1997). The starting model for MR was built by the PHYRE server by using the HSS structure from *L. pneumophila* (PDB ID 2PH5 (Forouhar), subunit A, 44 % sequence identity) (Kelley and Sternberg, 2009). MR was followed by *Bv*HSS automated model building with the software ARP/wARP (Mooij et al., 2009). The *Bv*HSS model was iteratively completed by alternating refinement steps with the software PHENIX.refine (Afonine *et al.*, 2012) and manual inspection and modification by using the program Coot (Emsley *et al.*, 2010). The refined model (PDB ID 4PLP) was used as starting model for structure determination from all other data sets collected from crystals of *Bv*HSS and *Bv*HSS variants by using the same procedure as described above.

The pH-dependent electrostatic potential maps were calculated by using the software APBS Version 1.3 (Baker *et al.*, 2001) with the AMBER99 force field (Wang *et al.*, 2000). Input files in PQR-format for APBS were generated from files containing *Bv*HSS atom coordinates in PDB-format with a modified version of the program PDB2PQR version 1.9.0 (to consider ligands in the pK_a prediction, PROPKA version 3.0 was replaced with version 3.1) in order to calculate pK_a values and set protonation states for titratable groups accordingly (Dolinsky *et al.*, 2007; Søndergaard *et al.*, 2011). The volume and surface of the binding pocket was calculated with the software HOLLOW (Ho and Gruswitz, 2008) by filling the interior of the protein with dummy atoms (1.4 Å radius) on a grid (spacing 0.2 Å) and manually including water molecules based on the structure from *Bv*HSS (PDB ID 4PLP).

All visualization and preparation of 3D structural images was performed with PyMOL (Schrodinger, 2010).

3 Results and Discussion

3.1 Protein Production and Purification

The results of the protein production and purification will be presented exemplary for the *Bv*HSS variant H296S. All other *Bv*HSS variants were produced and purified by using the same protocol and led to comparable results.

Figure 3.1 outlines the general procedure of the *Bv*HSS production and purification strategy. For details see subsection “Expression and Purification of *Bv*HSS” under Material and Methods on page 15. Briefly, after cultivation and harvesting the *E. coli* were disintegrated by sheer force

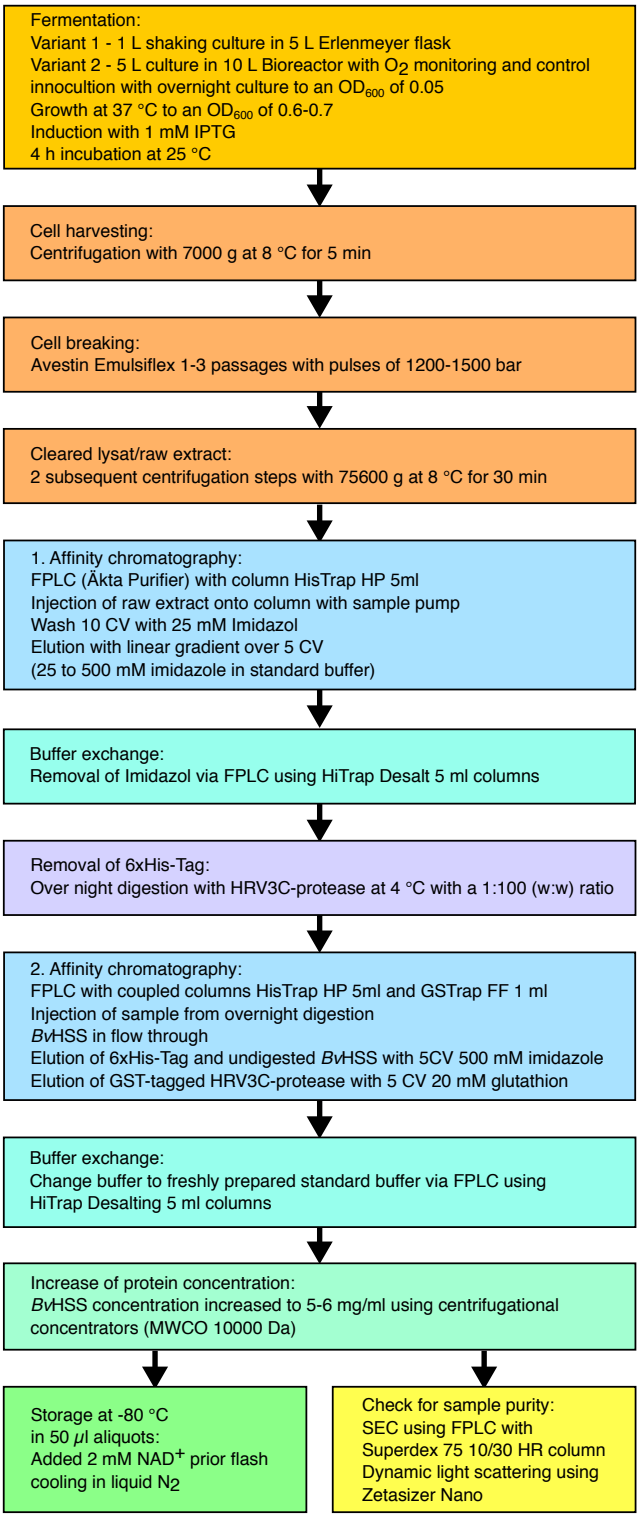

Figure 3.1: Outline of the complete *Bv*HSS expression and purification process.

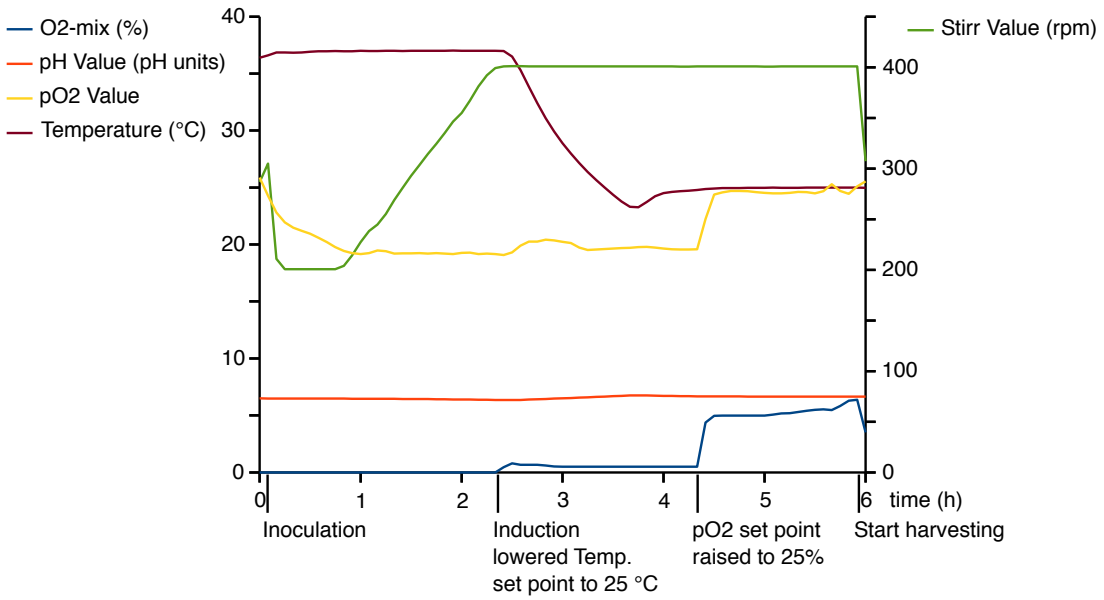

Figure 3.2: Process parameters of a representative fermentation of *E. coli* BL21(DE3) to produce recombinant *Bv*HSS. Relevant time points (inoculation, induction, and pO2 set point adjustment from 20 % to 25 %) are indicated by arrows. All parameters were recorded by the Software MFSC/DA 1 version 2.1 of the Biostat Bplus bioreactor during *Bv*HSS variant H296S production.

using the Emulsiflex C3 (Avestine). The lysat was cleared through centrifugation and the raw extract was applied onto a Ni(II)-NTA-matrix using an FPLC system (Äkta Purifier, GE Healthcare, Little Chalfont, United Kingdom). After a washing step the bound protein was eluted with a linear imidazol gradient over five column volumes (CV). The 6xHis-tag was removed via overnight digestion with GST-tagged HRV3C-protease followed by protease and 6xHis-tag removal and purity analysis.

The *E. coli* producing *Bv*HSS variant H296S was cultured in 5 L LB in a bioreactor (Biostat Bplus, Sartorius AG). During the process the pH, temperature, and solved oxygen level were monitored. In addition, temperature and oxygen level were controlled. As indicated in Figure 3.2, the protein production was induced after an approx. 2.5 h long growth phase. The temperature set point of 25 °C was reached approximately 1 h after induction and was maintained until the end of the process. During the whole process, the pH was stable at approx. pH 7. The oxygen concentration in the media never dropped below the set point (20 % and 25 % from 4.3 h as indicated in figure 3.2). The cell harvest, approximately 3.5 h post induction, resulted in an 18 g (wet weight) cell pellet. The cells were subsequently lysed to an approximately 200 ml large raw extract.

The results from the first purification step are shown in Figure 3.3. The cleared raw extract (approximately 180 ml) was loaded onto the column by using a P960 sample pump (GE Healthcare, Little Chalfont, United Kingdom). During the washing step, the absorption at 280 nm nearly reached the baseline (Fig. 3.3 a). One sharp peak started to elute at an imidazole concentration

of approximately 200 mM with a total volume of about 7 ml (Fig 3.3 b, indicated by yellow bar). Analysis of the applied sample and the collected fractions by SDS-PAGE is shown in Figure 3.4. The cleared raw extract showed a strong band at approximately 50 kDa, which was no longer present in the column flow through, representing with almost absolute certainty the *Bv*HSS (theoretical molecular weight 52.9 kDa). The SDS-PAGE showed one band at 50 kDa in the fraction A5 of the washing step and the fractions A11, A12 and B7. Besides the very strong peak of 50 kDa in the fractions B11 and B9 of the elution peak (and in the pool of the fractions A12-B7 and in subsequently obtained samples from post imidazol removal and overnight digestion), were a multitude of weak bands of sizes only below 50 kDa detectable. In conjunction, this indicates a successful first purification step resulting in already very pure *Bv*HSS with a total amount of approx. 33 mg protein (as determined via absorption at 280 nm) after removal of imidazol.

The results of the removal of the released 6xHis-tag and the GST-tagged HRV3C-protease are shown in Figure 3.5. The flow through fractions A7, B6, B4, B2, C8, and C10 only showed weak bands at 50 kDa in the SDS-PAGE (Fig. 3.5 b). In contrast, the flow through fraction A9, A11, B12, B10, and B8 showed a strong band at 50 kDa and weak bands at sizes below 50 kDa. The fraction E3 of the only strong and clear elution peak (indicated by a green bar, Fig. 3.5 a) detectable by absorption at 280 nm, showed two equally strong bands at around 50 kDa and some bands below 50 kDa at approx. 45, 40, 28, 27 kDa. Fractions A9 to B8 were pooled and used for subsequent processing. Indicated by the huge amounts of protein in the flow through, the 6xHis-tag was successfully removed from the major part of the *Bv*HSS. The two observed bands at around 50 kDa in the elution fraction E3 are most likely *Bv*HSS with and without 6xHis-tag. The *Bv*HSS is present as homodimer in solution under given conditions [see results from dynamic light scattering (DLS) analysis shown in Fig. 3.7 and Tholl *et al.* (1996)]. Thus, one *Bv*HSS without 6xHis-tag might have been bound to another *Bv*HSS with 6xHis-tag that was bound to the Ni(II)-NTA-column. The observed bands at sizes below 50 kDa in the elution fraction E3 suggest that also some of the protein impurities were removed during this step of the purification process. Because of these impurities and the relative low protein content compared to the fractions A9 to B8, the fraction E3 was discarded. Not being within the scope of interest and because of no identifiable peaks during the elution of the GST-tagged HRV3C-protease and thus no further analysis of respective fractions, the recovery of the protease remained unanswered.

With the *Bv*HSS already being present in a highly pure solution, the necessity for further purification steps was assessed based on analytical size exclusion chromatography (SEC) and DLS analysis. The results are shown in Figure 3.6 and 3.7.

The SEC was performed with two samples to ascertain a potential beneficial influence of NAD^+ addition on the aggregation or multimerization as indicator for the stability under given conditions of *Bv*HSS: one analysis was done with *Bv*HSS without additional NAD^+ (Fig. 3.6 a) the other was done with *Bv*HSS with 2 mM NAD^+ added prior to injection (Fig. 3.6 b). In both cases a strong and sharp symmetric peak (peak 1) with a potential small leading “shoulder” at approx.

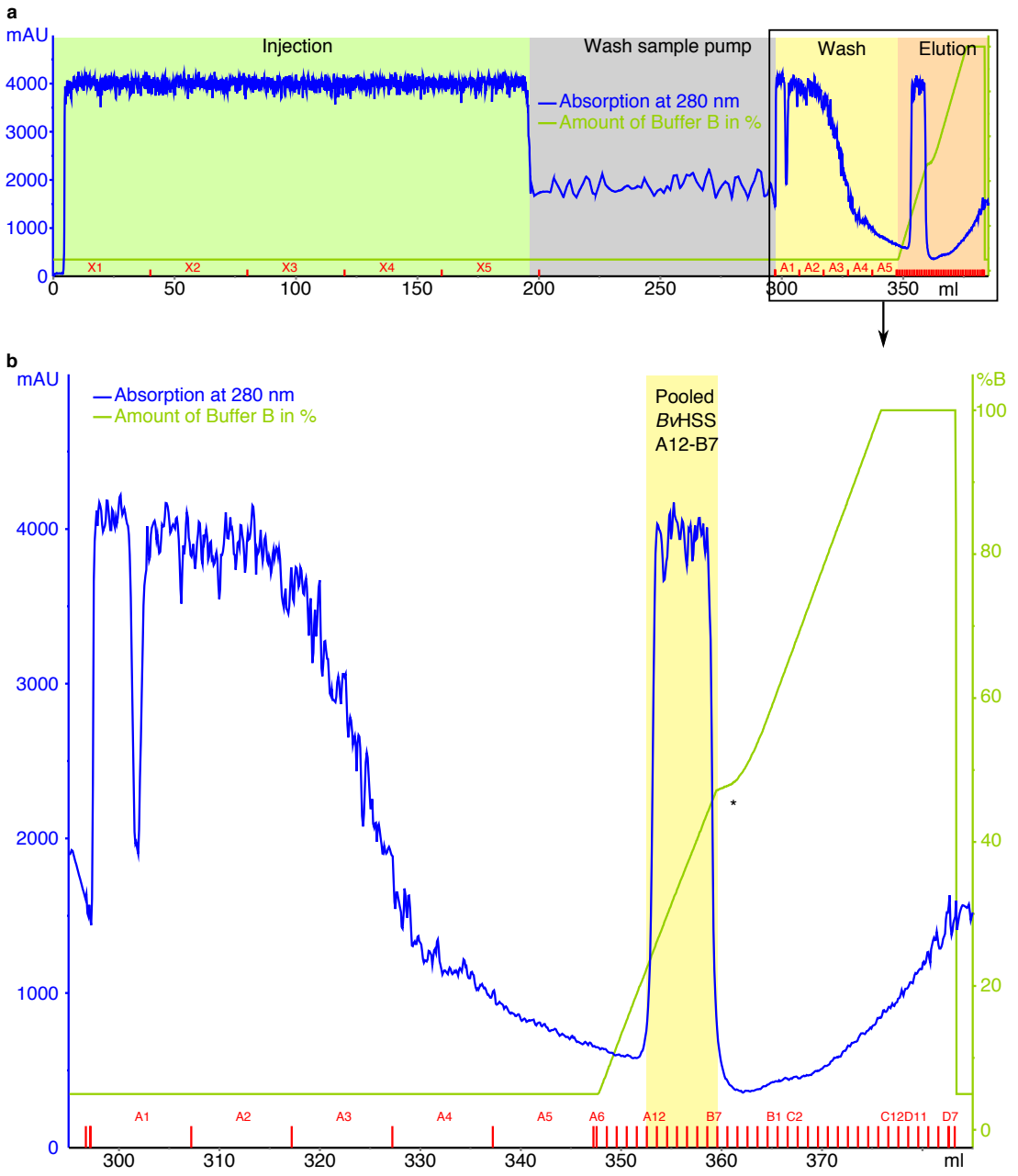

Figure 3.3: Chromatogram of the first purification step of *Bv*HSS variant H296S. The complete chromatogram, including sample injection, is shown in (a) and the steps of the chromatography are indicated by color bars (green = injection, yellow = column wash, orange = elution, grey = sample pump wash after injection bypassing the column). A magnification of the chromatogram of the washing and elution steps is additionally shown in (b) with the (subsequently pooled) elution peak of the *Bv*HSS (as determined by SDS-PAGE) indicated by a yellow bar. The collected fractions are indicated by the red horizontal lines (above the x-axis). The irregularity of the linear elution gradient (indicated by an asterisk [*]) was caused by a software error during the purification procedure and did not affect the protein purification. The fluctuations of the absorbance at 280 nm are caused by the high protein amounts in the sample leading to signals beyond the upper detection limit of the UV detector.

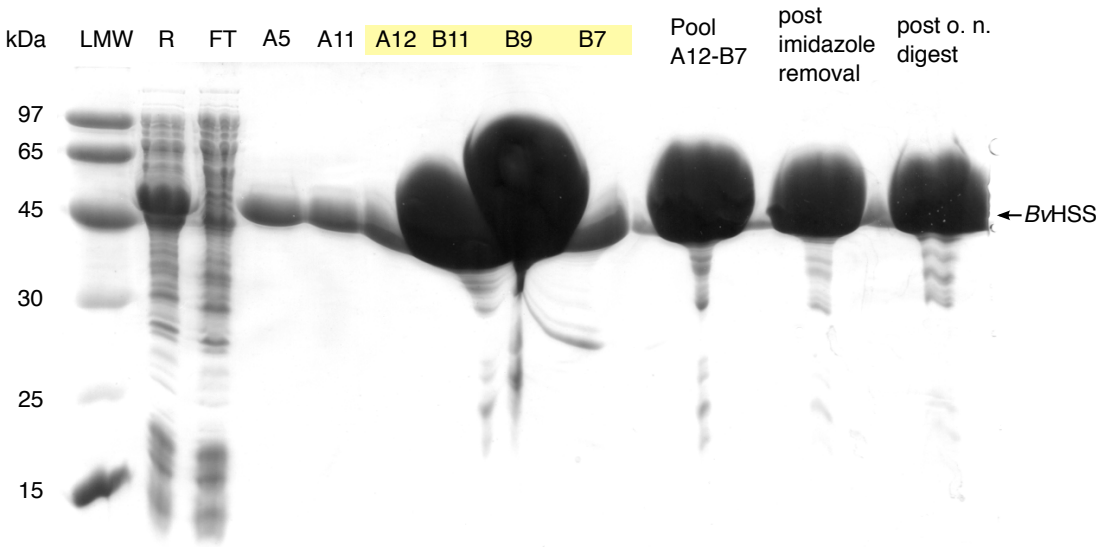

Figure 3.4: Analysis of the fractions of the first purification steps of the *Bv*HSS H296S by SDS-PAGE. The SDS-PAGE (15%, reducing conditions, expected *Bv*HSS height indicated by arrow) was loaded with a protein ladder (LMW), the raw extract (R) obtained after cell disintegration and centrifugation, the flow through of the first affinity chromatography (FT = fractions X1-X5, Fig. 3.3 a), the fractions A5, A11, A12, B11, B9, and B7 of the first affinity chromatography, the pooled (fractions A12-B7) protein prior and after imidazole removal, and after the overnight digestion with HRV3C protease. The wash/elution fractions and the pooled protein samples were loaded with matching volumes to allow for the estimation of the relative protein content.

9.5 ml post injection (Fig. 3.6 a, indicated by yellow bar and Fig. 3.6 b, indicated by green bar) and a small symmetric peak (peak 3) at approx. 27.5 ml post injection were detected by absorption spectroscopy at 280 nm. In addition, during analysis of *Bv*HSS with added NAD^+, a sharp symmetric peak (peak 2) with a potential small leading “shoulder” at approx 16.5 ml (Fig. 3.6 b, indicated by orange bar) was detected by absorption spectroscopy at 280 nm. The corresponding collected fractions of the peaks at 9.5 ml and 16.5 ml were analyzed by SDS-PAGE (Fig. 3.6 c, highlighted with the respective colors of the peaks in Fig. 3.6 a and b). In all fractions, with exception of the fraction H1 (belonging to the peak 2), a band at approx. 50 kDa representing *Bv*HSS, was detected. In addition, in the fractions corresponding to peak 1 maxima at least 4 bands at sizes below 50 kDa were visible. Comparable bands at the same corresponding sizes were detected in the injected sample (Fig. 3.6 c, labeled Inj. S.). In the fraction H1 from peak 2 were no bands between 100 and 25 kDa detected.
The addition of NAD^+ did not affect the multimerziation or aggregation of *Bv*HSS. The retention time of peak 1 of both SECs approximately corresponds to a molecular weight of 100 kDa (based on the reference chromatograms provided by GE Healthcare, Little Chalfont, United Kingdom), reflecting the expected *Bv*HSS dimer. The SEC did not result in an increased purity of *Bv*HSS. The SDS-PAGE analysis of the fractions from peak 1 start and end (fractions D9 compared to D4 and G6 compared to G11) did not show any differences in sample composition. The observed leading shoulders of peak 1 and also peak 2 might therefore be unrelated to sample

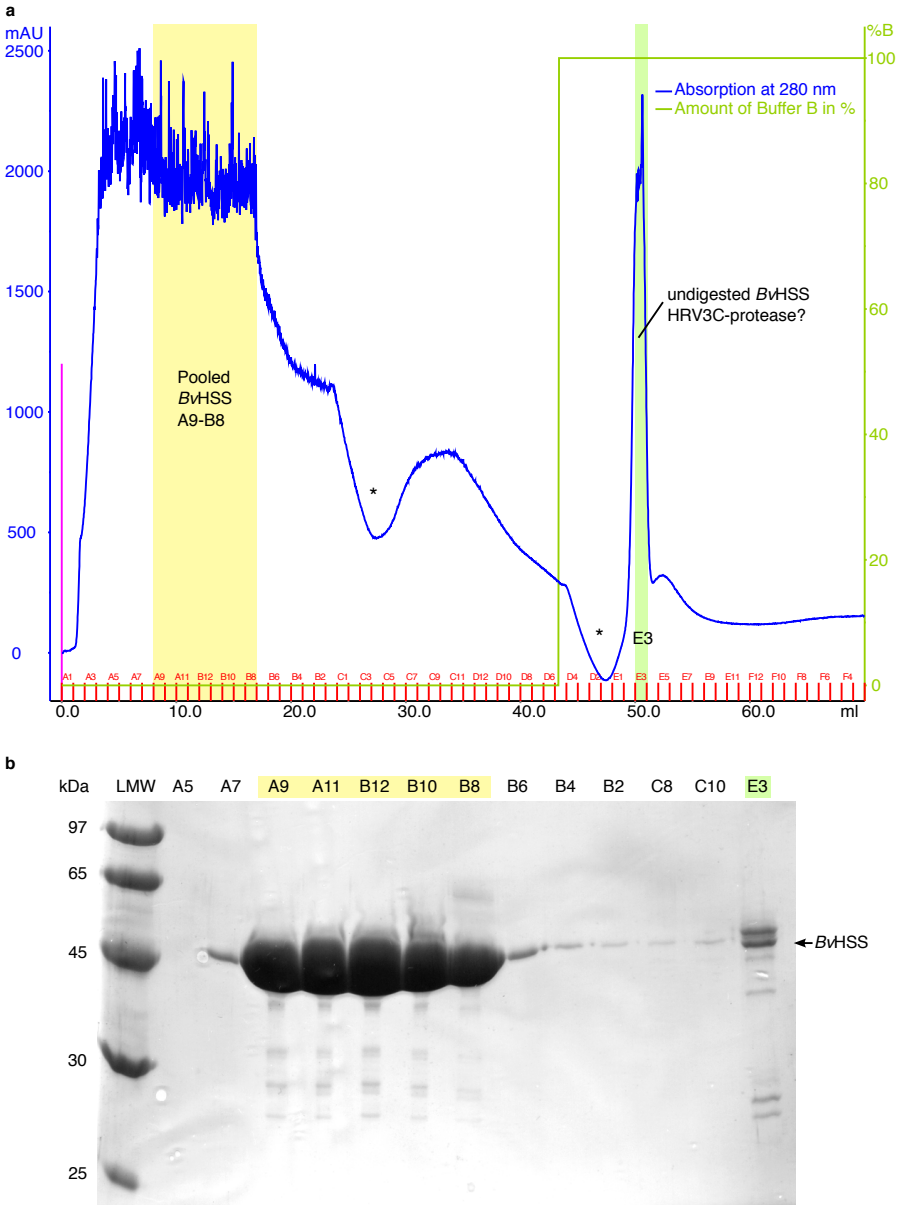

Figure 3.5: Chromatogram of the second affinity chromatography (a) of *Bv*HSS variant H296S and the corresponding analysis of a subset of the collected fraction by SDS-PAGE (b). After removal of the 6xHis-Tag the majority of the *Bv*HSS was found in the flow through fractions A9-B8 (yellow bar) as proven by SDS-PAGE (15%, reducing conditions, expected *Bv*HSS height indicated by arrow). The fraction E2 (green bar) most likely contained undigested *Bv*HSS variant H296S and HRV3C protease and was discarded. The collected fractions are indicated by the red horizontal lines (above the x-axis) and are labeled accordingly in (b). All samples were loaded with matching volumes onto the SDS-PAGE to allow for estimation of the relative protein content. A protein ladder (LMW) was loaded onto the SDS-PAGE for molecular weight estimation. The irregularities of the 280 nm absorption curve (indicated by an asterisk [*]) were caused by a software error during the purification procedure and did not affect the purification. The fluctuations of the absorbance at 280 nm are caused by the high protein amounts in the sample leading to signals beyond the upper detection limit of the UV detector.

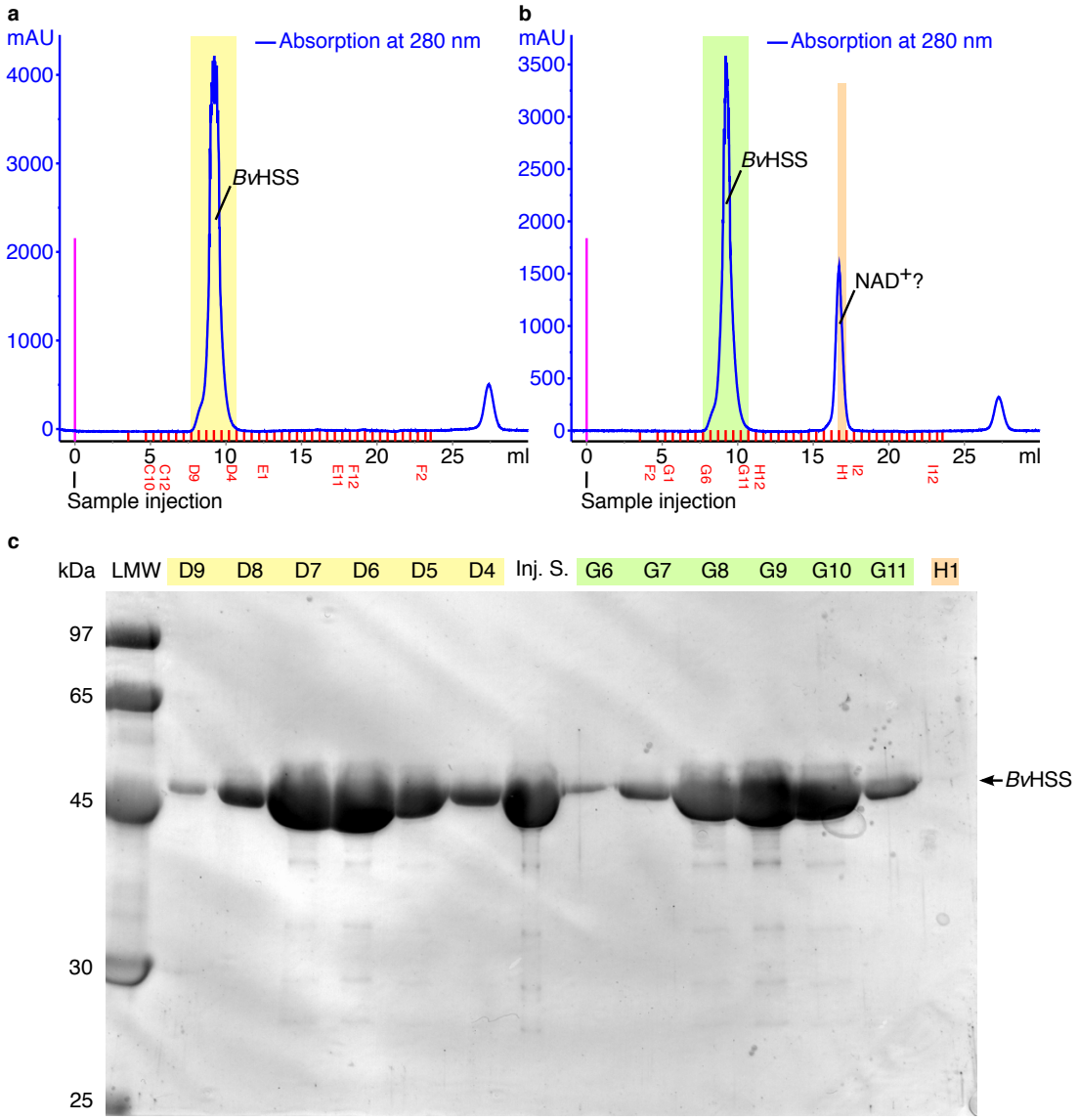

Figure 3.6: Chromatograms of the analytic SEC of the *Bv*HSS variant H296S with (b) and without (a) added NAD^+ and the corresponding analysis of the collected fractions by SDS-PAGE (c). The SEC of the sample without added NAD^+ resulted in a single peak (absorption at 280 nm) containing mainly *Bv*HSS (as proven by SDS-PAGE, expected *Bv*HSS height indicated by arrow, corresponding fractions indicated by a yellow bar). The SEC of the sample with added NAD^+ resulted in two peaks (absorption at 280 nm): The first peak contained mainly *Bv*HSS H296S (as proven by SDS-PAGE, expected size of *Bv*HSS indicated by arrow, corresponding fractions indicated by a green bar) and the second peak did not contain any detectable protein amounts (as proven by SDS-PAGE, corresponding fractions indicated by a orange bar) and presumably represented NAD^+. The SDS-PAGE showed no significant improvement of sample purity after SEC (compare injected sample [Inj. S.] with D6 or G9). All samples were loaded with matching volumes onto the SDS-PAGE (15%, reducing conditions) to allow for estimation of relative protein content. A protein ladder (LMW) was loaded onto the SDS-PAGE for molecular weight estimation. The fluctuations of the absorbance at 280 nm during the FPLC (a, b) are caused by the high protein amounts in the sample leading to signals beyond the upper detection limit of the UV detector.

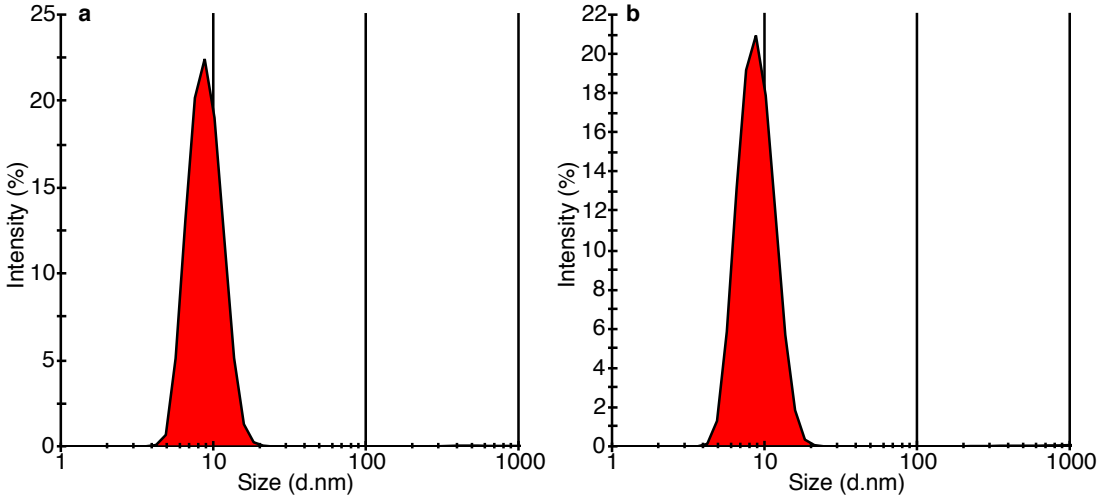

Figure 3.7: Analysis of *Bv*HSS variant H296S sample purity after SEC (a) and prior SEC (b) by dynamic light scattering. The sample after SEC (a) originated from the pooled fractions D7-D5, and G8-G10 of the analytical SECs shown in Fig. 3.6. The sample prior SEC (b) originated from the same purification lot and was supplemented with 2 mM NAD^+. In both measurements only one, comparable peak with a mode of 8.7 nm for the diameter accounting for 99.0% (a, 25.0% polydispersity) and 97.8% (b, 26.6% polydispersity) of total measured signal intensity reflecting a *Bv*HSS dimer with a calculated molecular weight of 113 kDa (a) and 114 kDa (b).

composition and rather related to the performance of the used column. It was not possible to remove the impurities (bands below 50 kDa) from the injected sample. All detectable bands of the injected sample were recovered in samples from peak 1. When comparing both chromatograms of the SECs (estimated retention time to molecular weight dependence, based on the reference chromatograms provided by GE Healthcare, Little Chalfont, United Kingdom) and regarding the results from the SDS-PAGEs, it is most likely that peak 2 represents the NAD^+ added to the injected sample prior to analysis. Because of the small molecular weight (assumed based on retention time) of the compound representing peak 3, further analyses of its identity was not of interest in this context. Regarding the composition of the injected sample, the compound was probably oxidized DTT.

A sample from pooled and concentrated fractions D7 to D5 and G8 to G10 obtained from analytical SEC was analyzed by DLS and compared to an DLS analysis of a *Bv*HSS sample containing 2 mM NAD^+ (prior SEC). The results are shown as a size distribution by intensity graph in Figure 3.7. For both samples one peak with a mode of 8.7 nm for the diameter accounting for 99.0 % (*Bv*HSS after SEC) and 97.8 % (*Bv*HSS prior SEC) of total measured signal intensity. Both samples were classified as fairly polydisperse by the Malvern DLS analysis software with a relative polydispersity of 25.0 % (*Bv*HSS after SEC) and 26.6 % (*Bv*HSS prior SEC). The software estimated the molecular weight of the sample to be 113 kDa (*Bv*HSS after SEC) and 114 kDa (*Bv*HSS prior SEC).

The DLS analyses did not show any significant difference between the samples of *Bv*HSS after and prior SEC. The estimated molecular weight of the detected peak is in agreement with the

reported *Bv*HSS homodimer in solution [theoretical molecular weight 105.8 kDa (Tholl *et al.*, 1996)]. The high purity of the sample was reflected by the observation that beside the one species no other species were detected. The minor impurities already seen in the SEC might be reflected by the polydispersity of the peak.
In conclusion, it was possible to produce the *Bv*HSS in *E. coli* and to purify it in sufficient amounts. Analytic SEC together with DLS measurements showed that the *Bv*HSS was already present at a sufficient purity for crystallization trials after the removal of the 6xHis-tag. A final preparative SEC was not necessary, hence subsequent to 6xHis-tag removal the protein was transferred to fresh buffer, concentrated to 5-6 mg/ml and stored at –80 °C after addition of 2 mM NAD^+ and flash cooling in liquid nitrogen.

3.2 Crystallization of *Bv*HSS

Initial screen for crystallization conditions with JCSG Core Suites I, II, III and IV (Qiagen) led to first small crystals with 100 mM sodium acetate pH 4.6, 200 mM ammonium acetate, 30 % (w/v) PEG 4000 as reservoir solution (Fig. 3.8 a). Manually performed grid screens and replacement of PEG 4000 with PEG 3350 resulted in single crystals of the *Bv*HSS with 100 mM sodium acetate pH 4.6, 100 mM ammonium acetate, 34 % (w/v) PEG 3350 as reservoir solution (Fig. 3.8 b). All attempts in reproducing single crystals under these conditions for soaking with diamines or in diamine-co-crystallization setups led exclusively to spliced needle-shaped crystals growing in haystack-like clusters (Fig. 3.8 c and d). Optimization of crystallization conditions was done using the Additive Screens I, II and III (Hampton Research, Aliso Viejo, California, USA). The additive non-detergent sulfobetaine-201/3-pyridin-1-ium-1-ylpropane-1-sulfonate (NDSB-201, G Biosciences, St. Louis, Missouri, USA) improved the crystal shape from needle- to rod-shaped crystals. The overall size of these rods could be increased by replacing PEG 3350 with PEG 10000 (Fig. 3.8 e). In conjunction, this led to conditions (100 mM sodium acetate pH 4.6 – 4.8, 150 mM ammonium acetate, 22-26 % (v/v) PEG 10000, 150 - 300 mM NDSB-201) reproducibly generating rod-shaped crystals sufficient for subsequent structure determination (Fig. 3.8 f and Table 3.1 for detailed crystallization conditions).

3.3 Overall Structure of *Bv*HSS

*Bv*HSS structure was solved from crystals belonging to space group $P2_12_12_1$ with bound NAD^+ (Protein Data Bank [PDB] ID 4PLP) diffracting up to 1.49 Å. Crystals from *Bv*HSS and *Bv*HSS variants with bound NAD^+ in complex with various polyamines all belonged to space group $P22_12_1$ with cell parameters in approximately the same order of magnitude diffracting up to 1.27 Å. Detailed data collection statistics are summarized in Table 3.2 and 3.3.
The crystal structure of *Bv*HSS was identified as a dimer with bound NAD^+ (PDB ID 4PLP) in the asymmetric unit (Fig. 3.9 a). The first four amino acids could not be traced for each of the two protein subunits. In each subunit, twelve residues (2 % of residues per subunit) were only

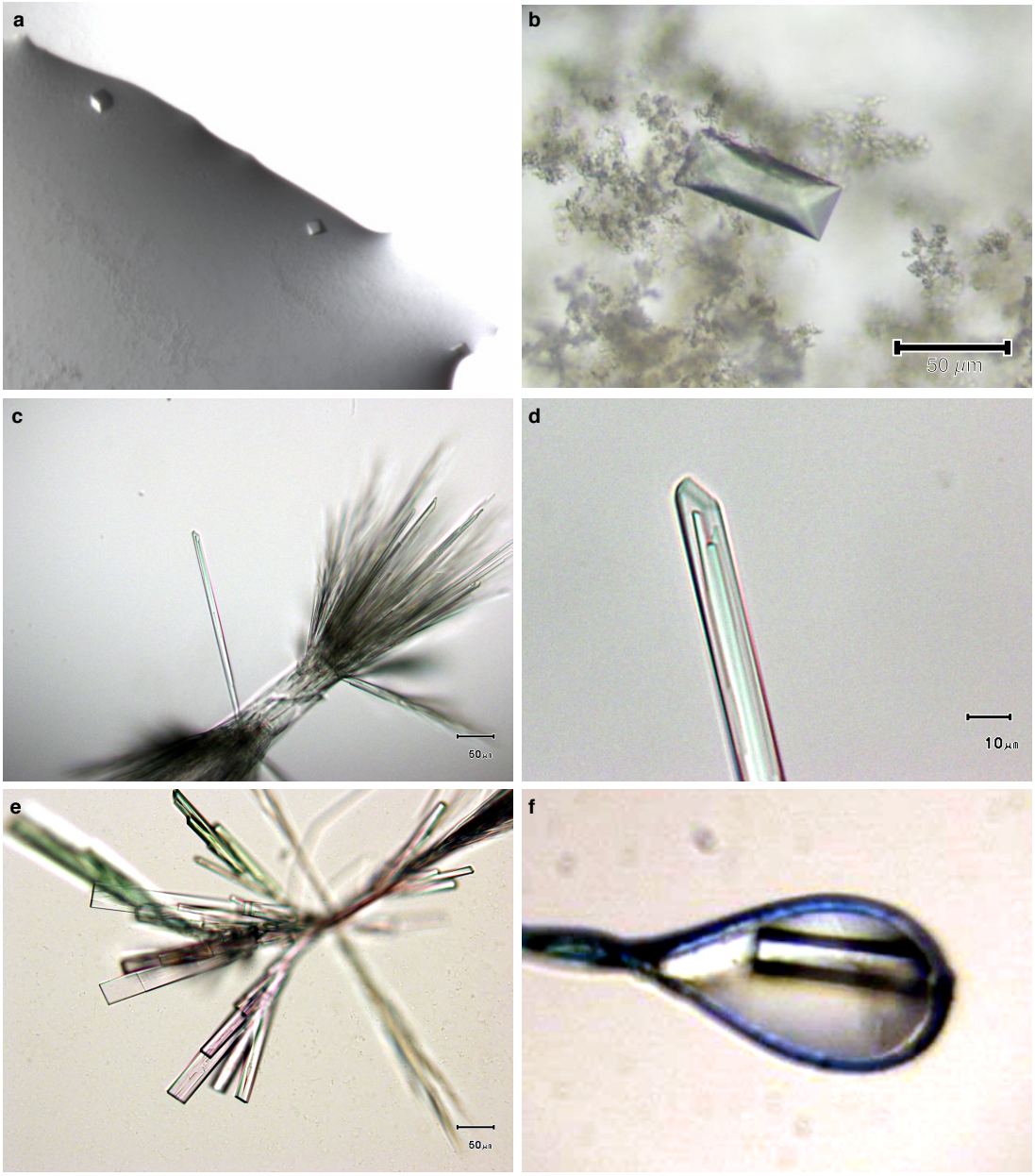

Figure 3.8: Representative images of *Bv*HSS crystals. (a) Initial crystals observed under crystallization condition screening. (b) Representative single crystal of *Bv*HSS wild-type without added polyamines as used for determination of the structure with PDB ID 4PLP. (c) Spliced, needle-shaped crystals growing in haystack-like clusters observed after attempted reproduction of crystallization conditions leading to single crystals shown in (b). (d) Magnifaction of one of the spliced, needle-shaped crystals showen in (c). (e) Rod-shaped crystals growing in clusters after crystallization condition improvement. (f) Exemplary single rod-shaped crystal in a cryoloop after manual disintegration of a cluster and flash-cooling in liquid nitrogen.

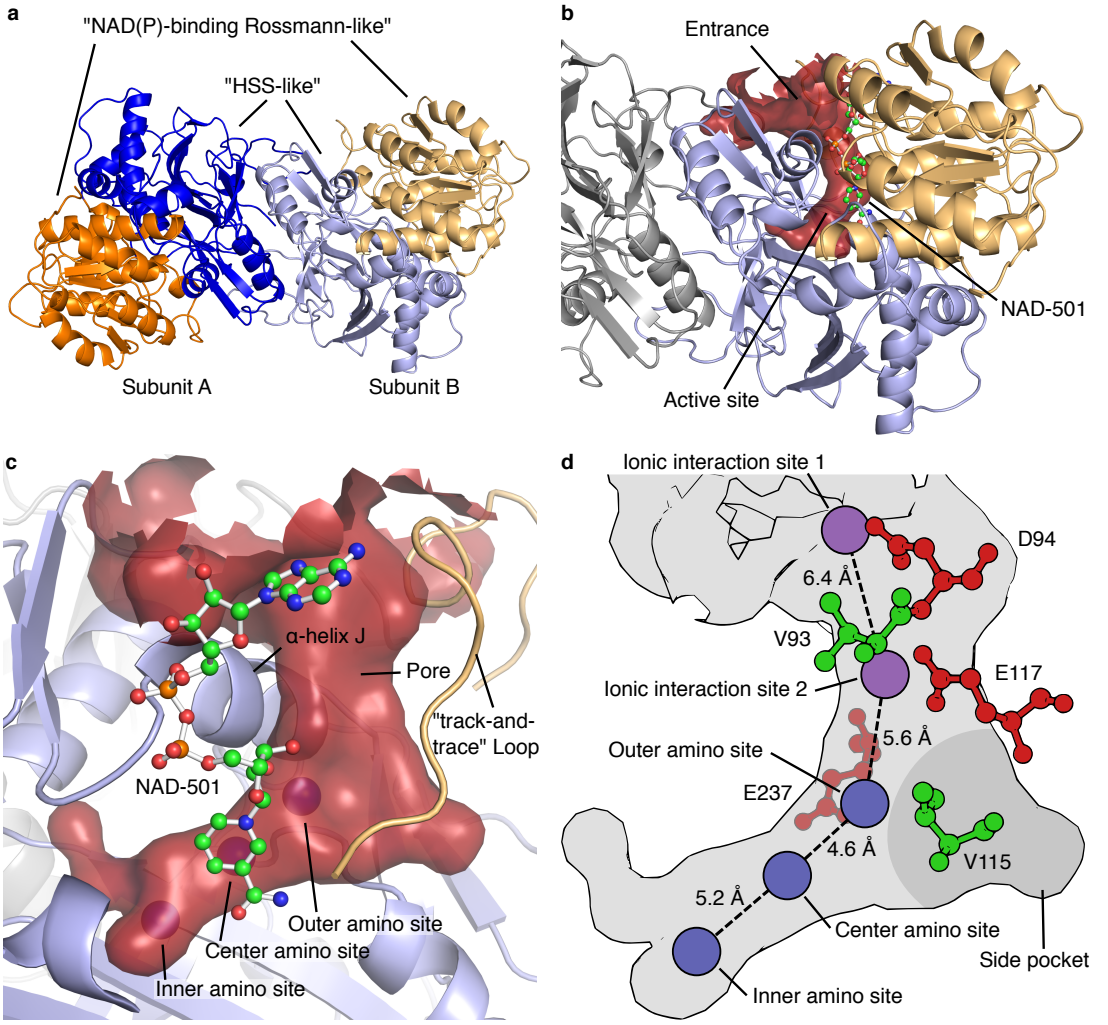

Figure 3.9: Overall structure of the homodimeric *Bv*HSS. (a) Cartoon representation of the *Bv*HSS (PDB ID 4PLP) dimer with domain 1 ("NAD(P)-binding Rossmann-like") in orange (subunit A)/light orange (subunit B) and domain 2 ("homospermidine-synthase (HSS)-like") in blue (subunit A)/light blue (subunit B). (b+c) Substrate binding pocket displayed as a surface-rendered cavity in red with adjacently bound NAD^+ (in ball-and-stick representation). (c) Outer, center, and inner amino sites are indicated as blue spheres, and the "track-and-trace" loop is given as a cartoon representation in light orange. (d) Representation of the substrate-binding pocket shown in (c). Amino sites are displayed as blue circles, and ionic interaction sites are displayed as violet circles. Amino acids providing the "ionic slide" (ball-and-stick representation) with acidic side chains are colored in red, and those with non-polar side chains are colored in green. The approximate position of the side pocket on the rear side of the binding pocket is indicated as a dark gray area.

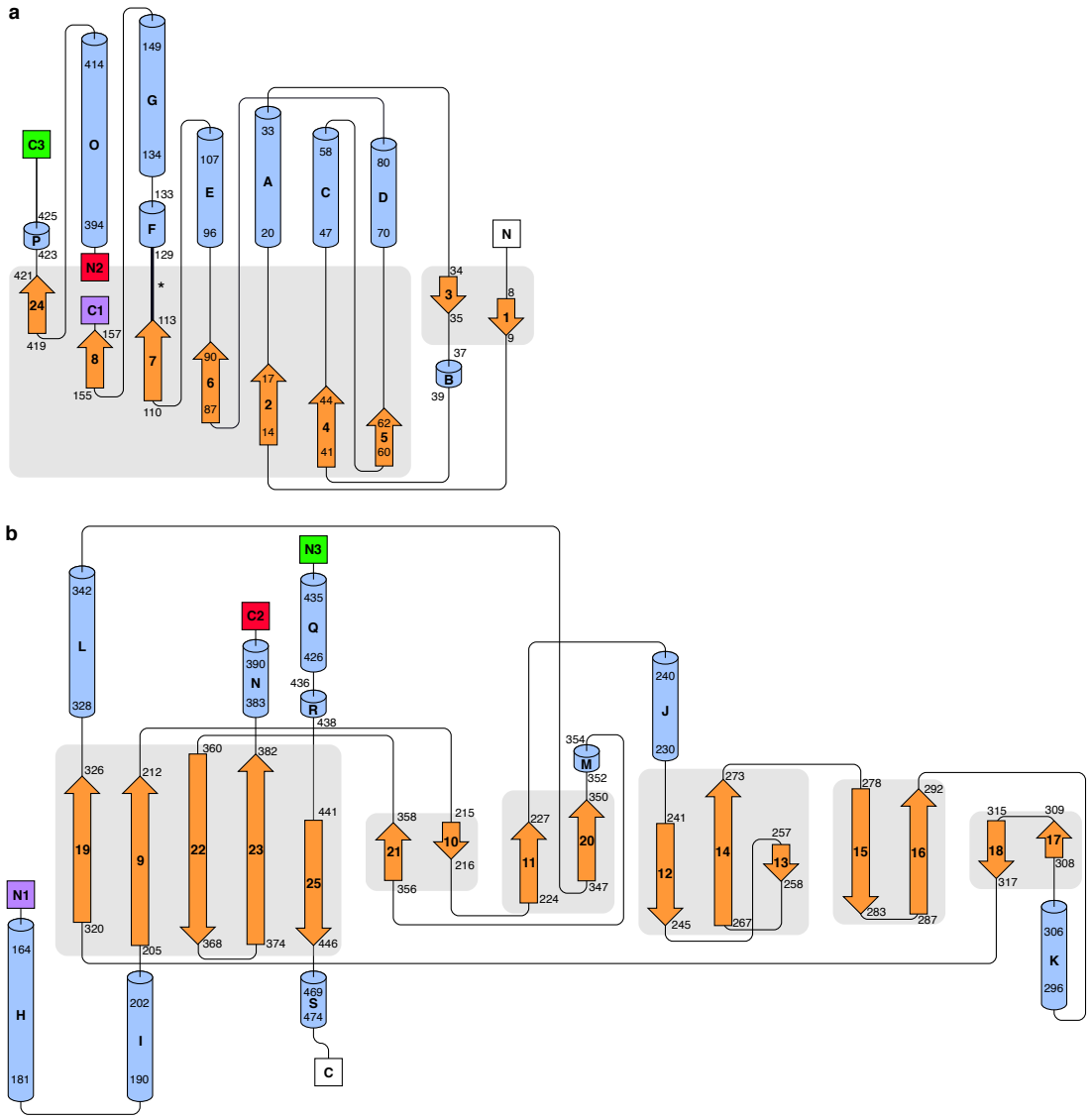

Figure 3.10: Topology diagram of *Bv*HSS. The diagram was generated with the program Pro-origami (Stivala *et al.*, 2011) by using secondary structure information embedded into the PDB file for *Bv*HSS subchain A (PDB ID 4PLP). α-helixes (numbered alphabetically A to S) are shown as cylinders, and β-strands (numbered 1 to 25) are shown as arrows. The numbers of the first and last residue of every secondary structure element are given at the start and end point of each representation. β-sheets are indicated as boxes. (a) Domain 1 – "NAD(P)-binding Rossmann-like" domain. The "track-and-trace" loop is represented by a thick black line and indicated by an asterisk. (b) Domain 2 – "homospermidine-synthase–like" domain.

Table 3.1: Crystallization conditions and polyamine composition of *Bv*HSS crystals: Reservoir solution consisted of 100 mM sodium acetate buffer pH 4.6 - 4.8 and 100 mM (*Bv*HSS w/o substrate; PDB ID 4PLP) or 150 mM (all other crystals) ammonium acetate in addition to substances listed in table. Protein solution consisted of approximately 4 mg/ml *Bv*HSS in standard buffer (*Bv*HSS w/o substrate; PDB ID 4PLP) or in 33 mM BIS-TRIS propane pH 9, 17 mM KCl, 6.7 mM DTT, 1.3 mM NAD (all other crystals).

Protein	Polyamine(s) in protein solution (co-crystallization)	Polyamine soaked	Polyamine identified in active site	Reservoir pH	Reservoir PEG (w/v)	Reservoir NDSB-201
*Bv*HSS PDB ID 4PLP	-	-	-	4.6	34 % PEG 3350	-
*Bv*HSS PDB ID 4TVB	0.2 M DAP	300 s 0.2 M PUT	HSP, PUT (transition close states)	4.8	22 % PEG 10000	250 mM
*Bv*HSS PDB ID 4XR4	0.2 M AGM	-	-	4.8	22 % PEG 10000	150 mM
*Bv*HSS PDB ID 4XQ9	0.2 M CAD	-	-	4.8	22 % PEG 10000	150 mM
*Bv*HSS PDB ID 4XQC	0.2 M DAP, 0.2 M PUT	-	DAP	4.6	24 % PEG 10000	300 mM
*Bv*HSS H296S PDB ID 4XQE	0.2 M AGM	-	AGM	4.6	22 % PEG 10000	250 mM
*Bv*HSS H296S PDB ID 4XRG	0.2 M AGM	300 s 0.2 M PUT	AGM+PUT	4.6	24 % PEG 10000	300 mM
*Bv*HSS E237Q PDB ID 4XQG	0.2 M AGM, 0.2 M PUT	-	-	4.6	24 % PEG 10000	300 mM

poorly represented by electron density as indicated by residue type and resolution normalized real space R-values (RSRZ) given in the worldwide PDB (wwPDB) structure validation report (Kleywegt *et al.*, 2004; Read *et al.*, 2011). All related residues were located at the protein surface within loop regions. The interface area of the dimer was calculated as 1705 Å² for subunit A and 1687 Å² for subunit B by PDBsum indicating a stable dimer (de Beer *et al.*, 2014). The *Bv*HSS subunit consists of two domains as determined by CATH (Sillitoe *et al.*, 2013): one "NAD(P)-binding Rossmann-like" domain (domain 1, residues 3 - 163 and 394 - 425) and one "homospermidine-synthase-like domain" (domain 2, residues 164 – 395 and 426 – 477) as shown in Figure 3.9 a and 3.10. Both subunits are structurally very similar with a root-mean-square difference (RMSD) of 0.8 Å² (structure with PDB ID 4PLP, complete residues 3 - 476 without hydrogens, alternate location A, for details see Table 3.4). Subsequently, determined structures of *Bv*HSS and *Bv*HSS variants with bound NAD^+ and different bound polyamines (compare Table 3.1) were found to be highly similar to the *Bv*HSS structure with PDB ID 4PLP (RMSDs in Table 3.5, overlay in Fig. 3.11). Slightly different relative orientations of subunit A to subunit B were observed for all *Bv*HSS structures. The most prominent differences were ascertained for a major fraction (residues Leu-120 to Pro-130) of a loop region (residues Thr-114 to Pro-130, further referred to herein as "track-and-trace" loop, see also Fig. 3.9 c, Fig. 3.10, and Fig. 3.11) between the holoenzyme (PDB ID 4PLP) and the substrate (PUT/HSP)-bound form (PDB ID 4TVB). Alignment of HSS from *L. pneumophila* subunit A (PDB ID 2PH5

(Forouhar)) with *Bv*HSS subunit A (PDB ID 4PLP) resulted in an RMSD of 1.1 Å² (362 to 362 C_α atoms, after 5 cycles of the PyMOLs “super” algorithm) indicating similar 3D structures as expected from the sequence alignment.
The bacterial HSS is supposed to be evolutionary related to CA(N)SDH, lysine 6-dehydrogenase, saccharopine dehydrogenase, and aspartate dehydrogenase (Shaw *et al.*, 2010). This relationship is supported by the superposition of a bacterial saccharopine dehydrogenase from *Wolinella succinogenes* (EC: 1.5.1.7, PDB ID 4INA (Vorobiev) RMSD 3.2 Å², 224 to 224 C_α atoms, after 5 cycles of the PyMOLs “super” algorithm) and two eukaryotic saccharopine dehydrogenases/reductases from *Saccharomyces cerevisiae* and *Magnaporthe grisea* (EC: 1.5.1.10, PDB ID 2AXQ (Andi et al., 2006) with RMSD 3.6 Å², 127 to 127 C_α atoms and PDB ID 1E5Q (Johansson *et al.*, 2000) with RMSD 2.9 Å², 116 to C_α atoms, both after 5 cycles of the PyMOLs “super” algorithm) with *Bv*HSS (PDB ID 4PLP) subunit A indicating a similar overall fold (see Fig. 3.11 for a side-by-side comparisson).

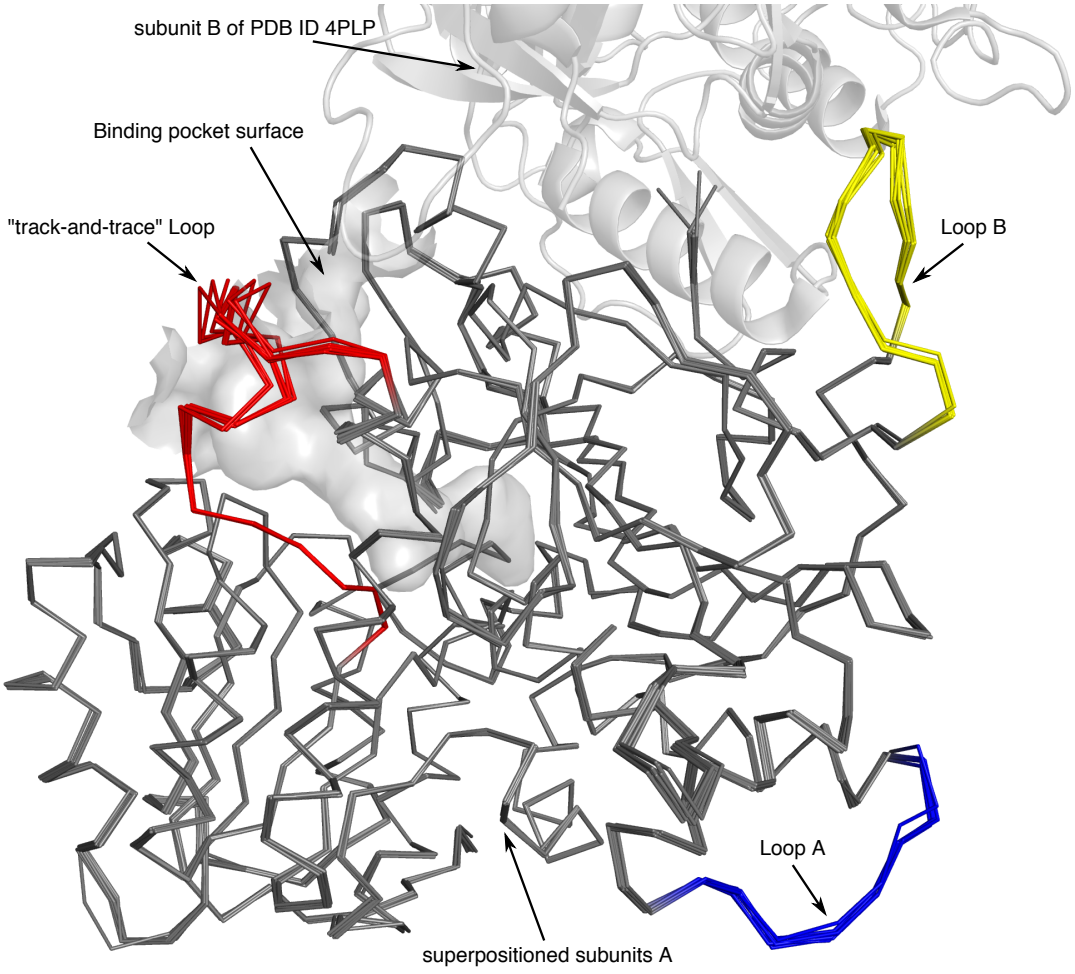

Figure 3.11: Superposition of all *Bv*HSS structures. The subunit A (represented as C_α-ribbon) of all *Bv*HSS structures was superimposed onto the subunit A of the *Bv*HSS structure with PDB ID 4PLP by using the “super” algorithm as implemented in PyMOL. The most prominent differences were ascertained for certain loop regions: The “track-and-trace” loop (red), loop A (blue), and loop B (yellow, for details see Table 3.5). For better orientation, the binding pocket surface and the subunit B (as cartoon representation) of the *Bv*HSS structure with PDB ID 4PLP are given in light grey.

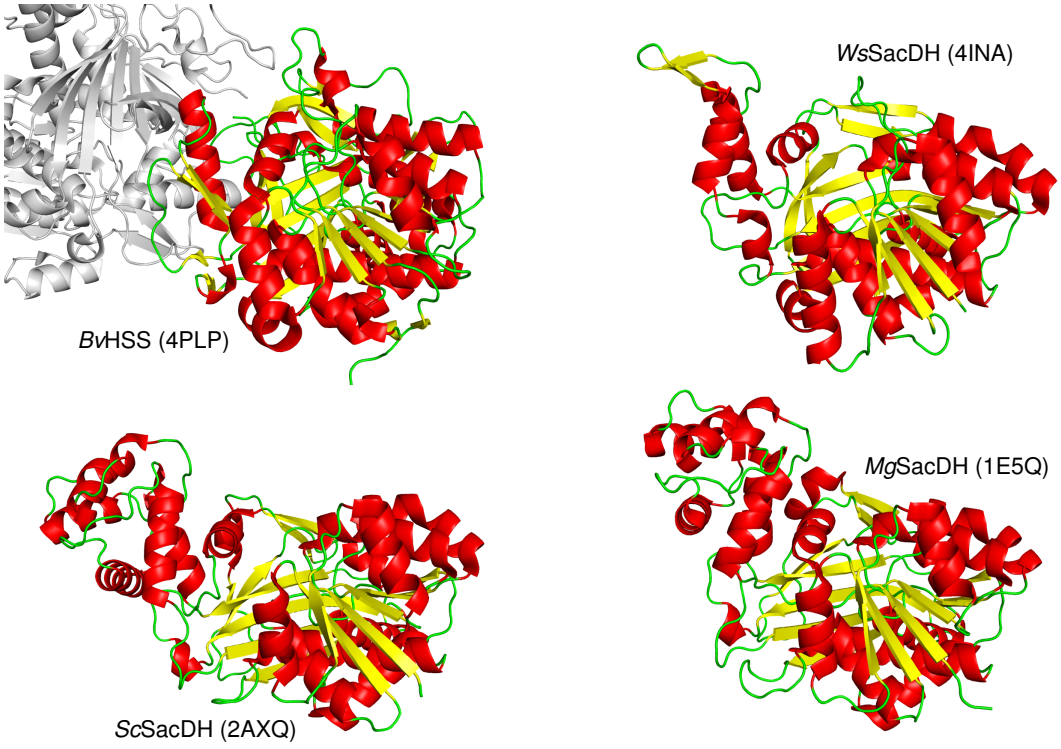

Figure 3.12: Comparison of *Bv*HSS with evolutionary related SacDHs. The superimposed subchains A of the structures of *Bv*HSS (PDB ID 4PLP), *Ws*SacDH (PDB ID 4INA), *Sc*SacDH (PDB ID 2AXQ), and *Mg*SacDH (PDB ID 1E5Q) are shown side-by-side in the same orientation as a cartoon representation colored according to the secondary structure (helix = red, β-sheet = yellow, loop = green). Superposition was done with the "super" algorithm as implemented in PyMOL by using the C_α atoms. For better orientation, the subunit B (as cartoon representation) of *Bv*HSS is given in light grey.

Table 3.2: Data collection and refinement statistics. Each structure is based on data collected from one crystal. Values in parenthesis are for highest resolution shell. Model refinements were performed with data sets containing all collected reflections as deposited in the PDB. The resolution cut-offs were only applied in the final steps of the model refinement. The low resolution cut-off of 10 Å was empirically chosen for all data sets to omit only a minimum of reflections and allow for better comparison of the data sets. The high resolution cut-offs were chosen based on significant $CC_{1/2}$ as determined by the software XDS as recently described by Karplus and Diederichs (2012).

	*Bv*HSS w/o substrate	*Bv*HSS with DAP (co-cryst.), PUT (soak)	*Bv*HSS with AGM (co-cryst.)	*Bv*HSS with CAD (co-cryst.)	*Bv*HSS with DAP, PUT (co-cryst.)	*Bv*HSS H296S with AGM (co-cryst.)	*Bv*HSS H296S with AGM (co-cryst.), PUT (soak)	*Bv*HSS E237Q with AGM, PUT (co-cryst.)
	PDB ID 4PLP	PDB ID 4TVB	PDB ID 4XR4	PDB ID 4XQ9	PDB ID 4XQC	PDB ID 4XQE	PDB ID 4XRG	PDB ID 4XQG
Space group	$P2_12_12_1$	$P22_12_1$	$P22_12_1$	$P22_12_1$	$P22_12_1$	$P22_12_1$	$P22_12_1$	$P22_12_1$
Cell dimensions								
a, *b*, *c* [Å]	70.0, 109.8, 193.0	59.5, 109.3, 157.2	54.9, 108.6, 161.3	60.1, 110.7, 157.5	60.1, 109.8, 157.3	60.3, 110.1, 157.9	60.0, 110.2, 157.5	59.8, 109.3, 157.6
α, β, γ [°]	90, 90, 90	90, 90, 90	90, 90, 90	90, 90, 90	90, 90, 90	90, 90, 90	90, 90, 90	90, 90, 90
Resolution (Å)	1.49	1.69	1.63	1.6	1.27	1.3	1.3	1.42
R_{merge}	0.168 (2.715)	0.2576 (2.21)	0.09 (0.751)	0.228 (2.678)	0.145 (1.338)	0.156 (3.515)	0.142 (3.11)	0.096 (0.927)
$\left\langle \frac{\langle I \rangle}{\sigma(\langle I \rangle)} \right\rangle$	5.7 (0.4)	8.4 (0.8)	13.9 (1.8)	6.2 (0.3)	7.7 (1.1)	7.2 (0.5)	6.1 (0.4)	10.8 (1.4)
Completeness [%]	99.16 (98.68)	98.08 (80.81)	98.22 (82.81)	91.78 (53.97)	95.92 (89.68)	99.3 (98.25)	99.63 (99.25)	96.67 (79.06)
Redundancy	3.7 (3.5)	12.8 (8.6)	6.3 (4.2)	5.7 (2.2)	6.9 (6.7)	6.6 (6.6)	5.3 (4.2)	6.6 (4.8)
Refinement								
Resolution [Å]	9.996 - 1.49 (1.54 - 1.49)	9.99 - 1.69 (1.75 – 1.69)	9.998 - 1.63 (1.68 - 1.63)	9.989 - 1.6 (1.66 - 1.6)	9.997 - 1.27 (1.32 - 1.27)	10 - 1.3 (1.35 - 1.33)	9.999 - 1.3 (1.35 - 1.3)	9.997 - 1.42 (1.47 - 1.42)
No. reflections (unique)	239366 (23587)	112717 (9183)	119073 (9911)	126905 (7384)	261583 (24265)	254864 (24993)	254501 (25125)	188913 (15316)
R_{work} / R_{free}	0.191 / 0.225 (0.383 / 0.394)	0.179 / 0.206 (0.312 / 0.338)	0.136 / 0.171 (0.234 / 0.261)	0.161 / 0.204 (0.365 / 0.364)	0.15 / 0.182 (0.278 / 0.307)	0.147 / 0.185 (0.351 / 0.381)	0.16 / 0.198 (0.368 / 0.394)	0.129 / 0.161 (0.257 / 0.289)
No. atoms								
Protein	7573	7457	7504	7503	7563	7653	7549	7537
Ligand/ion	92	118	219	96	166	217	165	219
Water	1035	1298	984	1307	1490	1086	1155	1146
***B*-factors** [Å^2]								
Protein	27.9	20.4	19.7	22.3	13.8	19.3	21.4	17.7
Ligand/ion	21.8	16.7	29.5	20.2	16.7	24	23.4	25.1
Water	42.3	29.8	34	36.6	27.3	34.2	36.1	32.1
RMS deviations								
Bond lengths [Å]	0.012	0.01	0.020	0.008	0.01	0.012	0.009	0.012
Bond angles [°]	1.41	1.17	1.34	1.15	1.31	1.38	1.26	1.36

Table 3.3: Additional statistics of data refinement. Values in parenthesis are for highest resolution shell. Model refinements were performed with data sets containing all collected reflections as deposited in the PDB. The resolution cut-offs were only applied in the final steps of the model refinement. The low resolution cut-off of 10 Å was empirically chosen for all data sets to omit only a minimum of reflections and allow for better comparison of the data sets. The high resolution cut-offs were chosen based on significant $CC_{1/2}$ as determined by the software XDS as recently described by Karplus and Diederichs (2012).

	*Bv*HSS w/o substrate PDB ID 4PLP	*Bv*HSS with DAP (co-cryst.), PUT (soak) PDB ID 4TVB	*Bv*HSS with AGM (co-cryst.) PDB ID 4XR4	*Bv*HSS with CAD (co-cryst.) PDB ID 4XQ9	*Bv*HSS with DAP, PUT (co-cryst.) PDB ID 4XQC	*Bv*HSS H296S with AGM (co-cryst.) PDB ID 4XQE	*Bv*HSS H296S with AGM (co-cryst.), PUT (soak) PDB ID 4XRG	*Bv*HSS E237Q with AGM, PUT (co-cryst.) PDB ID 4XQG
Wavelength of data collection [Å]	0.918	1.23953	1.23953	0.97628	0.976261	0.9763	0.9763	1.03322
Resolution [Å]	9.996 - 1.49 (1.54 - 1.49)	9.99 - 1.69 (1.75 – 1.69)	9.998 - 1.63 (1.68 - 1.63)	9.989 - 1.6 (1.66 - 1.6)	9.997 - 1.27 (1.32 - 1.27)	10 - 1.3 (1.35 - 1.33)	9.999 - 1.3 (1.35 - 1.3)	9.997 - 1.42 (1.47 - 1.42)
CC*	0.998 (0.549)	0.999 (0.607)	1 (0.861)	0.997 (0.296)	0.999 (0.692)	0.999 (0.463)	0.999 (0.387)	1 (0.765)
CC_{work}	0.973 (0.449)	0.968 (0.607)	0.976 (0.822)	0.976 (0.344)	0.976 (0.685)	0.979 (0.453)	0.977 (0.386)	0.978 (0.753)
CC_{free}	0.958 (0.408)	0.965 (0.518)	0.964 (0.751)	0.962 (0.243)	0.967 (0.672)	0.971 (0.394)	0.967 (0.323)	0.972 (0.675)
Ramachandran outliers [%]	0.1	0	0	0	0	0	0	0

Table 3.4: Structure alignment of *Bv*HSS subunit A to subunit B: Aligned with the “super” algorithm as implemented in the program PyMOL (5 cycles) to align subunit B residues 3-476 (complete residue without hydrogens, always using alternate location A) to chain A of respective *Bv*HSS structure; all other RMSDs calculated with the rms_cur function as implemented in the program PyMOL for complete residues without hydrogens, always using alternate location A. The respective residue range and the used alignment method are given in round parenthesis in the first row of the table. The number of atoms of the aligned parts of both molecules used to calculate each RMSD is given in parenthesis.

	Subunit B to A [Å^2] (residues 3-476 , super)	Subunit B to A [Å^2] (residues 3-476 , rms_cur)	"Track-and-trace" loop subunit B to A [Å^2] (residues 120-130, rms_cur)	Subunit B to A [Å^2] (NAD(H), rms_cur)
*Bv*HSS w/o substrate				
PDB ID 4PLP	0.15 (2786 atoms)	0.81 (3699 atoms)	1.72 (93 atoms)	0.58 (44 atoms)
*Bv*HSS with DAP (co-cryst.), PUT (soak)				
PDB ID 4TVB	0.13 (2853 atoms)	0.68 (3699 atoms)	0.57 (93 atoms)	0.57 (44 atoms)

Table 3.5: Alignment of all *Bv*HSS structures to *Bv*HSS structure with the PDB ID 4PLP: Aligned with the “super” algorithm as implemented in the program PyMOL (5 cycles) to align subunit A residues 3-476 (complete residue without hydrogens, always using alternate location A) to 4PLP subunit A; all other RMSDs were subsequently calculated for the superimposed proteins with rms_cur function as implemented in the program PyMOL for complete residues without hydrogens, always using alternate location A. The respective residue range and the used alignment method are given in round parenthesis in the first row of the table. The number of atoms of the aligned parts of both molecules used to calculate each RMSD is given in parenthesis.

	Subunit A [Å^2] (residues 3-476 , super)	Subunit A to subunit A of 4PLP [Å^2] (residues 3-476 , rms_cur)	Subunit B to subunit B of 4PLP [Å^2] (residues 3-476 , rms_cur)	“Track-and-trace” loop subunit A [Å^2] (residues 120-130, rms_cur)	Loop A subunit A [Å^2] (residues 181-188, rms_cur)	Loop B subunit A [Å^2] (residues 453-465, rms_cur)
*Bv*HSS with DAP (co-cryst.), PUT (soak)						
PDB ID 4TVB	0.21 (2951 atoms)	0.80 (3699 atoms)	1.51 (3699 atoms)	2.88 (93 atoms)	1.45 (55 atoms)	0.78 (98 atoms)
*Bv*HSS with AGM (co-cryst.)						
PDB ID 4XR4	0.23 (3122 atoms)	0.78 (3691 atoms)	1.13 (3691 atoms)	2.81 (93 atoms)	1.76 (55 atoms)	0.46(98 atoms)
*Bv*HSS with CAD (co-cryst.)						
PDB ID 4XQ9	0.18 (2990 atoms)	0.66 (3699 atoms)	1.44 (3699 atoms)	1.67(93 atoms)	1.48(55 atoms)	0.81(98 atoms)
*Bv*HSS with DAP, PUT (co-cryst.)						
PDB ID 4XQC	0.21(3068 atoms)	0.69(3699 atoms)	1.48(3699 atoms)	1.72(93 atoms)	1.68(55 atoms)	0.90(98 atoms)
*Bv*HSS H296S with AGM (co-cryst.)						
PDB ID 4XQE	0.22(3035 atoms)	0.73(3689 atoms)	1.49(3689 atoms)	1.42(93 atoms)	1.70(55 atoms)	0.80(98 atoms)
*Bv*HSS H296S with AGM (co-cryst.), PUT (soak)						
PDB ID 4XRG	0.22(3125 atoms)	0.71(3689 atoms)	1.04(3689 atoms)	1.24(93 atoms)	1.90(55 atoms)	0.62(98 atoms)
*Bv*HSS E237Q with AGM, PUT (co-cryst.)						
PDB ID 4XQG	0.22(2988 atoms)	0.73(3690 atoms)	1.59(3690 atoms)	1.72(93 atoms)	1.55(55 atoms)	0.87(98 atoms)

3.4 NAD Binding Site

Despite being a prosthetic group, NAD^+ is not covalently bound to *Bv*HSS. It is coordinated through hydrogen bonding via residues Ser-21, Ile-22, Ser-230 (phosphate), Asp-45, Val-66 (adenosine), Ser-92, Thr-114, Ala-161, Asn-162, and Pro-163 [nicotineamide riboside, see also Fig. 3.13 for a graphic representation of these interactions generated with LigPlot+ (Laskowski and Swindells, 2011)]. The phosphate-binding motif (^{18}GFGSIG^{23}) is located in the loop connecting β-strand 2 and α-helix A of the Rossmann fold. The adenosine part of NAD^+ is bound via loop regions located between β-strand 4, 5, 6 and α-helix C, D, E. Nicotineamide-riboside-binding residues are found in loop regions between β-strand 7 and 8 and α-helix F and O.

3.5 Characteristics of the Binding Pocket of *Bv*HSS

The volume and the surface of the binding pocket were calculated based on artificial water molecule coordinates generated with the software HOLLOW (Ho and Gruswitz, 2008) by filling the interior of the protein with dummy atoms (1.4 Å radius) on a grid (spacing 0.2 Å). Water molecules of the respective crystal structure of *Bv*HSS present inside or in the direct vicinity of the generated volume were manually added to the artificial water molecules prior to surface calculation. The pocket is a “boot-shaped” cavity that is approximately 21 Å deep (Fig. 3.9 d). The entry to the pocket is formed by part of the “track-and-trace” loop (residues Phe-122 to Asp-125) and the α-helix J at the protein surface (Fig. 3.9 b and c). The innermost end lies near amino acids Asn-162 and Glu-210. The active site is situated between residues Asn-162, Trp-229, Glu-237, His-296, and the nicotine amide ring of NAD^+ at the narrow end of the pocket (Fig. 3.14 for all residues or Fig. 3.15 for distances). Residues Val-115, Val-116, Tyr-123, Asn-135, Leu-138, Pro-163, Gln-240, Thr-295, and Asn-297 form a side pocket at the “heel” of the “boot-shaped” binding pocket, which is filled with six ordered water molecules of which five occur in a nearly planar and equidistant five-membered ring (Fig. 3.16). At least five amino acids (Val-93, Glu-117, Tyr-123, Gly-233, and Ser-236) form a pore at the binding pocket entrance. Based on these observations, four variants of *Bv*HSS (N162D, E237Q, H296S, and E298Q) have been generated for further characterization of residues within the active site. All side chains of these functionally relevant residues (with the exception of Glu-298) participate in forming the active site (Fig. 3.15 and Fig. 3.21). Residue Glu-298 has been chosen based on direct interaction with the active site residue His-296. All four variants of *Bv*HSS lead to enzymatically inactive but soluble proteins. The structure of the *Bv*HSS variant H296S with bound agmatine (PDB ID 4XQE) has revealed two alternative conformations for the “track-and-trace” loop and Ser-236 (α-helix J, Fig. 3.17). These result in at least two different possible dimensions of the pore opening suggesting a locking or a substrate sensing and discriminating mechanism at the binding pocket entrance. Closing or narrowing might occur by the bending of the “track-and-trace” loop resulting in a slight rotation of the side chain of Tyr-123 deeper into the pocket and towards Glu-117, accompanied by a side chain rotation of Ser-236 towards the pocket entrance. Thus, the ellipsoid-shaped

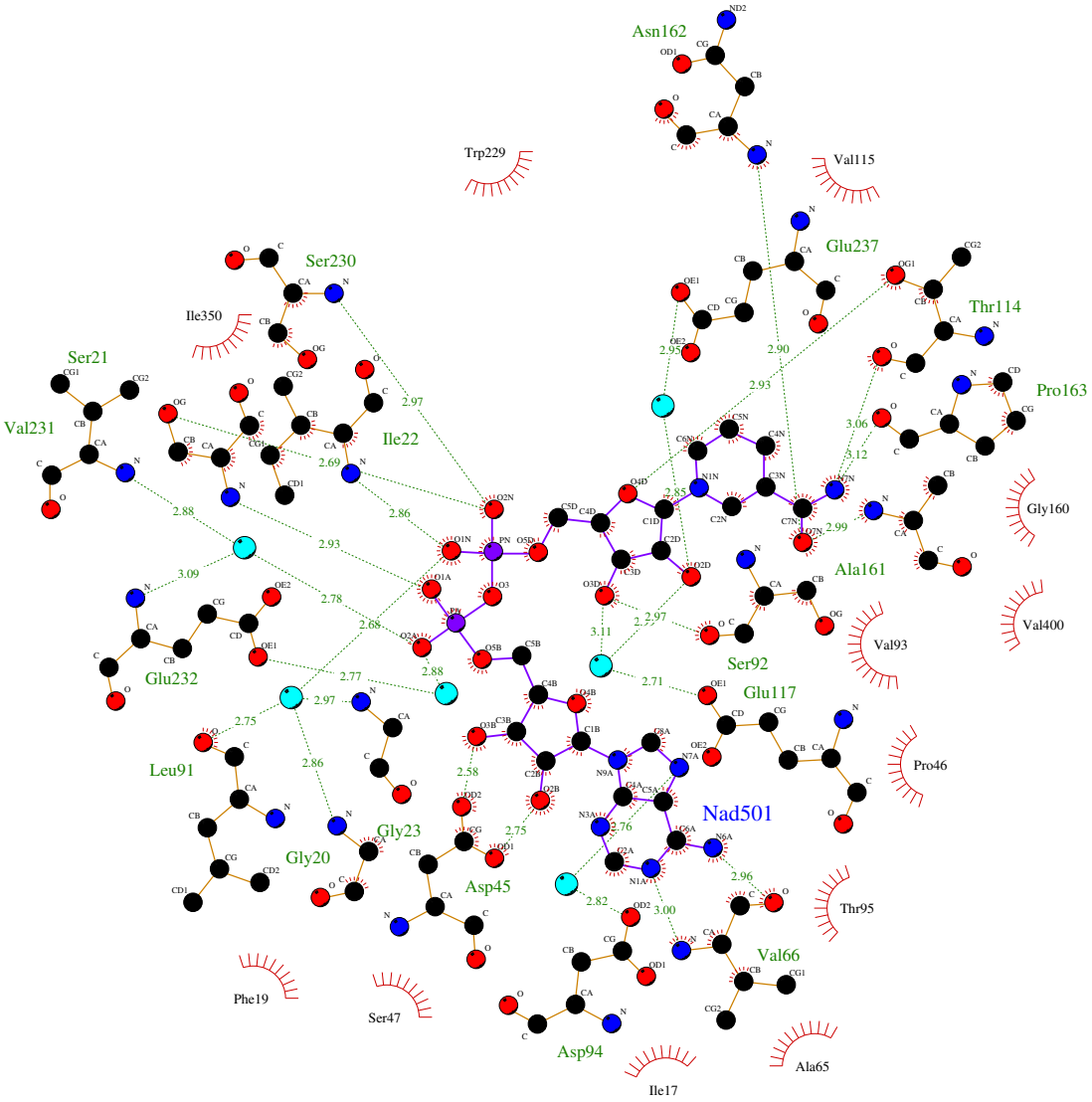

Figure 3.13: Interactions between *Bv*HSS and the ligand NAD^+. Shown are 2D circle-and-line representations of NAD^+ together with relevant amino acids of *Bv*HSS. The hydrophobic interactions (red spoked arcs) and the hydrogen bonds (green dashed lines with distances in Å) between the amino acids of *Bv*HSS and NAD^+ are shown based on the structures with PDB ID 4PLP. The atoms presented as circles are color coded: carbon = black, oxygen = red, nitrogen = blue, phosphor = purple. The bonds between ligand atoms are colored in purple and between amino acids colored in orange. Water molecules are represented as cyan colored circles. Image was generated with LigPlot+.

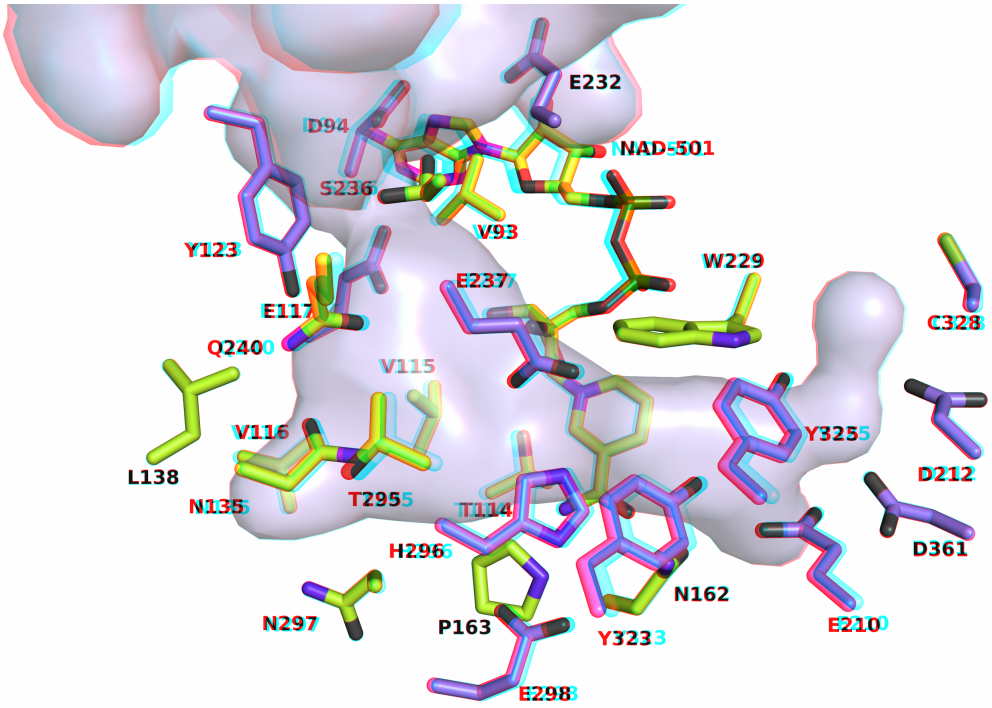

Figure 3.14: 3D stereoscopic visualization of all relevant residues near the binding pocket of *Bv*HSS.The substrate binding pocket is displayed as a surface-rendered cavity in light blue with the adjacently bound NAD^+ and the side chains including the C_α carbons of the relvant residues (in stick representation). The carbons of residues with titratable groups are colored in blue (see also Table 3.6), all other carbons are colored in yellow. Please find the anaglyph 3D glassess necessary to view this visualization attached at the back cover.

pore is narrowed from an approximately 4.0 Å times 5.0 Å opening to an approximately 3.3 Å times 3.5 Å opening (Fig. 3.17). The sensing of changes in substrate binding might occur via the “track-and-trace” loop, which runs mainly alongside the binding pocket and which could directly interact with the nicotine amide ring of NAD^+ through Thr-114. In particular, side chains of residues Val-115, Glu-117, Tyr-123 reaching into the binding pocket provide an alternating polar/apolar path and take part in the "ionic slide" (described in the next paragraph). Additional sensing might occur through Glu-237, which is adjacent to the pore-forming Ser-236. Its side chain reaches directly into the active side and interacts with residue His-296.

The electrostatic properties of the binding pocket were analyzed by calculating the side chain pK_a-values based on the 3D structure of *Bv*HSS and subsequently derived electrostatic potential maps at pH 5, 7, and 9 (visualized in Fig. 3.18). The calculation of the individual pK_a-values revealed particular noticeable shifts from standard pK_a-values towards more basic pK_a-values for acidic residues Glu-117, Glu-210, Asp-212, and Asp-361 near the binding pocket of of *Bv*HSS (PBD entry code 4PLP, see Table 3.6 for values and Fig. 3.19 for illustration of the pK_a-shifts of relevant residues). Slight basic shifts in pK_a-values were calculated for Asp-94, Glu-232, Glu-237, and Glu-298. The calculated pK_a-value for His-296 was shifted to a much

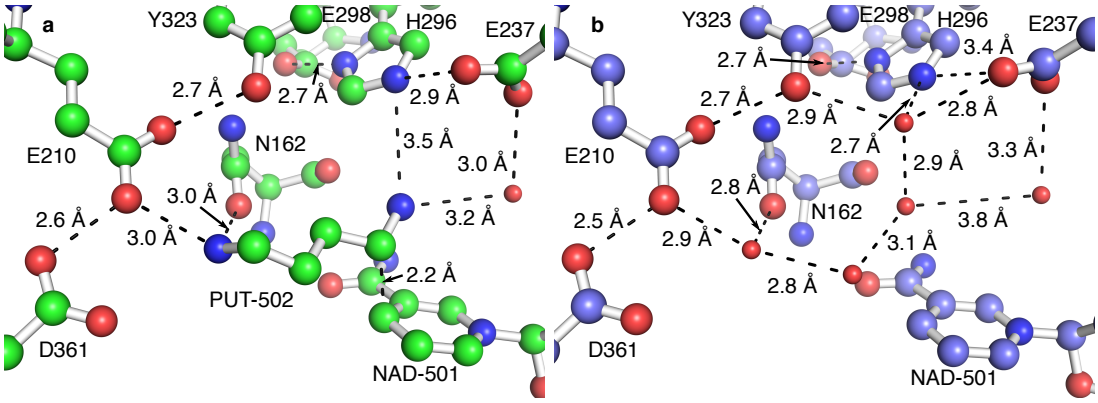

Figure 3.15: Residues of the active site of *Bv*HSS. Relevant residues, NAD-501, and PUT-502 are shown as ball-and-stick representations. Relevant water molecules are shown as spheres. All distances (indicated by dashed lines) were measured with the measurement function as implemented in the program PyMOL. (a) The active site of *Bv*HSS with bound PUT (PDB ID 4TVB, subunit B). (b) The active site of *Bv*HSS without substrate (PDB ID 4XQC, subunit B). The carbons in (a) and (b) are differently colored to avoid the impression of a stereoscopic. Trp-229 not shown for clarity. representation.

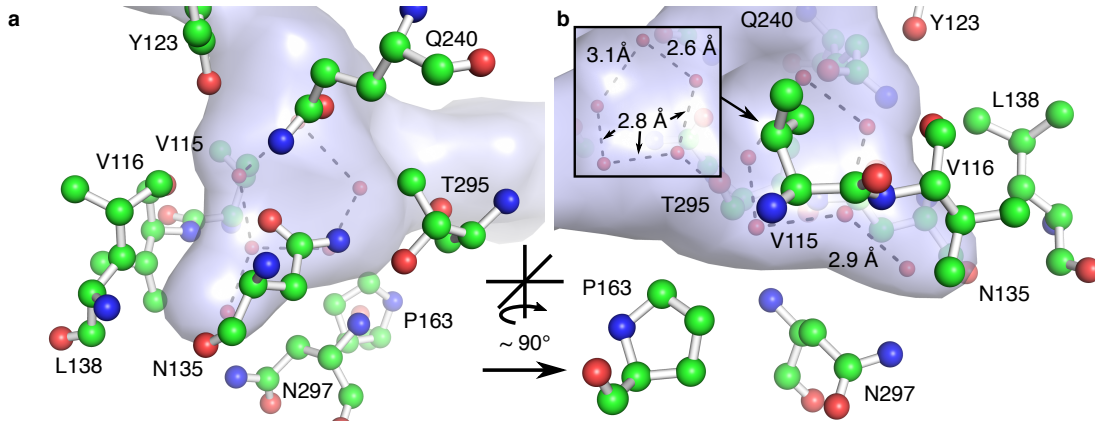

Figure 3.16: The side pocket at the “heel” of the binding pocket of *Bv*HSS, subunit B (PDB ID 4PLP). Relevant residues are shown as ball-and-stick representations. Relevant water molecules are shown as spheres. All distances (indicated by dashed lines) were measured with the measurement function as implemented in the program PyMOL. The binding pocket of *Bv*HSS is represented as a surface-rendered cavity in light blue. Both panels (a, b) show a detail of the same structure of *Bv*HSS from opposing points of view (as indicated by the rotation of approximately 90° around one axis).

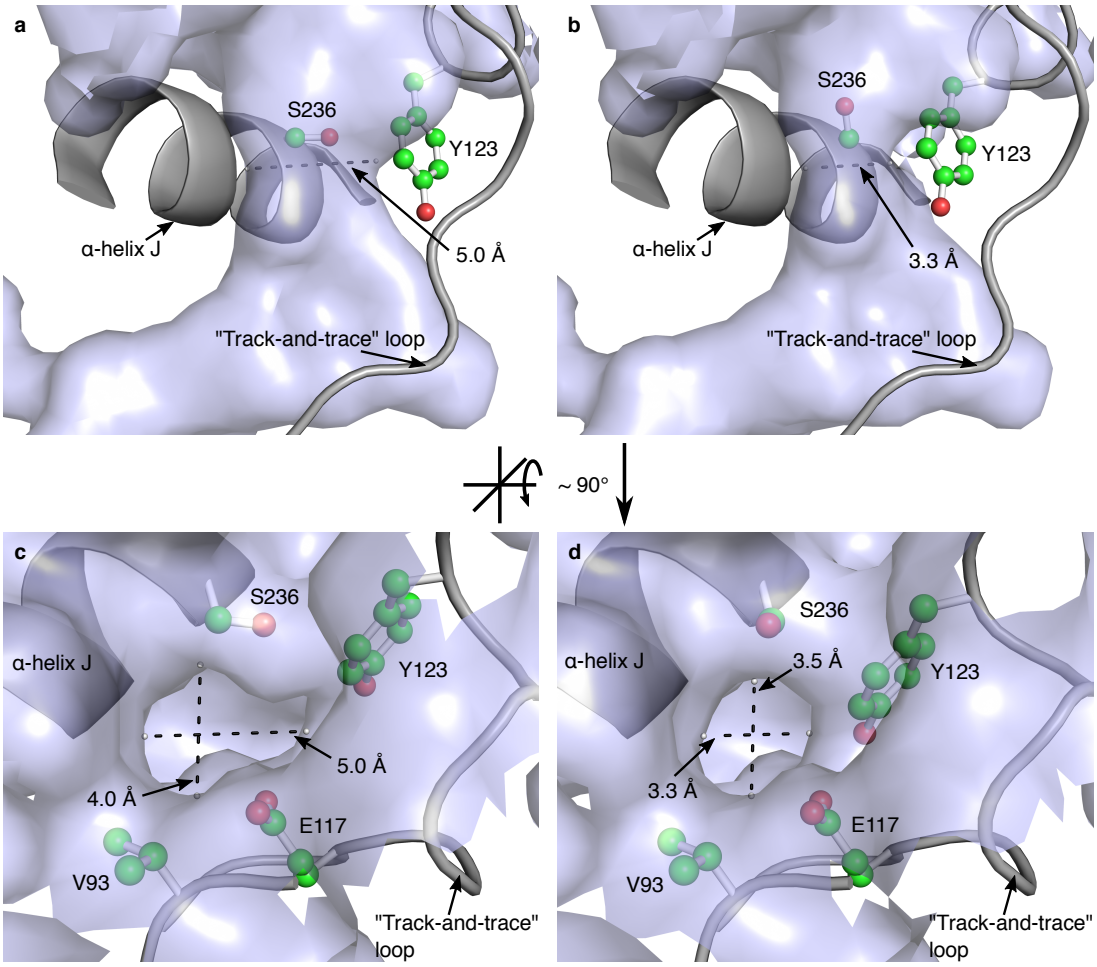

Figure 3.17: Dimensions of the pore at the entrance of the binding pocket. The binding pocket of *Bv*HSS variant H296S, subunit A (PDB ID 4XQE) is represented as a surface-rendered cavity in light blue. Pore-forming α-helix J and the "track-and-trace" loop are shown as cartoon representations. Pore-forming amino acids (Val-93, Glu-117, Tyr-123, and Ser-236) are given in ball-and-stick representations. The two observed alternate conformations A (a, c) and B (b, d) of residues Tyr-123 and Ser-236 effecting the dimension of the pore are shown separately. All given dimensions of the pore for both orientations and alternate conformations were measured in the same plane. All distance measurements were performed with the measurement function as implemented in the program PyMOL.

higher pK_a-value, together with those for Tyr-323 and Tyr-325. The resulting overall electrostatic potential of the surface of the pocket is mainly negative at pH 7 and pH 9, in contrast to a mainly positive potential at pH 5 (compare Fig. 3.18 b, c, e, and f with Fig. 3.18 a and d; residues Glu-232, Glu-298, Tyr-323, and Tyr 325 are not shown for clarity, for all residues see Fig. 3.14). At pH 7 (or pH 9), the negative electrostatic potential at the surface of the pocket increases from a region immediately above the entrance (Asp-94 and Glu-232) down to the active site between Glu-237, His-296, Trp-229, Tyr-323, and the nicotine amide ring of NAD^+. The entrance and active site are conjoined by a path along surface of areas of the binding pocket with highly negative electrostatic potential (mainly provided by Asp-94, Glu-117, and Glu-237 from entrance to active site) alternating with areas of less negative electrostatic potential or small areas of positive electrostatic potential mainly caused by Tyr-123. The residue His-296 with a calculated pK_a of 10 is most probably protonated and positively charged at both side chain nitrogens at pH 5, pH 7, and pH 9 causing the only positive electrostatic surface potential at pH 7 and pH 9 in the direct vicinity of the electron transfer site. The only additional positive electrostatic surface potential at pH 7 and pH 9 has been calculated at the narrow end of the binding pocket occupied by two waters. The reported catalytic pH optimum of pH 9 for HSS (Ober *et al.*, 1996) is in agreement with the calculated electrostatic potential of the surface of the binding pocket. PUT and HSP or other di- and tri-amines with a theoretical pK_a of 10 for their terminal amino groups will be mainly positively charged at pH 5 to pH 9. The binding pocket facilitates, but only under neutral to basic conditions, a mainly negative electrostatic surface potential and thus an attractive electrostatic effect on its substrates, thus explaining the observed pH-optimum of pH 8.7-9 for bacterial HSS (Ober *et al.*, 1996; Yamamoto *et al.*, 1993). The strongly negative electrostatic surface potential at the pore entrance might function as "bait" for the positively charged substrate, which then “slides down” the negative potential towards the active site. In particular, the side chain carboxy groups of Asp-94, Glu-117, and Glu-237 are positioned to provide negative ionic interaction sites at a distance of approximately 6.4 Å and 5.6 Å, with a small hydrophobic site (Val-93 or Val-115) in between each (Fig. 3.9 d and Fig. 3.18 a-c). With regard to the nitrogen-nitrogen distance of approximately 6.1 Å of linear PUT and the highly conserved residues Glu-117 and Glu-237 (Shaw *et al.*, 2010), this arrangement (“ionic slide”) might be involved in substrate discrimination and direction towards the active site. Because of its positive electrostatic potential, the side chain of Tyr-123 might additionally support substrate transfer by “pushing it down” by electrostatic repulsion.

3.6 Substrate-Binding Sites of *Bv*HSS

To determine substrate-binding sites, *Bv*HSS and the non-functional *Bv*HSS variants H296S and E237Q were co-crystallized or soaked with diamines of different lengths (DAP, PUT, and CAD) and with the polyamine agmatine (AGM) under various conditions as given in Table 3.1.

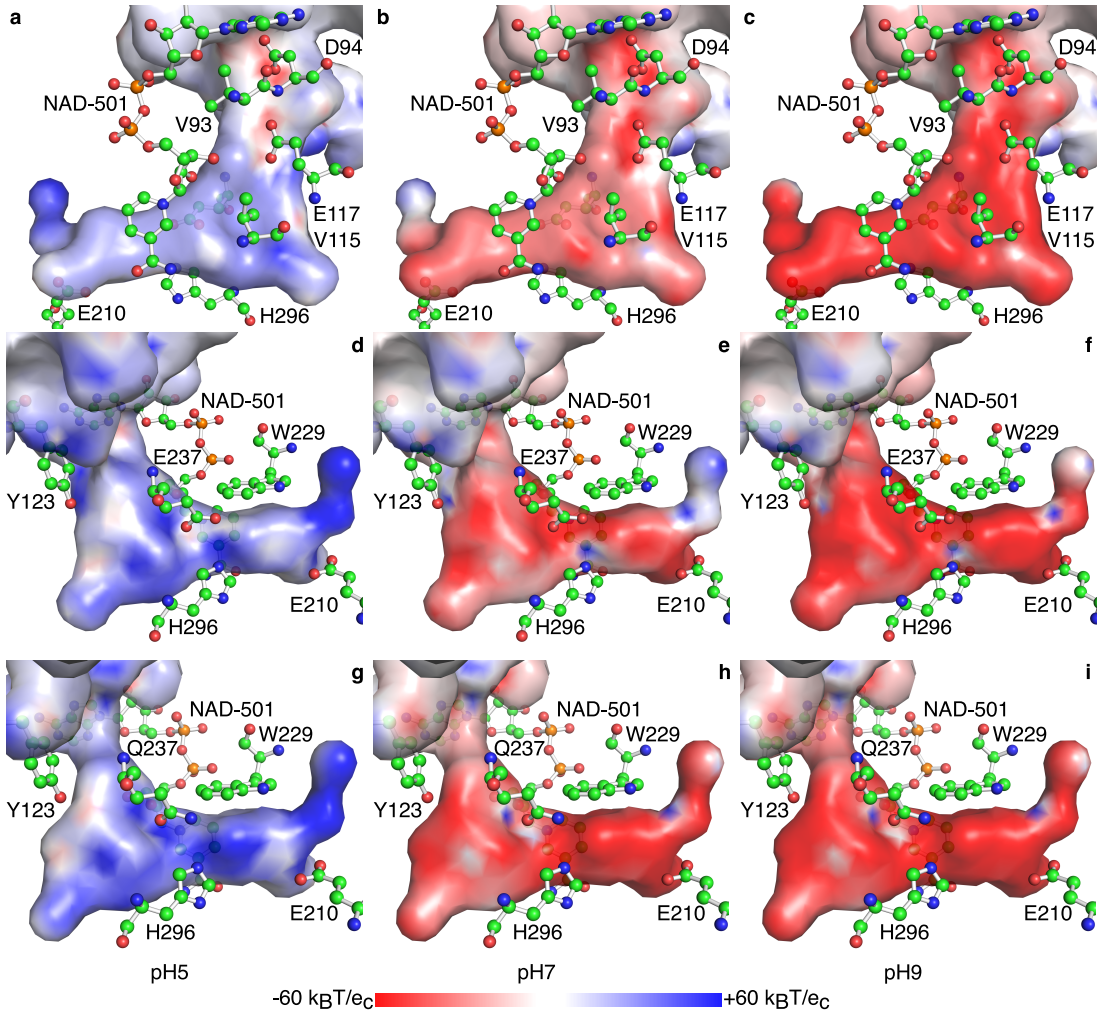

Figure 3.18: Representation of the electrostatic potential of the surface of the binding pocket at pH 5, 7, and 9. The electrostatic potential at the surface of the substrate-binding pocket (compare with Fig. 3.9 b and c) is represented as a color gradient from red (-60 k_BT/e_c) over white (0 k_BT/e_c) to blue (+60 k_BT/e_c) at pH 5 (a, d, g), pH 7 (b, e, h), and pH 9 (c, f, i) from two opposing orientations for *Bv*HSS wild-type (a-f, PDB ID 4PLP) and one orientation for *Bv*HSS variant E237Q (g-i, PDB ID 4XQG). The cofactor NAD^+ and the important residues Val-93, Asp-94, Val-115, Glu-117 ("ionic slide"), Tyr-123, Glu-210, Trp-229, Glu-237, and His-296 are superimposed in ball-and-stick representation. Residues Glu-232, Glu-298, Tyr-323, and Tyr 325 are not shown for clarity (for all residues see Fig. 3.14)

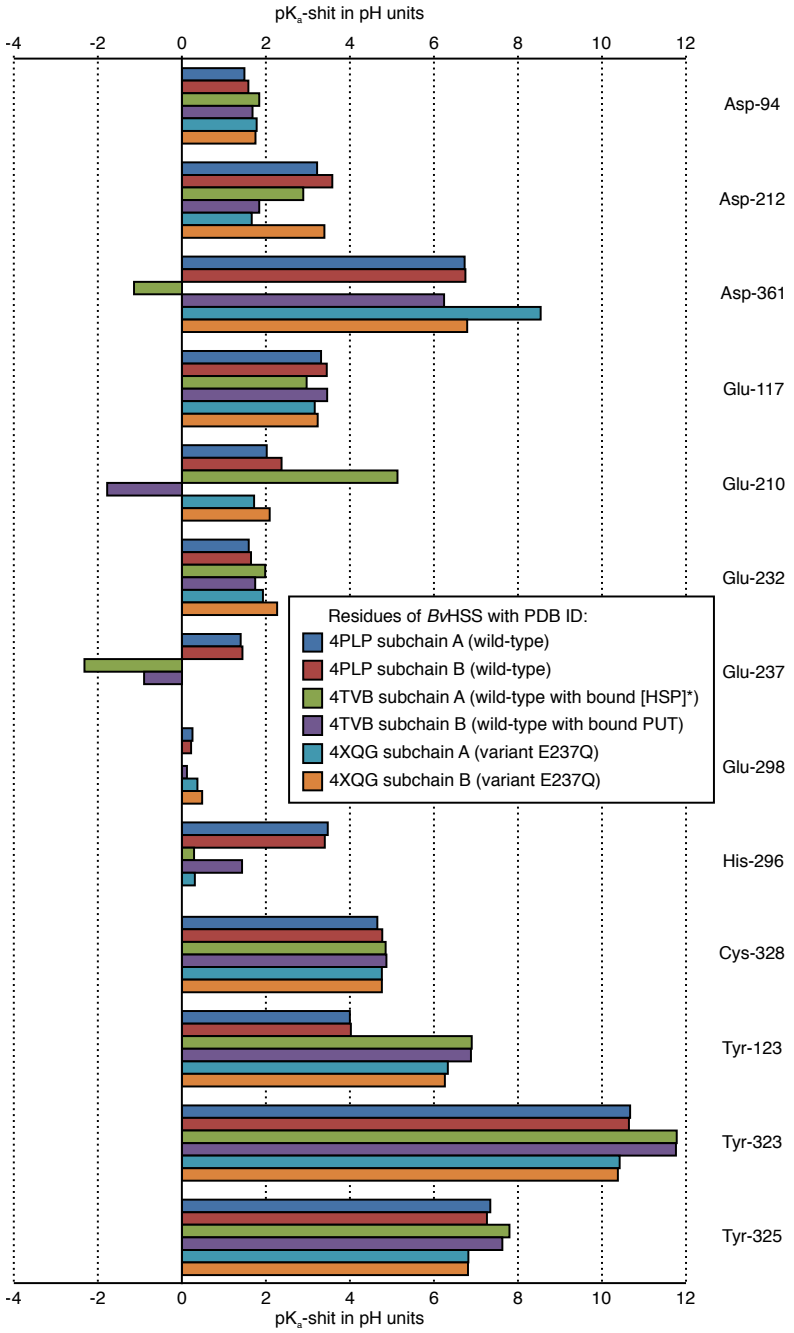

Figure 3.19: Graphical representation of the calculated pK$_a$-shifts of the titratable side chains of residues near the binding pocket of *Bv*HSS (PDB ID 4PLP and 4TVB) and *Bv*HSS variant E237Q (PDB ID 4XQG). The pK$_a$-shifts are the difference between the predicted pK$_a$-values (by the software PROPKA) and the model pK$_a$-values (model pK$_a$-values: Asp 3.8, Glu 4.5, His 6.5, Cys 9, Tyr 10). The values are given in Table 3.6.

Table 3.6: Relative pK_a-shifts of the titratable side chains of residues near the binding pocket of *Bv*HSS (PDB ID 4PLP and 4TVB) and *Bv*HSS variant E237Q (PDB ID 4XQG). The pK_a-shifts are the difference between the predicted pK_a-values (by the software PROPKA) and the model pK_a-values (model pK_a-values: Asp 3.8, Glu 4.5, His 6.5, Cys 9, Tyr 10). A graphical representation is given in Fig. 3.19.

Residue	*Bv*HSS subchain A PDB ID 4PLP	*Bv*HSS subchain B PDB ID 4PLP	*Bv*HSS subchain A PDB ID 4TVB	*Bv*HSS subchain B PDB ID 4TVB	*Bv*HSS E237Q subchain A PDB ID 4XQG	*Bv*HSS E237Q subchain B PDB ID 4XQG
Asp-94	1.5	1.6	1.8	1.7	1.8	1.8
Asp-212	3.2	3.6	2.9	1.8	1.7	3.4
Asp-361	6.7	6.8	-1.1	6.2	8.5	6.8
Glu-117	3.3	3.5	3.0	3.5	3.2	3.2
Glu-210	2.0	2.4	5.1	-1.8	1.7	2.1
Glu-232	1.5	1.5	1.8	1.6	1.8	2.1
Glu-237	1.4	1.4	-2.3	-0.9	0.0	0.0
Glu-298	0.3	0.2	0.0	0.1	0.4	0.5
His-296	3.5	3.4	0.3	1.4	0.3	-0.1
Cys-328	4.7	4.8	4.9	4.9	4.8	4.8
Tyr-123	4.0	4.0	6.9	6.9	6.3	6.3
Tyr-323	10.7	10.6	11.8	11.8	10.4	10.4
Tyr-325	7.3	7.3	7.8	7.6	6.8	6.8

3.6.1 Verification of Polyamine Content of *Bv*HSS Crystals by HPLC Analysis

The type of polyamine present within the individual crystals was verified by HPLC analysis. The analyses of a *Bv*HSS crystal cluster co-crystallized with DAP and PUT (sample A) and of a *Bv*HSS crystal cluster (sample B) and a single *Bv*HSS crystal (sample C), both co-crystallized with DAP and soaked with PUT, clearly detected DAP and PUT plus SPD in all samples. The height and area of the DAP peaks detected in samples B and C were lower than that of the PUT peak, in contrast to an approximately equal height and area detected in sample A (chromatograms shown in Fig. 3.20 and Fig. 3.21). This indicates an effective reduction of compounds present in the crystallization solution by the crystal transfer and polyamine derivatization procedure and thereby emphasizes the polyamine composition inside the *Bv*HSS crystals. All analyzed crystals gave a peak with the same retention time of HSP; this peak was overlaid by a peak of an unknown impurity or side product of the labeling procedure. The peak height and area of this impurity detected during calibration runs without HSP was lower than the peak detected during the analysis of the *Bv*HSS sample A and was approximately of the same or slightly higher magnitude as that during the analysis of sample C (Fig. 3.20 a vs. d and 3.21 a vs. b, d). The presence of SPD (known *Bv*HSS product of DAP and PUT (Ober *et al.*, 1996)) in all samples and the most probable presence of HSP in sample A, together with the effective reduction of mother liquor compounds, strongly indicate that *Bv*HSS is active under these crystallization conditions.

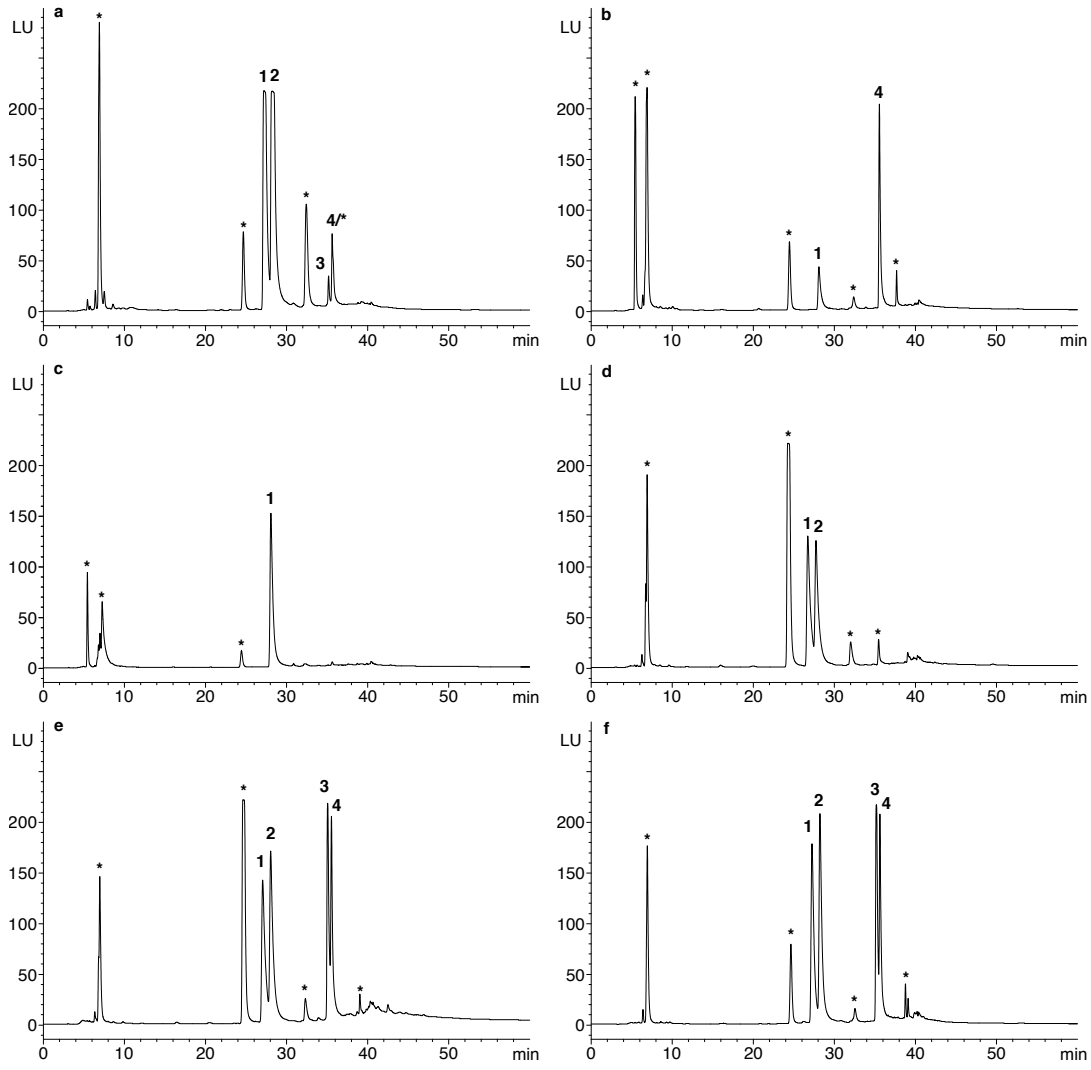

Figure 3.20: Results of HPLC-based polyamine analyses of *Bv*HSS crystals, qualitative enzyme activity assays, and various calibration mixtures. The chromatograms show the measured fluorescence intensity in light units (LU) (detector-settings: λ_{Ex} = 248 nm; λ_{Em} = 398 nm; photomultiplier tube gain 11; response time 4 s (standard); lamp flash frequency 296 Hz (standard)) over the complete analysis run time of 60 min. (a) Analysis of the polyamine content of a *Bv*HSS crystal cluster from co-crystallization with DAP and PUT (sample A). (b) Analysis of polyamine content after incubation of *Bv*HSS with PUT in standard buffer supplemented with 2 mM NAD^+ for 1 h at 37 °C. (c) Analysis of polyamine content after incubation of non-functional *Bv*HSS variant H296S with PUT in standard buffer supplemented with 2 mM NAD^+ for 1 h at 37 °C. (d) Chromatogram of calibration mixture I, containing DAP and PUT each with approximately 800 pmol. (e, f) Chromatograms of two independent separations of calibration mixtures II, containing DAP, PUT, SPD, and HSP, each with approximately 800 pmol. Polyamines identified via retention times: 1 = DAP, 2 = PUT, 3 = SPD, 4 = HSP. Impurities that were not further analyzed or byproducts of sample derivatization are marked with an asterisk (*).

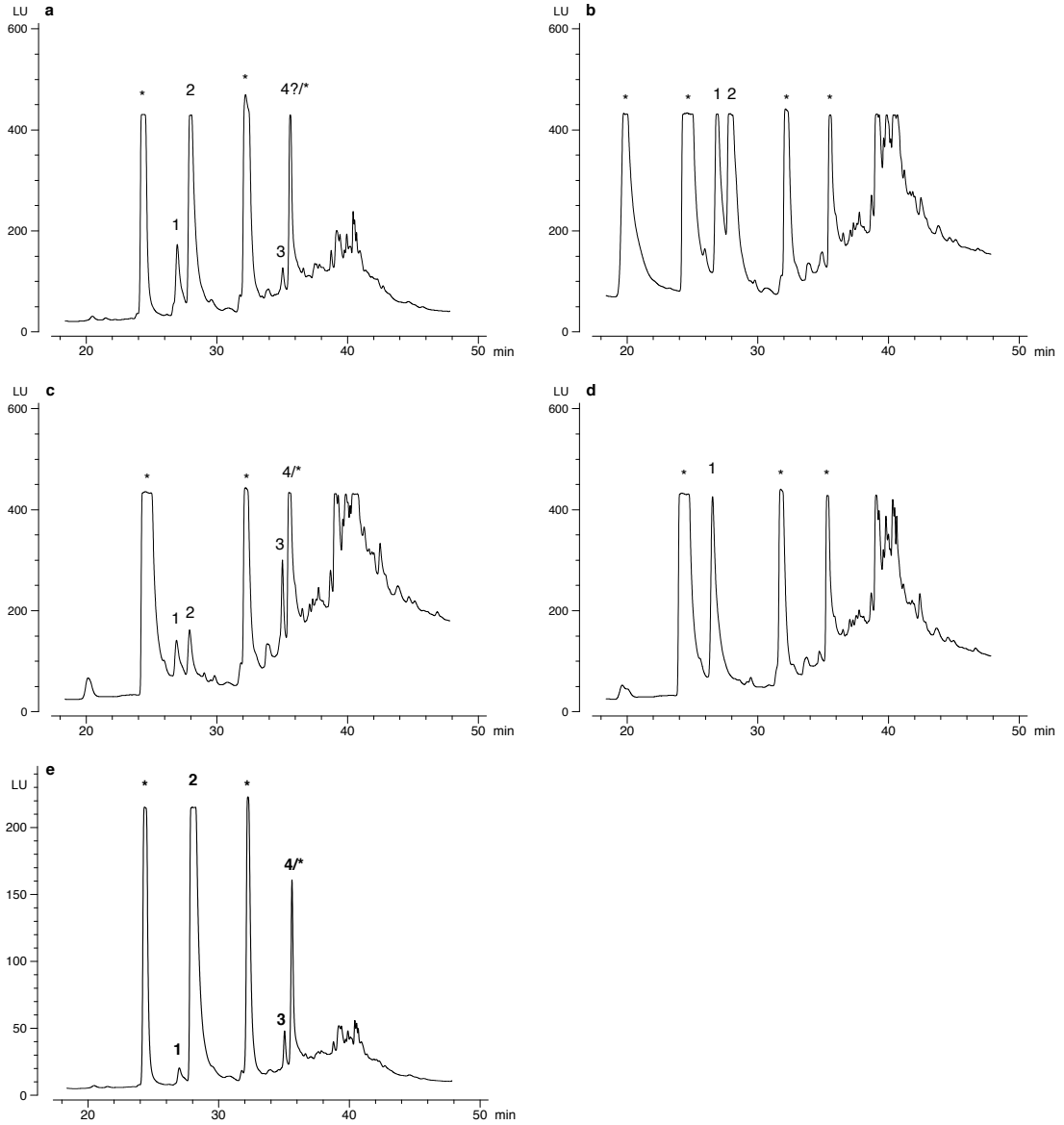

Figure 3.21: Results of HPLC-based polyamine analyses of *Bv*HSS crystals and various calibration mixtures. The chromatograms show the measured fluorescence intensity in light units (LU) (detector-settings: λ_{Ex} = 248 nm; λ_{Em} = 398 nm; photomultiplier tube gain 16 (a-d) or 14 (e); response time 4 s (standard); lamp flash frequency 296 Hz (standard)) as a section of the complete analysis run time of 60 min. (a) Analysis of the polyamine content of a single *Bv*HSS crystal from co-crystallization with DAP and subsequent soaking with PUT (sample C). (b) Chromatogram of calibration mixture I, containing DAP and PUT, each with approximately 8 pmol. (c) Chromatogram of calibration mixtures II, containing DAP, PUT, SPD, and HSP, each with approximately 0.8 pmol. (d) Chromatogram of calibration mixture III, containing PUT with approximately 8 pmol. (e) Analysis of the polyamine content of a *Bv*HSS crystal cluster from co-crystallization with DAP and subsequent soaking with PUT (sample B). Polyamines identified via retention times: 1 = DAP, 2 = PUT, 3 = SPD, 4 = HSP. Impurities that were not further analyzed or byproducts of sample derivatization are marked with an asterisk (*).

3.6.2 *Bv*HSS with Bound Transition-close States of the Catalyzed Reaction

Supported by the results from the HPLC analyses, the electron density derived from a *Bv*HSS crystal co-crystallized with DAP and subsequently soaked for 5 min with PUT was interpreted to contain "transition-close" states of the catalyzed reaction (PDB ID 4TVB, Fig. 3.22 and Fig. 3.23, Fig. 3.24 a and b). The electron density at the active site of subunit B is interpreted as a hydride transfer from PUT C4 to NAD^+ C4N representing a "transition-close" state of the oxidation at carbon C4. The electron density at the active site of subunit A is interpreted as representing the hydride transfer from C4N of NADH to the still oxidized C05 of HSP, with a partial double bond between C05 and N06 of HSP representing a partial Schiff base (see subsection "Hypothesis of the Reaction Steps of HSS Catalysis" on page 61 for details). The inner most amino group at nitrogen N01 of HSP or nitrogen N1 of PUT is coordinated to residues Glu-210 and Asn-162 (inner amino site), whereas the amino group at nitrogen N11 of HSP is coordinated to Glu-237 and oxygen O2D of NADH (outer amino site). The nitrogen N2 of PUT is coordinated to Asn-162 (center amino site). If in its protonated state, the nitrogen N2 of PUT or nitrogen N06 of HSP can additionally be coordinated to Trp-229 via cation-π interaction (Fig. 3.25 a and c; for Trp-229 position relative to NAD^+ refer to Fig. 3.32 b and Fig. 3.33 b and d or Fig. 3.14) (Ma and Dougherty, 1997; Marshall *et al.*, 2009). In both observed cases (in subunit A and B of *Bv*HSS with PDB ID 4TVB), the polyamine nitrogens (N2 of PUT, N06 of HSP) are bound with a non-optimal off-center geometry relative to the center of the 6-membered (benzene) ring of the respective Trp-229 side chain. Based on calculated interaction energies of benzene with NH_4^+ (Marshall *et al.*, 2009), these positions (R = 4.2 Å, θ= 24.7°, and φ = 11.3° for nitrogen N2 of PUT; R = 3.5 Å, θ = 15.9°, and φ = 41.3° for nitrogen N06 of HSP, Fig. 3.25 a and c) will most likely result in interaction energies significantly contributing to substrate binding and recognition. The substrates are further stabilized by hydrophobic interactions with Val-115, Pro-163, Trp-229, His-296, Tyr-323, Tyr-325, and Leu-363 (Fig. 3.22 and Fig. 3.23). The binding site between the inner amino site and center amino site will be referred to as the inner (binding) site, whereas the binding position between the outer amino site and center amino site will be referred to as the outer (binding) site (Fig. 3.9).

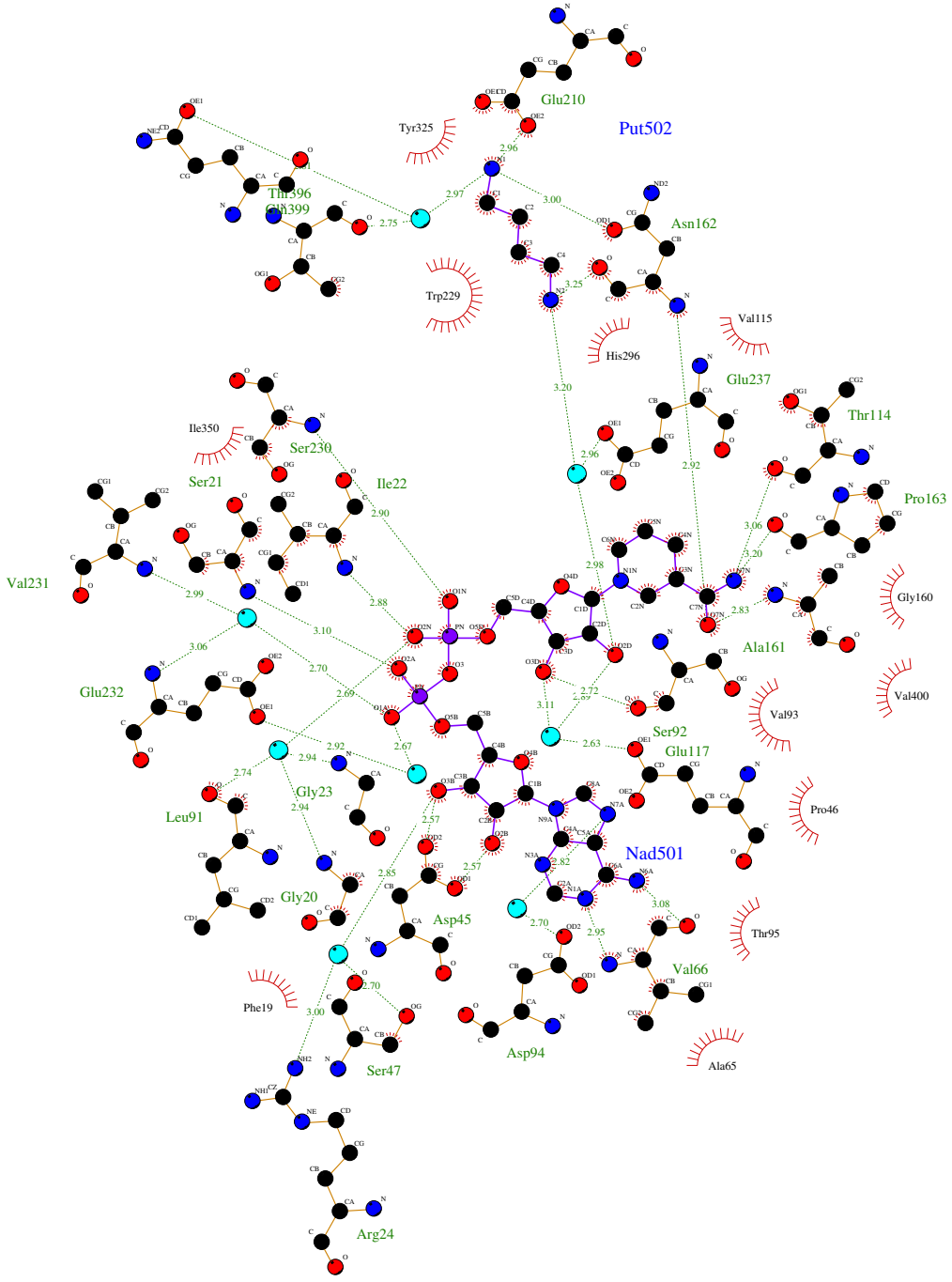

Figure 3.22: Interactions between *Bv*HSS and the ligand PUT. Shown are 2D circle-and-line representations of NAD^+ and the ligand PUT found at the active site together with relevant amino acids of *Bv*HSS. The hydrophobic interactions (red spoked arcs) and the hydrogen bonds (green dashed lines with distances in Å) between the amino acids of *Bv*HSS, NAD^+, and PUT (Put502) are shown based on the structures with PDB ID 4TVB subunit B. The atoms presented as circles are color coded: carbon = black, oxygen = red, nitrogen = blue, phosphor = purple. The bonds between ligand atoms are colored in purple and between amino acids colored in orange. Water molecules are represented as cyan colored circles. Image was generated with LigPlot+.

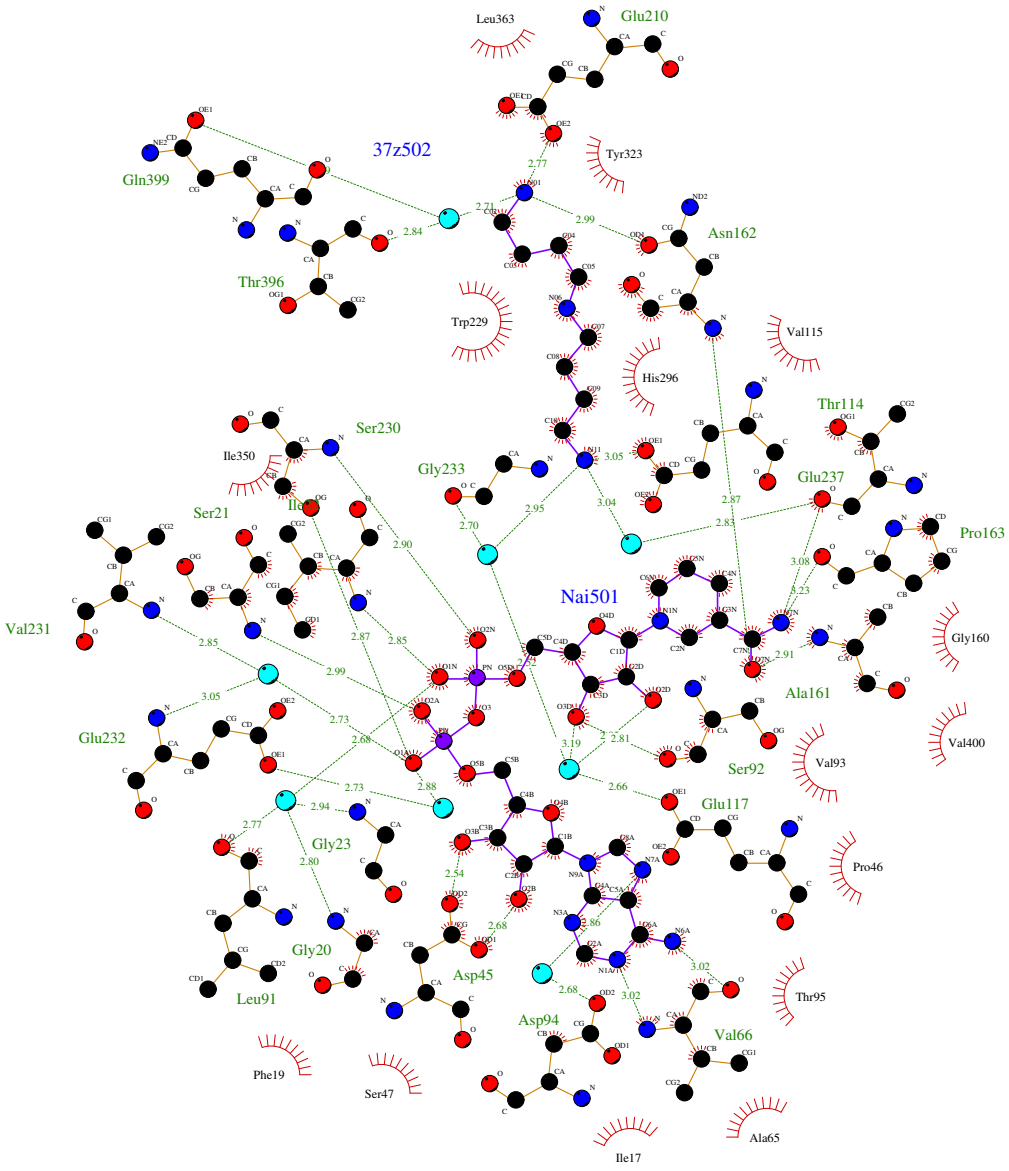

Figure 3.23: Interactions between *Bv*HSS and the ligand HSP. Shown are 2D circle-and-line representations of NAD(H) and the ligand HSP found at the active site together with relevant amino acids of *Bv*HSS. The hydrophobic interactions (red spoked arcs) and the hydrogen bonds (green dashed lines with distances in Å) between the amino acids of *Bv*HSS, NAD(H) (Nai501), and HSP (37z502) are shown based on the structures with PDB ID 4TVB subunit A. The atoms presented as circles are color coded: carbon = black, oxygen = red, nitrogen = blue, phosphor = purple. The bonds between ligand atoms are colored in purple and between amino acids colored in orange. Water molecules are represented as cyan colored circles. Image was generated with LigPlot+.

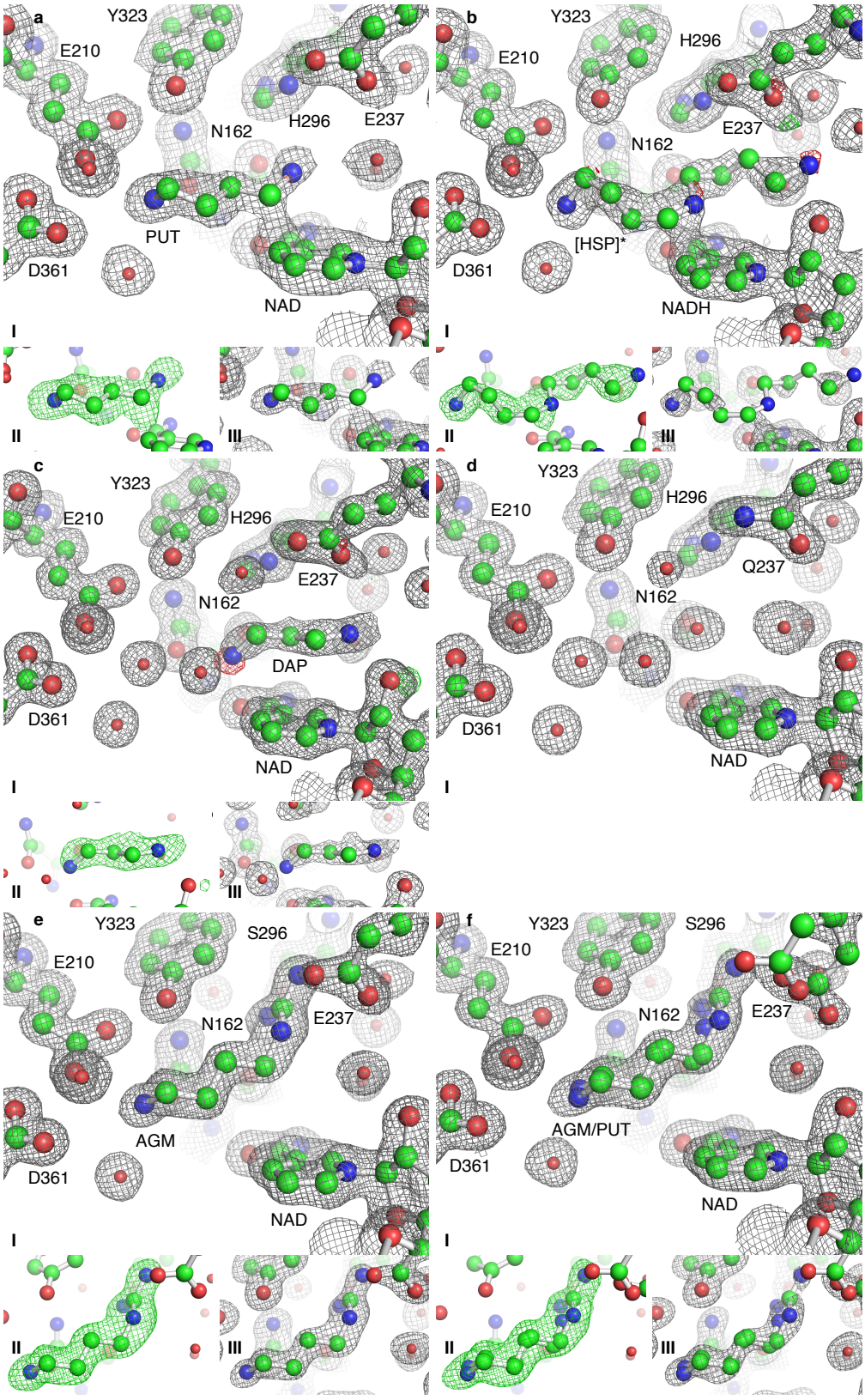

Figure 3.24: Active site of *Bv*HSS and *Bv*HSS variants E237Q and H296S with bound polyamines. The electron density maps are shown as a mesh at a contour level of 1σ (2mFo-DFc in gray) and +/- 5σ (mFo-DFc, green/red). Electron density maps obtained from PHENIX.refine are shown in (I), and the simulated annealing (SA) ligand omit electron density (ED) maps obtained from PHENIX.composite_omit_map are shown in (II, mFo-DFc) and (III, 2mFo-DFc). Relevant residues are shown as ball-and-stick representations. (a,b) Active site of *Bv*HSS (PDB ID 4TVB) with bound substrates in subunit A and subunit B. The PUT bound in subunit B is shown in (a). The transition close state of the reduction to HSP bound in subunit A is shown in (b). (c) Active site of *Bv*HSS with bound DAP (subunit A, PDB ID 4XQC). (d) Active site of *Bv*HSS variant E237Q (subunit B, no SA ligand omit ED maps were calculated because of the lack of bound substrate, PDB ID 4XQG). (e, f) Active site of *Bv*HSS variant H296S with bound AGM (e, PDB ID 4XQE, subunit B) or with bound AGM and PUT as alternate conformations (f, PDB ID 4XRG, subunit B). The adjustment of the occupancy values for AGM and PUT (with a constrained occupancy group per molecule to ensure equal occupancy for each atom of the respective molecule) was performed by PHENIX.refine during refinement. The calculated occupancy is in subunit A 0.56 for AGM and 0.44 for PUT and in subunit B 0.66 for AGM and 0.34 for PUT.

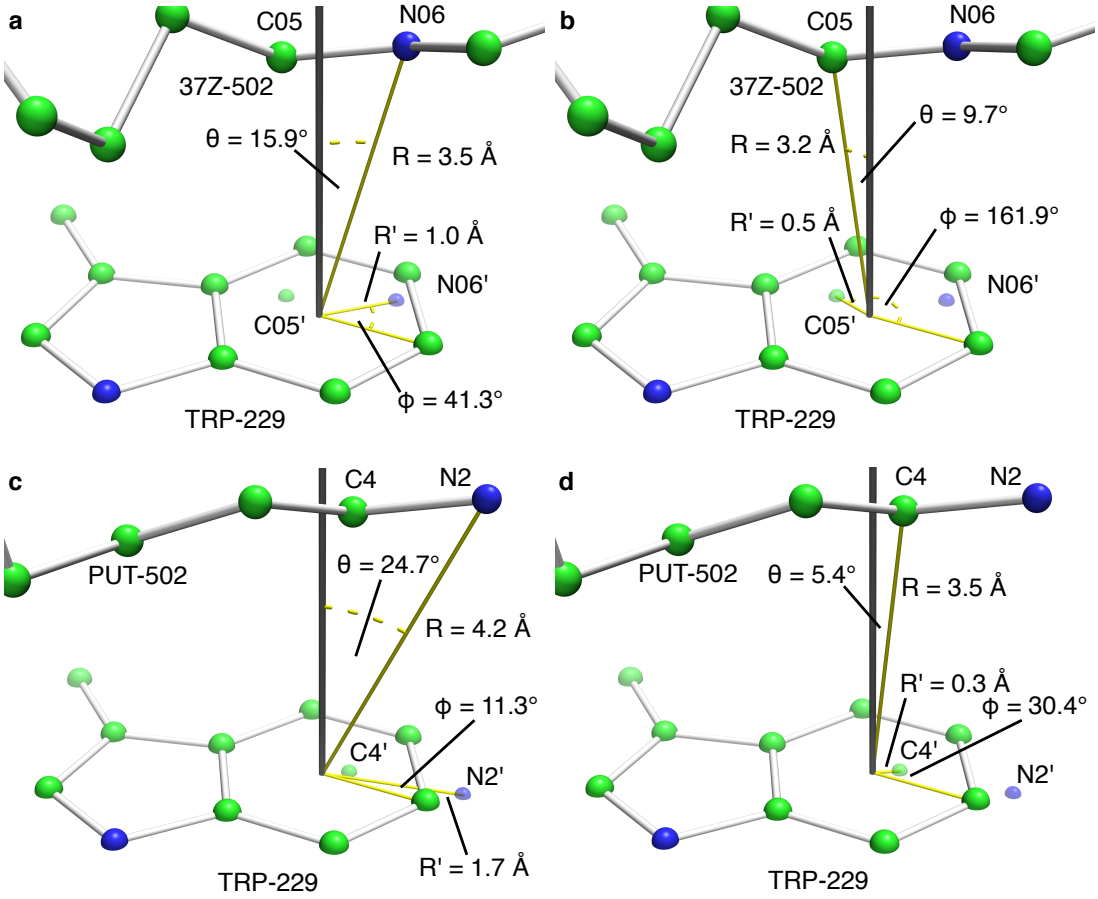

Figure 3.25: Tryptophan Trp-229 cation-π interaction angles and distances. The *Bv*HSS (PDB ID 4TVB) subunit A Trp-229 and 37Z(HSP)-502 (a, b) and subunit B Trp-229 and PUT-502 (c, d) are shown in ball-and-stick representations. The plane of the indol of the Trp-229 side chain is indicated by a white surface cutting all spheres in half representing atoms lying on the aromatic plane. The black line represents the orthogonal vector to the aromatic plane with its origin at the center of the 6-membered (benzene) ring of the tryptophan side chain. The orthogonal projections of carbon C05 and nitrogen N06 of 37Z-502 (a, b) and of carbon C4 and nitrogen N2 of PUT-502 (c, d) are indicated as slightly smaller spheres named C05', N06', C4', and N2'. All angle and distance measurements were performed with the measurement function implemented in the program PyMOL. The names of the angles and distances were chosen by analogy to Marshall *et al.* (2009)

A PUT or HSP bound at the afore described positions lead to changes of the pK_a-values of the titratable groups of some of the residues near the active site (see Table 3.6 and Fig. 3.19). The pK_a-shift of Glu-237 inverts from a basic to an acidic shift, the pK_a of His-296 converges to the model pK_a and the pK_a of Tyr-123 is shifted to an even more basic value. Of note, an HSP bound at the active site leads to an even higher basic shift of the pK_a of Glu-210 and an inversion of the pK_a-shift of Asp-361 to an acidic shift. In contrast, a PUT bound at the active site causes an inversion of the pK_a-shift of Glu-210 to an acidic shift and no changes in the pK_a of Asp-361. In conjuction, these changes might reflect in part the substrate binding and recognition mechanisms of *Bv*HSS: The decreased pK_a of Glu-210 could indicate a stronger binding of

PUT at the inner binding site. The increased pK_a of Glu-210 together with the decreased pK_a of Glu-237 might indicate at weaker HSP binding or even an "extraction-mechanism" of the HSP from the active site.

3.6.3 *Bv*HSS with Bound DAP at the Active Site and at the Ionic Slide

The electron density obtained from a *Bv*HSS crystal co-crystallized with DAP and PUT (PDB ID 4XQC) did not allow an interpretation of *Bv*HSS with bound PUT or HSP, but rather with bound DAP at positions distinct from that of PUT in the *Bv*HSS structure obtained from crystals after soaking with PUT (PDB ID 4TVB, compare Fig. 3.26 with 3.22 and Fig. 3.24 c with a). Two DAP molecules were found at two different positions in subunit A (PDB ID 4XQC), of which the first was found at the active site (Fig. 3.26 and Fig. 3.24 c) and the second near the pore forming α-helix J in the entrance of the binding pocket (Fig. 3.27). The innermost nitrogen ND of the DAP at the active site is coordinated to Asn-162 and oxygen O7N of NAD^+, whereas nitrogen NAA is coordinated to Glu-237 and oxygen O2D of NAD^+. Neither nitrogen position exactly matches those of HSP or PUT. With the nitrogen NAA position being found near the inner amino site and the nitrogen ND position being found near the center amino site (shifted towards the inner amino site), the overall geometry of DAP has to be slightly “stretched” to fit the observed electron density. The innermost nitrogen ND of the second DAP is coordinated to Glu-117 and oxygen O2D of NAD^+, whereas nitrogen NAA is coordinated to Ser-236 and oxygen O of Glu-232 (Fig. 3.27). Thus, the nitrogen ND is positioned at the proposed ionic interaction site 2 of the "ionic slide" (refer to Fig. 3.9 d). The other nitrogen is positioned slightly "below" the proposed ionic interaction site 1. In case of a, one carbon atom longer, PUT instead of a DAP, the corresponding nitrogen would still be positioned slightly below the ionic interaction site 1. This supports the proposed function of the ionic slide as being a substrate guiding mechanism: The observed electron density of this second DAP (Fig. 3.27 b) appears well defined and is not “smeared” as in the case of the first DAP. Thus, the modeled position is most likely homogeneously occupied throughout the most molecules of the crystal. This positioning can be explained by a higher attractive force for a positively charged nitrogen of the ionic interaction site 2 over site 1, resulting in a substrate guiding towards the active site of *Bv*HSS.

3.6.4 CAD and AGM were not Found at the Active Site of *Bv*HSS

It was not possible to determine a distinct binding site of CAD. The electron density obtained from a *Bv*HSS crystal co-crystallized with CAD was not interpretable with bound CAD at the active site. All *Bv*HSS and *Bv*HSS variants co-crystallized with AGM were found to have AGM bound to the protein surface at various sites, most likely causing the observed improvement in crystal growth.

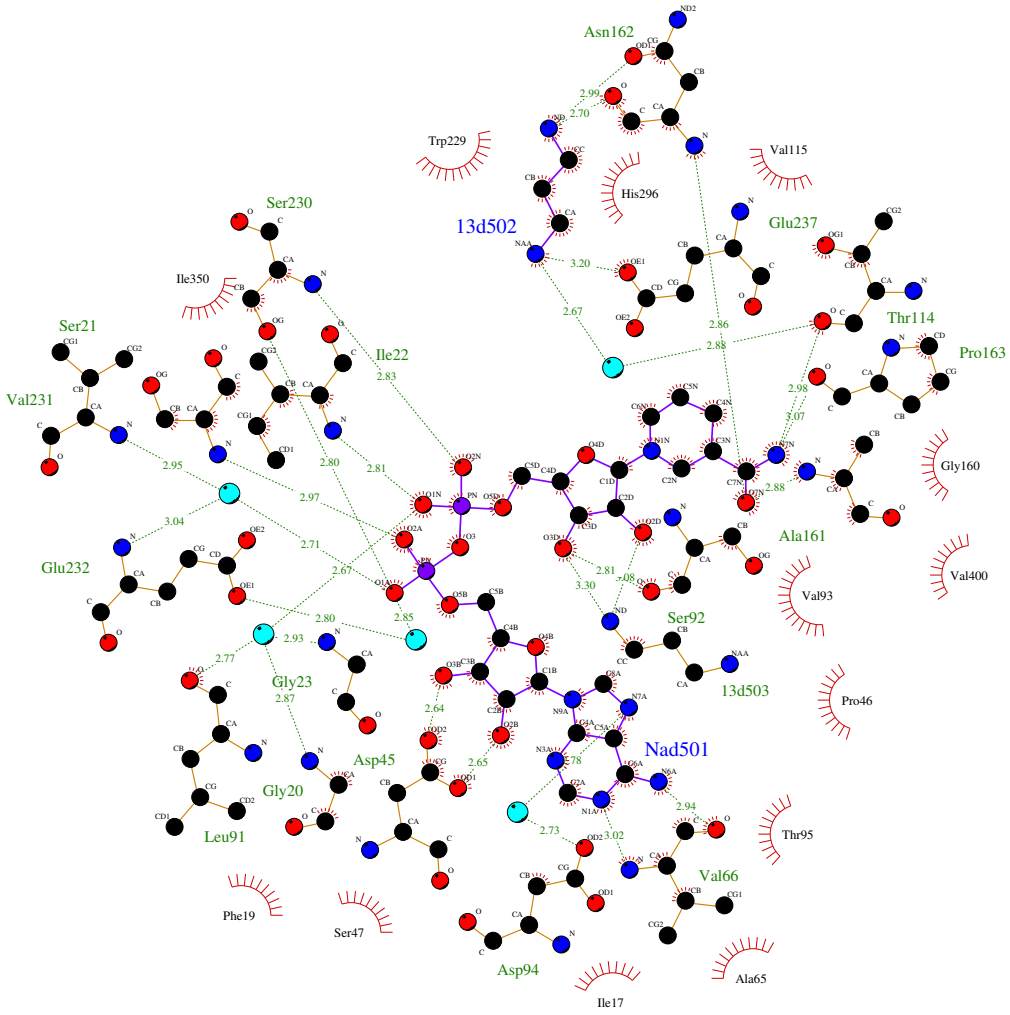

Figure 3.26: Interactions between *Bv*HSS and the ligand DAP. Shown are 2D circle-and-line representations of NAD^+ and the ligand DAP found at the active site together with relevant amino acids of *Bv*HSS. The hydrophobic interactions (red spoked arcs) and the hydrogen bonds (green dashed lines with distances in Å) between the amino acids of *Bv*HSS, NAD^+, and DAP (13d502) are shown based on the structures with PDB ID 4XQC with bound DAP. The atoms presented as circles are color coded: carbon = black, oxygen = red, nitrogen = blue, phosphor = purple. The bonds between ligand atoms are colored in purple and between amino acids colored in orange. Water molecules are represented as cyan colored circles. Image was generated with LigPlot+.

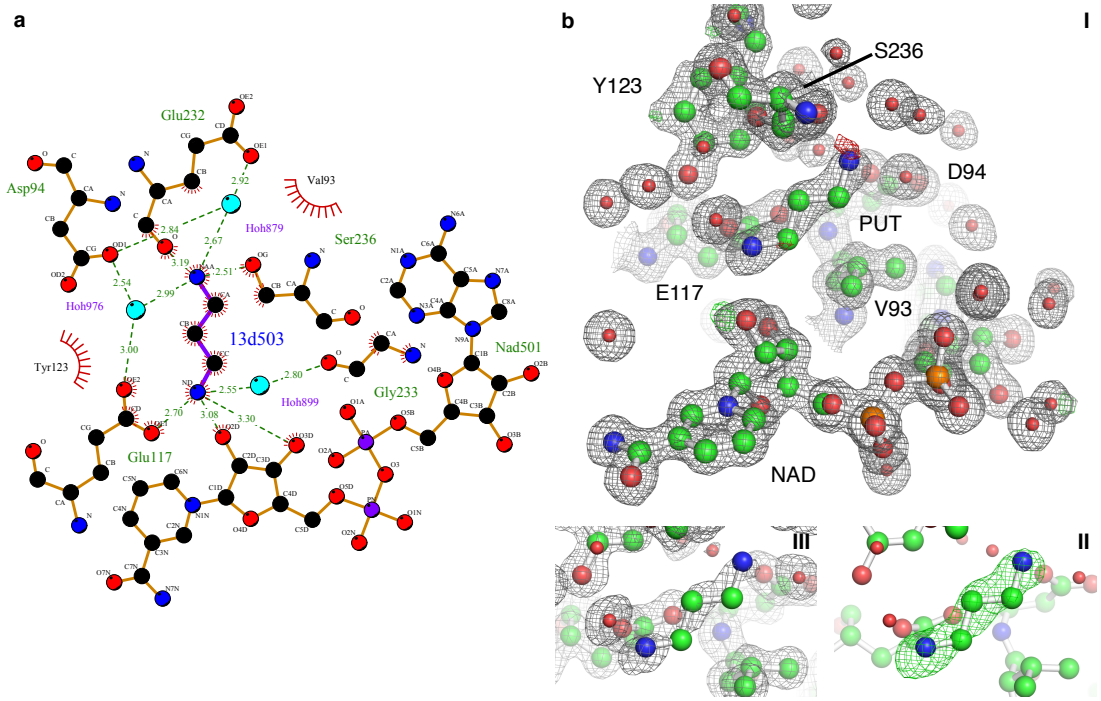

Figure 3.27: DAP bound at the "ionic slide" of *Bv*HSS (PDB ID 4XQC). (a) The hydrophobic interactions (red spoked arcs) and hydrogen bonds (green dashed lines with distances in Å) between the residues of *Bv*HSS (some of which take part in forming the "ionic slide"), NAD^+, and DAP (13d503) are shown as 2D circle-and-line representations. The atoms presented as circles are color coded: carbon = black, oxygen = red, nitrogen = blue, phosphor = purple. The bonds between ligand atoms are colored in purple and between amino acids and NAD^+ colored in orange. Water molecules are represented as cyan colored circles. Images were generated with LigPlot+. (b) The electron density map of relevant residues, NAD^+, and PUT are shown as a mesh at a contour level of 1σ (2mFo-DFc in gray) and +/- 5σ (mFo-DFc, green/red). Electron density maps obtained from PHENIX.refine are shown in (I), and the simulated annealing (SA) ligand omit electron density (ED) maps obtained from PHENIX.composite_omit_map are shown in (II, mFo-DFc) and (III, 2mFo-DFc). Relevant residues are shown as ball-and-stick representations.

3.6.5 Modified Substrate-Binding at the Active Site of *Bv*HSS Variants

Structures derived from the enzymatically inactive *Bv*HSS variant H296S (PDB # 4XQE and 4XRG) revealed slightly different substrate positions, and other than Glu-298 and Glu-237, no differences for any amino acid positions or orientations in the active site. In contrast to wild-type *Bv*HSS, the variant H296S co-crystallized with AGM was found to bind AGM in the active site with its guanidine group approximately placed at the former His-296 imidazole ring position (Fig. 3.24 e). The primary amino group of AGM was bound and coordinated as that of HSP or PUT at the inner amino site. The electron density of *Bv*HSS variant H296S crystals co-crystallized with AGM and, when subsequently soaked for 5 min with PUT, showed a decrease in electron density for the guanidine group of the AGM bound at the active site. PUT most likely competes with AGM for the binding at the observed position. Therefore, the electron density is interpreted as reflecting alternate locations of AGM and PUT (Fig. 3.28, Fig. 3.29 and Fig. 3.24 f). Compared with PUT bound in wild-type *Bv*HSS (PDB ID 4TVB), the first nitrogen of PUT is bound at the same inner amino site. The second nitrogen and the carbon that is thought to be oxidized occur farther away from the nicotine amide ring of NAD^+ (approximately 2 Å and 1.5 Å, respectively, measured from the carbon C4N of NAD^+ at which the hydride transfer occurs).
Enzymatically inactive *Bv*HSS variant E237Q co-crystallized with AGM and PUT gave a structure with no bound substrate (PDB ID 4XQG, Fig. 3.24 d). Other than minimal and most likely negligible rotations of the side chain amide group of amino acid Gln-237 and the side chain of amino acid His-296, no structural changes of active site residues compared with wild-type *Bv*HSS were observed. In contrast to the structure of the wild-type *Bv*HSS with no bound substrate (PDB ID 4PLP), the Tyr-123 was clearly represented by electron density in its narrow position. The exchange of residue Glu-237 by Gln-237 resulted in changes of the electrostatic potential of the surface of the binding pocket (Fig. 3.18 g-i). Compared with wild-type *Bv*HSS, the side chain of His-296 ($pK_{a,calc}$ = 6.4, see also Tab. 3.6 and Fig. 3.19) was no longer protonated at both nitrogens resulting in a loss of the positive charge at the imidazole ring. Together with the loss of the negative charge of the side chain of residue 237 because of the replacement of glutamate by glutamine, the electrostatic potential of the surface of the pocket inverted at pH 7 and pH 9, at a region around Gln-237, to a now positive electrostatic potential and, at an area around His-296, to a negative electrostatic potential.

3.7 Structures of Wild-type *Bv*HSS and *Bv*HSS Variants Provide Functional Insights

The structures of active wild-type *Bv*HSS and inactive *Bv*HSS variants reveal important amino acid residues for enzyme function and substrate binding. The side chain of His-296 seems to be crucial for correct substrate positioning. Of note, the structure of *Bv*HSS variant E237Q does not have PUT bound at the active site implying an important role for the residue Glu-237 during substrate binding. Contrary to expectations, the variation of Glu-237 prevents the

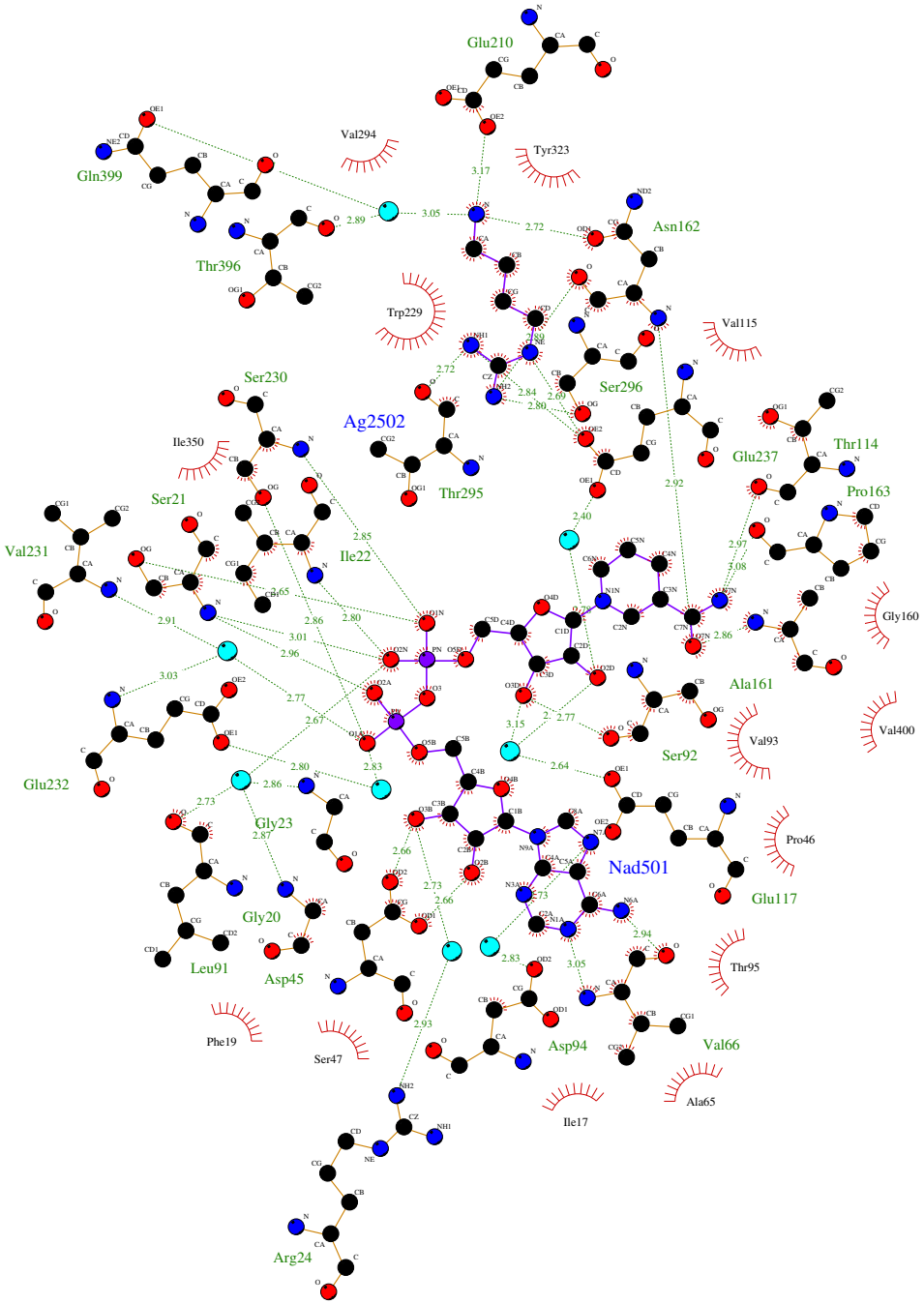

Figure 3.28: Interactions between *Bv*HSS and the ligand AGM. Shown are 2D circle-and-line representations of NAD^+ and the ligand AGM found at the active site together with relevant amino acids of *Bv*HSS variant H296S. The hydrophobic interactions (red spoked arcs) and the hydrogen bonds (green dashed lines with distances in Å) between the amino acids of *Bv*HSS, NAD^+, and AGM (Ag2502) are shown based on the structures with PDB ID 4XRG with bound AGM (the PUT that alternativly occupies the same position is shown in Fig. 3.29). The atoms presented as circles are color coded: carbon = black, oxygen = red, nitrogen = blue, phosphor = purple. The bonds between ligand atoms are colored in purple and between amino acids colored in orange. Water molecules are represented as cyan colored circles. Image was generated with LigPlot+.

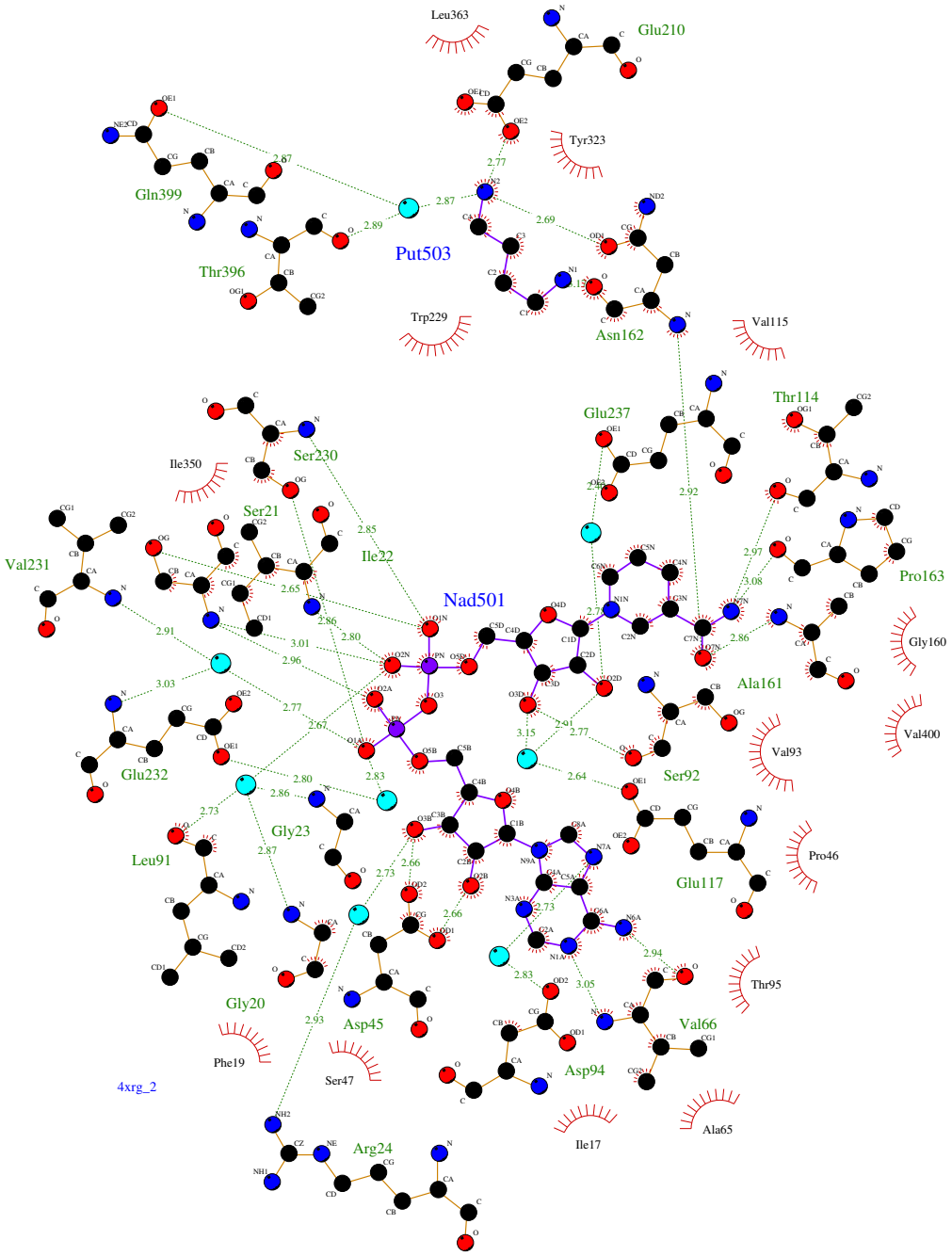

Figure 3.29: Interactions between *Bv*HSS and the ligand PUT. Shown are 2D circle-and-line representations of NAD^+ and the ligand PUT found at the active site together with relevant amino acids of *Bv*HSS variant H296S. The hydrophobic interactions (red spoked arcs) and the hydrogen bonds (green dashed lines with distances in Å) between the amino acids of *Bv*HSS, NAD^+, and PUT (Put503) are shown based on the structures with PDB ID 4XRG with bound PUT (the AGM that alternativly occupies the same position is shown in Fig. 3.28). The atoms presented as circles are color coded: carbon = black, oxygen = red, nitrogen = blue, phosphor = purple. The bonds between ligand atoms are colored in purple and between amino acids colored in orange. Water molecules are represented as cyan colored circles. Image was generated with LigPlot+.

binding of PUT not only at the outer site, but also at the inner site. This can be explained by the effects on the electrostatic potential of the binding pocket surface. Inverting the electrostatic potential around Gln/Glu-237 will destroy the above-described model of the ionic slide und thus completely prevents the entry of PUT into the active site. In comparison with wild-type *Bv*HSS (PDB ID 4PLP), the electron density for the residues of the “track-and-trace” loop is well defined. This indicates a rather rigid conformation of the “track-and-trace” loop and, with it, an extremely narrow and rigid opening of the pore of the binding pocket in the *Bv*HSS variant E237Q in relation to the wild-type *Bv*HSS. Under the assumption that the change of Glu-237 to Gln-237 mimics a fully substrate bound state, most likely through changes in the electrostatic potential, the rigid and narrow conformation of the pore of the binding pocket supports the idea of it also functioning as a locking mechanism directed through a substrate-sensing feature of the “track-and-trace” loop.

3.8 Hypothesis of the Reaction Steps of HSS Catalysis

Based on the substrate-bound structures together with the calculated charge distribution in the binding pocket, we propose the following reaction steps for catalysis under neutral to basic conditions (Fig. 3.30 and Fig. 3.31).

In combination, Glu-237 and Glu-298 transform His-296 into a strong base (calculated pK_a 10). This triad seems to enable the deprotonation of a nearby water shortly before or after the binding of the first PUT molecule within the active site and thereby turning it into an active hydroxide ion (step 1, Fig. 3.30).

Upon the binding of the first PUT molecule at the inner site, repulsion between the positively charged His-296 and protonated amino group of PUT pushes PUT towards the nicotine amide ring of NAD^+, in favor of adopting an oxidation transition-state-like structure. The buildup of positive charge at the nitrogen of PUT at the central site might be stabilized via weak cation-π interaction with the neighboring Trp-229 (step 1 to 2, Fig. 3.30).

A proton transfer from the PUT nitrogen to the hydroxide ion initiates the hydride transfer from PUT carbon C4 to C4N of NAD^+ leaving PUT with a protonated imine at C4 (step 2 to 3, Fig. 3.30).

In accordance with the observed electron density distribution of substrate bound *Bv*HSS, a hydride transition state with a partially aromatic nicotine amid ring and a positive partial charge at PUT carbon C4 seems probable. A near to optimal positioning of PUT carbon C4 (R = 3.5 Å and 0.3 Å off center, see also Fig. 3.25 d) for cation-π interaction with Trp-229 makes it more likely that a positive partial charge occurs at PUT carbon C4 than at the PUT nitrogen (step 4, Fig. 3.30).

In this state, a proton transfer presumably occurs from water to the PUT nitrogen followed by a nucleophilic attack of the water/hydroxide ion oxygen at the electrophilic PUT carbon C4 (step 4 to 5, Fig. 3.30).

Because of the stabilization of the transient build up of a positive partial charge through cation-π stacking at PUT carbon C4, an ammonium ion most probably leaves, resulting in the complete hydrolysis of PUT to 4-aminobutanal (step 6 to 7, Fig. 3.30 and Fig. 3.31).

This 4-aminobutanal might then be activated for nucleophilic attack at carbon C4 by protonation through His-296 and again a stabilization of a positive partial charge at its carbon by Trp-229 (step 7 to 8, Fig. 3.31).

After the entry of a second protonated PUT molecule into the active site, a proton transfer from PUT to His-296 could occur in concert with a nucleophilic attack by the nitrogen free electron pair at 4-aminobutanal carbon C4 (step 8 to 9, Fig. 3.31).

In contrast to the imine at the starting point of the reaction, the positive charge at nitrogen is in addition to the Trp-229 cation-π interaction stabilized by the second carbon chain making it more likely for the hydroxyl group to leave (step 10 to 11, Fig. 3.31).

The resulting protonated Schiff base will then be reduced to HSP by hydride re-transfer from NADH (step 11 to 12, Fig. 3.31), regenerating NAD^+.

Upon leaving the active site, the HSP might be protonated by His-296 at the secondary amine to restore the active site to its initial state (step 12 to 1, Fig. 3.31).

The proposed mechanism is in agreement with a previously postulated less detailed mechanism for HSS (Böttcher *et al.*, 1994; Ober *et al.*, 1996; Tholl *et al.*, 1996). The HSS is able to utilize SPD as substrate to produce HSP and to produce (4-aminobutyl)(5-aminopentyl)amine, (4-aminobutyl)(6-aminohexyl)amine, or (4-aminobutyl)(7-aminheptyl)amine from PUT and respective diamines (Ober et al., 1996). Additionally, HSS does not produce bis(3-aminopropyl)amine or bis(5-aminopentyl)amine from DAP or CAD (Ober *et al.*, 1996; Yamamoto *et al.*, 1993). In contrast to PUT, neither DAP nor CAD have been detected either at a distinct position at the inner binding site or at the outer binding site in *Bv*HSS crystal structures. Instead, only DAP is found to swap potentially between the inner and outer sites without being oxidized. Thus, DAP can compete against PUT for both binding sites explaining its reported competitive inhibitory effect (Ober *et al.*, 1996). The aforementioned HSS products and the observed diamine binding patterns imply a highly specific PUT binding site at the inner site discriminating, via carbon chain length, at which position the redox reaction solely can take place. The outer binding site is probably less specific, and with the adjacent side pocket, it provides enough space for longer diamines. The observed lower conversion rates of diamines with longer carbon chains compared with PUT (Ober *et al.*, 1996) are most likely caused by the less favored binding of the increased hydrophobic parts inside the mainly negatively charged binding pocket. Additionally, the described “ionic slide” probably favors linear molecules with positive charges at approximately 6 Å distance.

All residues proposed to take part in the reaction catalysis and substrate binding (Asn-162, Glu-210, Trp-229, Glu-237, His-296, Glu-298, Tyr-323, and Asp-361) are highly conserved throughout the bacterial HSS family (Shaw *et al.*, 2010) supporting the proposed reaction steps and observed substrate binding sites. The non-functional *Bv*HSS variants E237Q, H296S, and E298Q,

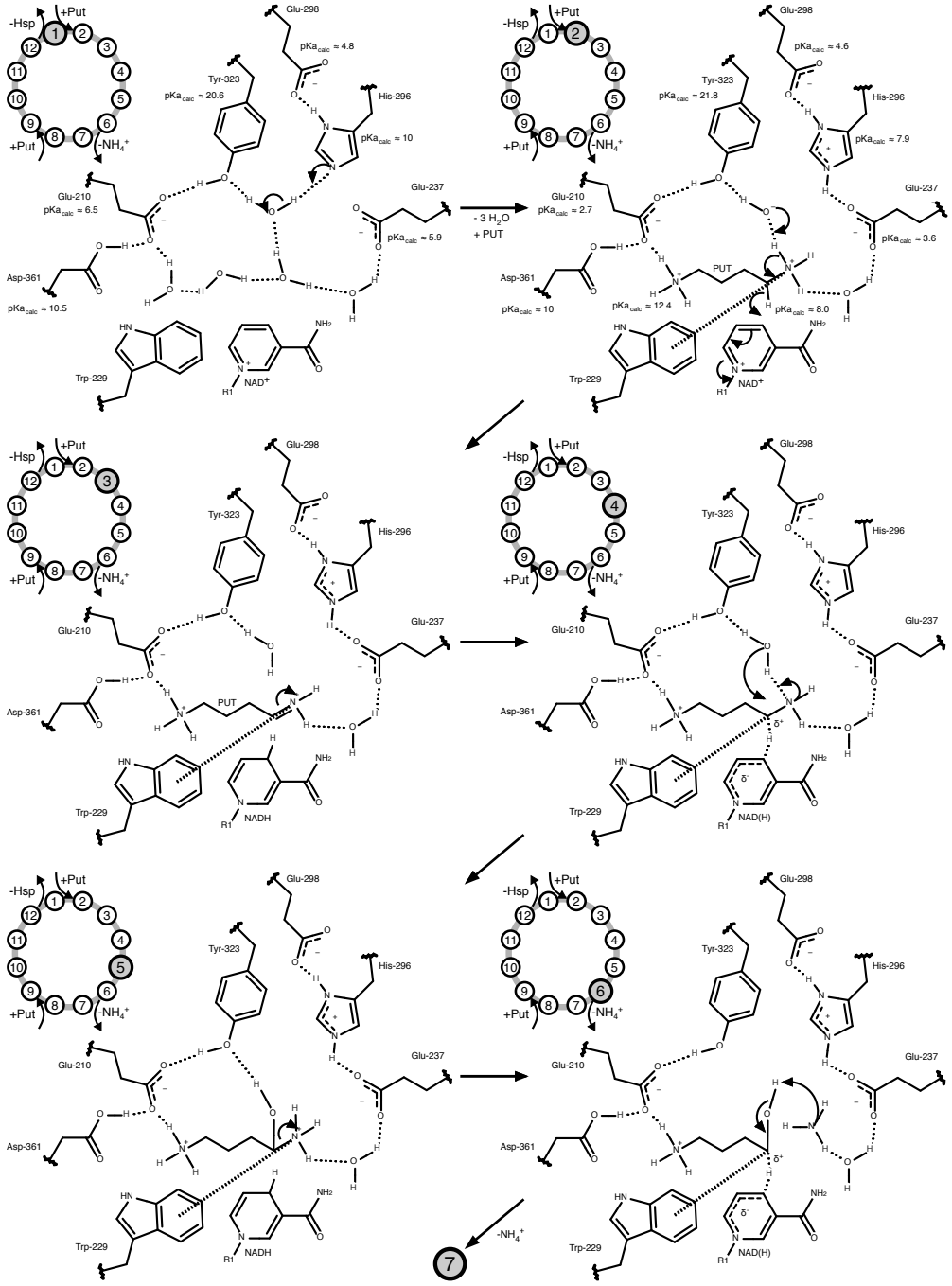

Figure 3.30: First six reaction steps of the proposed bacterial HSS catalyzed formation of HSP from PUT. Relevant residues and NAD(H) of HSS, reaction substrates, intermediates, and product are shown as two-dimensional structure representations (see Figs. 3.14, 3.15, 3.24, and 3.25 for distances and orientation in 3D space). The number of each step is indicated by the highlighted (gray background) number of the abstracted reaction circle in the upper left corner. The $pK_{a,calc}$-values were calculated with the program PROPKA from the respective structures (step 1: *Bv*HSS with PDB ID 4PLP, step 2: *Bv*HSS with PDB ID 4TVB). The cation-π interaction of Trp-229 is indicated by a thick dashed line. Hydrogen bonds are indicated by thin dotted lines. Delocalized electrons/partial bonds are indicated by thin dashed lines.

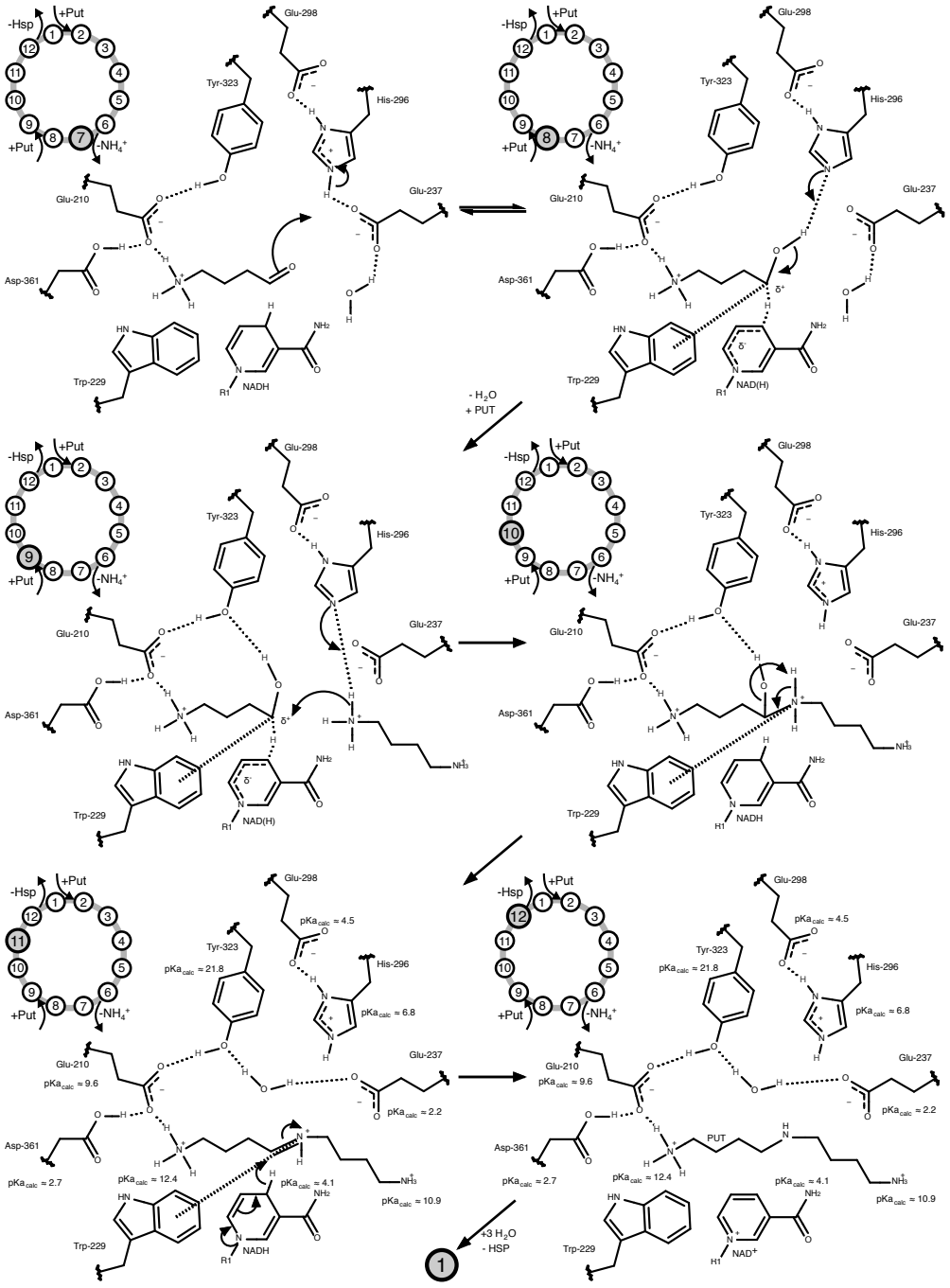

Figure 3.31: Last six reaction steps of the proposed bacterial HSS catalyzed formation of HSP from PUT. Relevant residues and NAD(H) of HSS, reaction substrates, intermediates, and product are shown as two-dimensional structure representations (see Figs. 3.14, 3.15, 3.24, and 3.25 for distances and orientation in 3D space). The number of each step is indicated by the highlighted (gray background) number of the abstracted reaction circle in the upper left corner. The $pK_{a,calc}$-values were calculated with the program PROPKA from the respective structures (steps 11 and 12: *Bv*HSS with PDB ID 4TVB). The cation-π interaction of Trp-229 is indicated by a thick dashed line. Hydrogen bonds are indicated by thin dotted lines. Delocalized electrons/partial bonds are indicated by thin dashed lines.

together with the structural arrangement of Glu-237, His-296, Glu-298, and water molecules (Fig. 3.15 and Fig. 3.24) and the herein calculated pK_a value of approximately 10 for His-296, indicate a general base-catalyzed method of action comparable with that of the catalytic triad in serine protease with a nucleophilic water instead of a serine (Carter and Wells, 1988). The first part of the bacterial HSS-catalyzed reaction can be described as an oxidative deamination, which in part resembles the reaction catalyzed by the structurally nonrelated $NAD(P)^+$-dependent glutamate dehydrogenase (GluDH, EC: 1.4.1.2-4). The reaction meachanism of GluDH from *Clostridium symbiosium* (*Cs*GluDH, PDB ID 1BGV) has been analyzed in detail by Stillman *et al.* (1993) based on its 3D structure. A comparison of the two mechanisms reveals that the proposed deprotonation of the PUT nitrogen by a hydroxide ion is an initial driving force for oxidation at the carbon C4 of PUT. Instead of an aspartate (Asp-165 in *Cs*GluDH), the *Bv*HSS utilizes most probably a well-shielded water/hydroxide ion as a proton acceptor to facilitate substrate oxidation and imine formation. As observed in substrate-bound *Bv*HSS (PDB ID 4TVB), the Glu-237 carboxyl group at a distance of approximately 4.4 Å for each of its oxygens is much too far away from the PUT nitrogen to act as a base like Asp-165 in *Cs*GluDH. As in *Cs*GluDH, the deamination in *Bv*HSS occurs by a nucleophilic attack of a water molecule. The *Cs*GluDH initiates the nucleophilic attack by a proton transfer from Asp-165 to the imine nitrogen, thereby turning the imine carbon into a strong electrophile. The attacking water is activated by a proton transfer from a lysine (Lys-125) (Stillman *et al.*, 1993). The *Bv*HSS lacks corresponding residues and seems to increase the electrophilic properties of PUT carbon C4 by stabilizing a positive partial charge at the carbon through cation-π interaction with Trp-229. This enables proton transfer from water to imine nitrogen followed by nucleophilic attack of the hydroxide ion at the imine carbon. In contrast to the described cation-π interactions, which help to stabilize cationic substrate binding (Sussman *et al.*, 1991; Zhong *et al.*, 1998), observed structural arrangements of *Bv*HSS Trp-229, PUT carbon C4, and PUT nitrogen N2 (PDB ID 4TVB) strongly indicate that cation-π interaction is the key stabilizer of transition states lowering energy barriers and thus favoring the reaction equilibrium towards product formation (compare Fig. 3.30 steps 3 to 6 and Fig. 3.31 steps 8 to 9), as for the cationic cyclization of squalene in steroid biosynthesis (Dougherty, 1996; Morikubo *et al.*, 2006; Wendt *et al.*, 1997), carbocation stabilization in retinal pigment epithelium-specific 65 kDa protein (Redmond *et al.*, 2010), or eudesmane cation stabilization by Trp-334 of aristolochene synthase (Faraldos *et al.*, 2011). The respective carbon (C4 and C05) of both substrates/intermediates found to bind at the active site of *Bv*HSS (PDB ID 4TVB) are approximately positioned over the center of the 6-membered (benzene) ring of the Trp-229 side chain at a distance of 3.5 Å or 3.2 Å. The carbons lie in a near to optimal and much more favored position than the off-centered neighboring nitrogens of the respective molecule (see Fig. 3.25). This supports the hypothesis that, after oxidation and hydrolysis of PUT to 4-aminobutanal, a highly reactive electrophile transition state will be stabilized by cation-π interaction, thus supporting Schiff base formation with a second PUT. In comparison with PUT, the HSP precursor seems to be slightly more “compressed” towards the

inner amino site (Fig. 3.24 a, b and Fig. 3.25). Together with the shorter double bond of the Schiff base compared with a C-N single bond, this results in a re-positioning relative to Trp-229 of the carbon C05 and the nitrogen N06 of the HSP precursor (Fig. 3.25 a and b) compared with the corresponding atoms of PUT (Fig. 3.25 c and d). The nitrogen N06 of the HSP precursor moves from an energetically less favored (R= 4.2 Å, θ = 24.7°, φ = 11.3°) to a more favored (R = 3.5 Å, θ = 15.9°, φ = 41.3°) cation-π interaction site (Marshall *et al.*, 2009) and thus drives Schiff base formation and subsequent reduction (compare Fig. 3.31 steps 10 to 12).

3.8.1 Similarities of the Active Sites of *Bv*HSS and *Mg*SacDH

Of note, the active site of the supposedly evolutionary related eukaryotic saccharopine dehydrogenase/reductase (Shaw *et al.*, 2010) from *M. grisea* (*Mg*SacDH, PDB ID 1E5Q (Johansson *et al.*, 2000)) has substrate, NADPH, and a tryptophan (Trp-174) arranged in a highly similar orientation as their equivalences (PUT/HSP, NAD^+, Trp-229) at the active site of *Bv*HSS (Fig. 3.32). A key step of the proposed mechanism of the enzyme is a Schiff base intermediate (between glutamate and α-aminoadipic-δ-semialdehyde), which is subsequently reduced by NADPH to saccharopine (SHR, forward reaction) (Johansson *et al.*, 2000). Structure alignment of substrate-bound *Bv*HSS (PDB ID 4TVB) and substrate-bound *Mg*SacDH (PDB ID 1E5Q) reveals the tryptophan (Trp-229 of *Bv*HSS and Trp-174 of *Mg*SacDH) as the only conserved or converged amino acid in the vicinity of the active site. The orientation of the planes of the respective tryptophane side chains, as indicated by a green (*Mg*SacDH, Trp-117, Fig. 3.32 a) or a blue (*Bv*HSS, Trp-229, Fig. 3.32 b) plane, towards the plane of the nicotine amide ring of $NAD(P)^+$ are highly similar in both enzymes. In addition, the relative position of the substrates (SHR/HSP, Fig. 3.32) is highly similar in both enzymes. The carbon of SHR, which gets reduced/oxidized during the catalyzed reaction, is placed approximately 3.7 Å over the center of the 6-membred ring of the Trp-174 side chain (corresponding distance in *Bv*HSS: 3.2 Å) and in a distance of approximately 3.7 Å from the "active carbon" of $NADP^+$ (corresponding distance in *Bv*HSS: 2.1 Å) of *Mg*SacDH. Although Johansson *et al.* (2000) did not consider the participation of tryptophan Trp-174 in enzyme catalysis, the described striking resemblances of *Bv*HSS and *Mg*SacDH with regard to their originating from evolutionary distant organisms support the proposed role of tryptophan Trp-229 during the enzyme catalysis of *Bv*HSS.

3.8.2 Similarities of the Active Sites of *Bv*HSS and human DHS

The NAD(H)-dependent human DHS (PDB ID 1RQD (Umland *et al.*, 2004)), capable of producing HSP as a side reaction (Park *et al.*, 2003), possesses some similar structural characteristics of the active site to those of *Bv*HSS (Fig. 3.33). The plane of the tryptophan Trp-327 side chain in DHS is oriented in a comparable mode towards the potential electron transfer sites between NAD^+ and the substrate analog 2-(7-aminoheptyl)guanidine (GC7, Fig. 3.33 a and b). Because a structure of the human DHS with its substrate is not yet known, the actual position of the re-

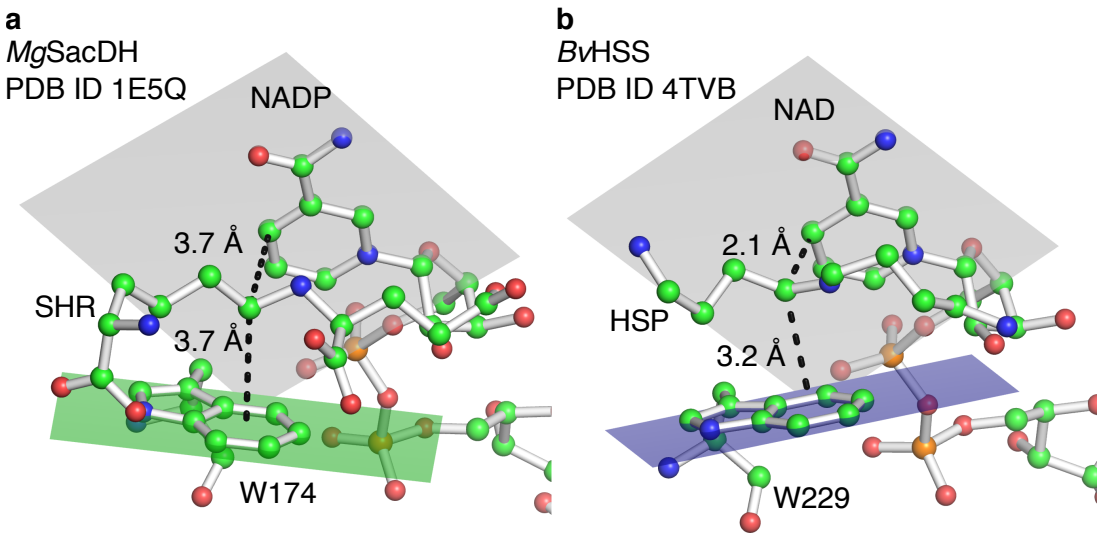

Figure 3.32: Comparison of the active site of *Mg*SacDH (a) and *Bv*HSS (b). Relevant residues (W174/W229), NADP/NAD$^+$, and substrates (SHR/HSP) are shown in ball-and-stick representations. The planes of the nicotinamide ring of NADP/NAD$^+$ are visualized as a grey plane, which are oriented in the same manner in both representations towards the observer. The planes of the tryptophans are shown as green (W174 of *Mg*SacDH) and blue (W229 of *Bv*HSS) planes.

duced/oxidized carbon has to be estimated from the three most likely carbon positions of GC7 (Fig. 3.33 a, as indicated by the 6 distance measurements). This results in a probable position of approximately 3.4-3.7 Å over the center of the 6-membred ring of the Trp-327 side chain, further supporting the proposed key function of tryptophan Trp-229 of *Bv*HSS.
A histidine residue, potentially functioning as general base (Umland *et al.*, 2004), is placed near the electron transfer site and has either the carboxy group of the aspartate Asp-238 or Asp-316 side chain positioned in hydrogen bond distance of one of the histidine side chain nitrogens (depending of the side chain rotation, see Fig. 3.33 c). The orientation of this triad is about the same as that in *Bv*HSS (Glu-237, His-296, Glu-298), with the difference that in *Bv*HSS both nitrogens of the His-296 side chain are positioned in hydrogen bond distance of the respective carboxy group of the glutamate side chain (Fig. 3.33 d).

3.8.3 The Schiff Base Formation at the Active Site of *Bv*HSS

The proposed reaction mechanism of the human DHS and the evolutionary related plant HSS include the formation of a Schiff base between the amino group of the side chain of a lysine residue at the active site and the reaction intermediate 4-aminobutanal (Böttcher *et al.*, 1994; Wolff *et al.*, 1997). Because of the similarity of the net reactions of plant and bacterial HSS a Schiff base formation between a lysine of the bacterial HSS and the 4-aminobutanal appeared possible. Nevertheless, such an enzyme-bound intermediate Schiff base within *Bv*HSS is not possible because of the absence of a lysine residue at the active site of *Bv*HSS imply-

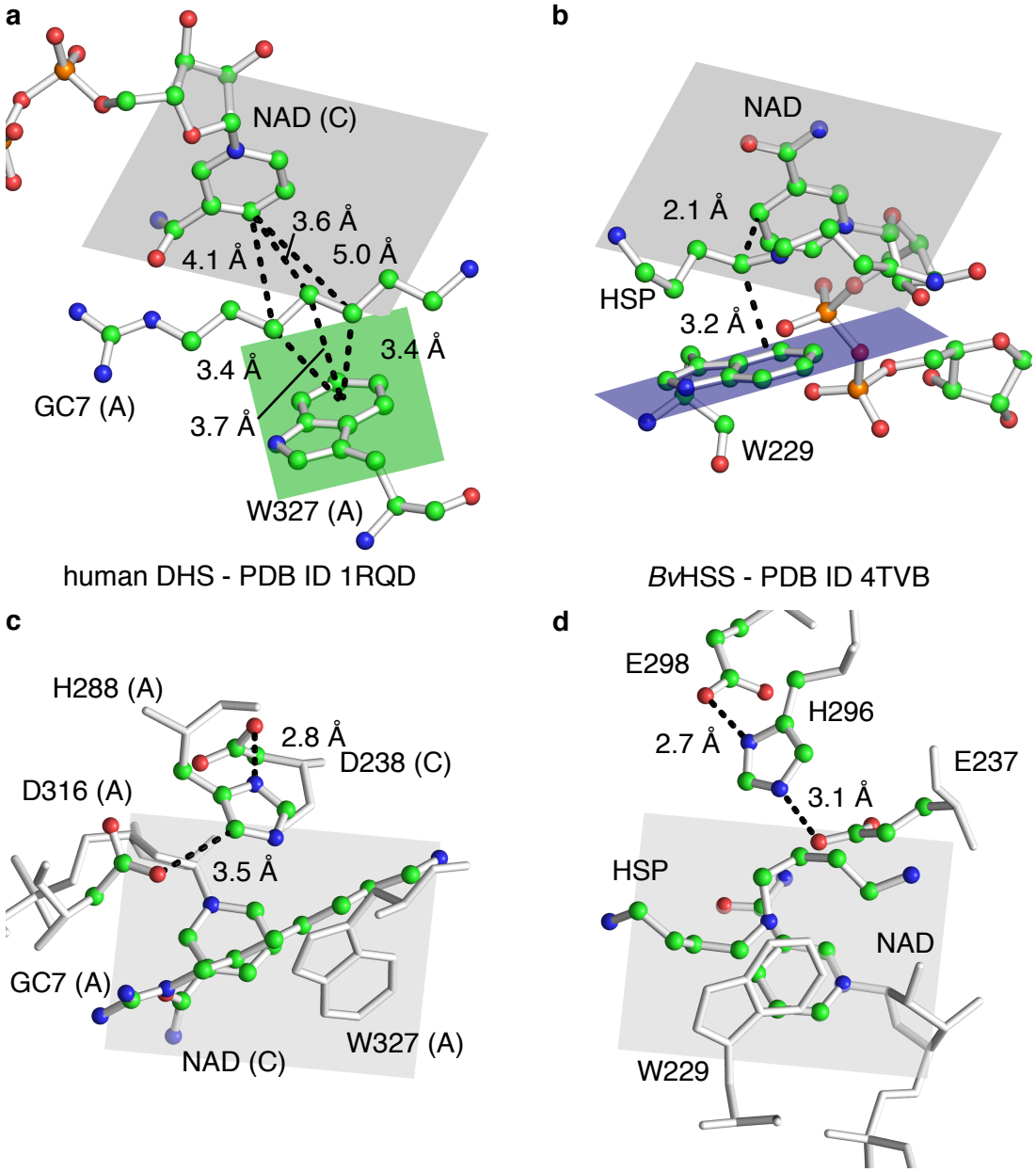

Figure 3.33: Comparison of the active site of human DHS (a, c) and *Bv*HSS (b, d). Relevant residues, NAD^+, and DHS substrate analog 2-(7-aminoheptyl)guanidine (GC7) or HSP are shown in ball-and-stick representations. The active site of human DHS is formed between two subunits (here: A and C). The respective subunit of each shown DHS residue/ligand is given in parentheses. The planes of the nicotinamide ring of NAD^+ are visualized as a grey plane, which are oriented in the same manner in both representations towards the observer. (a, b) The planes of the tryptophans are shown as green (W327 of DHS) and blue (W229 of *Bv*HSS) planes. (c, d) Both enzymes contain a Glu-His-Glu arrangement at the active site, of which the histidine (H288/H296) is oriented towars the substrate (GC7/HSP) in a comparable manner.

ing the distinct handling of the intermediate 4-aminobutanal between bacterial HSS and plant HSS or human DHS, respectively. The presence of an intermediate intramolecular Schiff base forming 3,4-dihydro-2H-pyrrole (five-membered ring) from 4-aminobutanal, as observed under polyamine extraction from *Bv*HSS (Ober *et al.*, 1996), seems unlikely at the active site. Although the binding pocket theoretically provides enough space for a five-membered ring, the well-coordinated amino group at the inner amino-binding site, together with the linearly aligned carbon chain and the occurring ring strain, will prevent intramolecular in favor for intermolecular Schiff base formation. Thus, the 4-aminobutanal present at the inner binding site of the bacterial HSS will most likely immediately form a Schiff base with a diamine present at the outer binding site.

3.9 Conclusion and Outlook

This PhD thesis clearly identifies important residues for substrate binding and enzyme function. The structures provide a solid base for the proposed detailed reaction mechanism. With regard to HSS being considered as a drug target, the results provide a good starting point for *in silico* drug design. A potential drug should at best mimic substrate or transition state in shape and charge. In the case of HSS, the substrate PUT is a small linear, most likely positively charged molecule binding in a linear shape. The proposed intermediates will probably still be linear. As AGM has only been found to bind inside the active site of *Bv*HSS variant H296S, the active site is probably only accessible for linear, unbranched, and positively charged molecules. Because of the high specificity of the inner site for PUT, inhibitors targeting this site have to be similar to PUT. These inhibitors will bind not only to bacterial HSS, but most likely also to any enzyme utilizing PUT, such as eukaryotic DHS and spermidine synthase or plant HSS (Ikeguchi *et al.*, 2006; Ober and Hartmann, 1999a, c). Such a low drug/inhibitor specificity might cause severe cytotoxic site effects by interference with host polyamine metabolism (Pegg and Casero, 2011). Of note, this PhD thesis has identified a side pocket (Fig. 3.9 d and Fig. 3.16) adjacent to the active site that might serve as a more specific inhibitor target, as it is not present in human DHS and is most probably an exclusive feature of bacterial HSS. Nearly all residues forming the side pocket are conserved throughout the bacterial HSS family (Shaw *et al.*, 2010), and some of the side pocket residues participate in the described model of the “ionic slide”. An inhibitor binding in the side pocket could function by blocking substrate trafficking to the active site or it could reach partially into the active site occupying the outer substrate binding site. Additionally, the functional relevant and highly conserved residue Glu-237 is accessible from the side pocket. As demonstrated by non-functional *Bv*HSS variant E237Q and this residues position in direct vicinity of the electron transfer site, (suicide) inhibition might be possible through the modification of this residue. Because of the observed flexible characteristics of the pore at the binding pocket entrance, even larger ring-shaped molecules might not be sterically hindered to enter the side pocket as long as they possess enough positive charges to outbalance their hydrophobicity.
The presented structures and the hereupon proposed reaction meachanism emphasize cation-π

interaction through the conserved tryptophan Trp-229 as a key stabilizer of high energetic transition states. The substitution of the Trp-229 residue with canonical or non-canonical residues to weaken the cation-π interaction and subsequently alter the enzyme kinetic, in analogy to the work of Morikubo *et al.* (2006), Redmond *et al.* (2010) or Faraldos *et al.* (2011), could substatiate this hypothesis. Alternatively, the tryptophan Trp-229 could be replaced by a non-canonical aromatic amino acid that can provide stronger cation-π interaction through introduction of electron donating substituents, like hydroxyl (-OH) or amino (-NH_2) groups. In case of the bacterial HSS such a substitution might be problematic because of the positioning of the respective tryptophan at a narrow area of the active site. Thus, these modifications could result in a blockage of or altering of the charge distribution at the active site and should be verified by the crystal structure of the respective protein. Another approach could be the measurement of changes in the potential absorption at 532 nm of the tryptophane Trp-229 induced by cation-π interaction (Roveri and Braslavsky, 2012) with various substrates, like DAP compared to PUT. To avoid measurement of the interaction of the substrates with other (accessible) tryptophanes of the enzyme, like Trp-4 or Trp-348, substitution of these with for example phenylalanine should be considered.

4 Literature

Afonine, P.V., Grosse-Kunstleve, R.W., Echols, N., Headd, J.J., Moriarty, N.W., Mustyakimov, M., Terwilliger, T.C., Urzhumtsev, A., Zwart, P.H., and Adams, P.D. (2012). Towards automated crystallographic structure refinement with phenix.refine. Acta Crystallogr D Biol Crystallogr *68*, 352-367.

Andi, B., Cook, P.F., and West, A.H. (2006). Crystal structure of the his-tagged saccharopine reductase from Saccharomyces cerevisiae at 1.7-A resolution. Cell biochemistry and biophysics *46*, 17-26.

Baker, N.A., Sept, D., Joseph, S., Holst, M.J., and McCammon, J.A. (2001). Electrostatics of nanosystems: application to microtubules and the ribosome. Proc Natl Acad Sci U S A *98*, 10037-10041.

Beppu, T., Shirahata, A., Takahashi, N., Hosoda, H., and Samejima, K. (1995). Specific depletion of spermidine and spermine in HTC cells treated with inhibitors of aminopropyltransferases. J Biochem *117*, 339-345.

Böttcher, F., Ober, D., and Hartmann, T. (1994). Biosynthesis of Pyrrolizidine Alkaloids - Putrescine and Spermidine Are Essential Substrates of Enzymatic Homospermidine Formation. Can J Chem *72*, 80-85.

Brändén, C.I., and Jones, T.A. (1990). Between Objectivity and Subjectivity. Nature *343*, 687-689.

Brünger, A.T. (1992). Free R-Value - a Novel Statistical Quantity for Assessing the Accuracy of Crystal-Structures. Nature *355*, 472-475.

Byers, T.L., Wiest, L., Wechter, R.S., and Pegg, A.E. (1993). Effects of Chronic 5'-([(Z)-4-Amino-2-Butenyl]Methylamino)-5'-Deoxy-Adenosine (Abeado) Treatment on Polyamine and Eif-5a Metabolism in Abeado-Sensitive and Abeado-Resistant L1210 Murine Leukemia-Cells. Biochem J *290*, 115-121.

Carter, P., and Wells, J.A. (1988). Dissecting the Catalytic Triad of a Serine Protease. Nature *332*, 564-568.

Casero, R.A., Jr., and Marton, L.J. (2007). Targeting polyamine metabolism and function in cancer and other hyperproliferative diseases. Nat Rev Drug Discov *6*, 373-390.

Cromer, D.T., and Mann, J.B. (1968). X-ray scattering factors computed from numerical Hartree–Fock wave functions. Acta Crystallogr A *24*, 321-324.

de Beer, T.A., Berka, K., Thornton, J.M., and Laskowski, R.A. (2014). PDBsum additions. Nucleic Acids Res *42*, D292-296.

Di Martino, M.L., Campilongo, R., Casalino, M., Micheli, G., Colonna, B., and Prosseda, G. (2013). Polyamines: emerging players in bacteria-host interactions. Int J Med Microbiol *303*, 484-491.

Diederichs, K., and Karplus, P.A. (1997). Improved R-factors for diffraction data analysis in macromolecular crystallography. Nat Struct Biol *4*, 269-275.

Dolinsky, T.J., Czodrowski, P., Li, H., Nielsen, J.E., Jensen, J.H., Klebe, G., and Baker, N.A. (2007). PDB2PQR: expanding and upgrading automated preparation of biomolecular structures for molecular simulations. Nucleic Acids Res *35*, W522-525.

Dougherty, D.A. (1996). Cation-pi interactions in chemistry and biology: a new view of benzene, Phe, Tyr, and Trp. Science *271*, 163-168.

Dougherty, D.A. (2013). The cation-pi interaction. Acc Chem Res *46*, 885-893.

Emsley, P., Lohkamp, B., Scott, W.G., and Cowtan, K. (2010). Features and development of Coot. Acta Crystallogr D Biol Crystallogr *66*, 486-501.

Evans, P.R. (2011). An introduction to data reduction: space-group determination, scaling and intensity statistics. Acta Crystallogr D Biol Crystallogr *67*, 282-292.

Faraldos, J.A., Antonczak, A.K., Gonzalez, V., Fullerton, R., Tippmann, E.M., and Allemann, R.K. (2011). Probing eudesmane cation-pi interactions in catalysis by aristolochene synthase with non-canonical amino acids. J Am Chem Soc *133*, 13906-13909.

Forouhar, F., Hussain, M., Seetharaman, J., Fang, Y., Janjua, H., Xiao, R., Cunningham, K., Ma, L-C., Owens, L., Liu, J., Baran, M.C., Acton, T.B., Montelione, G.T., Hunt, J.F., Tong, L. Crystal

structure of the homospermidine synthase hss from Legionella pneumophila in complex with NAD. To be Published.

Gallivan, J.P., and Dougherty, D.A. (2000). A Computational Study of Cation-π Interactions vs Salt Bridges in Aqueous Media: Implications for Protein Engineering. J Am Chem Soc *122*, 870-874.

Green, D.W., Ingram, V.M., and Perutz, M.F. (1954). The Structure of Haemoglobin. IV. Sign Determination by the Isomorphous Replacement Method. Proc R Soc A *225*, 287-307.

Hamana, K., and Matsuzaki, S. (1992). Polyamines as a chemotaxonomic marker in bacterial systematics. Crit Rev Microbiol *18*, 261-283.

Hamana, K., Sato, W., Gouma, K., Yu, J., Ino, Y., Umemura, Y., Mochizuki, C., Takatsuka, K., Kigure, Y., Tanaka, N.*, et al.* (2007). Cellular Polyamine Catalogues of the Five Classes of the Phylum Proteobacteria: Distributions of Homospermidine within the Class Alphaproteobacteria, Hydroxyputrescine within the Class Betaproteobacteria, Norspermidine within the Class Gammaproteobacteria, and Spermine within the Classes Deltaproteobacteria and Epsilonproteobacteria. Ann Gunma Health Sci *27*, 1-16.

Hamana, K., and Takeuchi, M. (1998). Polyamine Profiles as Chemotaxonomic Marker within Alpha, Beta, Gamma, Delta, and Epsilon Subclasses of Class Proteobacteria: Distribution of 2-Hydroxyputrescine and Homospermidine. Microbiol Cult Coll *14*, 1-14.

Hanfrey, C.C., Pearson, B.M., Hazeldine, S., Lee, J., Gaskin, D.J., Woster, P.M., Phillips, M.A., and Michael, A.J. (2011). Alternative spermidine biosynthetic route is critical for growth of Campylobacter jejuni and is the dominant polyamine pathway in human gut microbiota. J Biol Chem *286*, 43301-43312.

Hendrickson, W.A. (1991). Determination of macromolecular structures from anomalous diffraction of synchrotron radiation. Science *254*, 51-58.

Ho, B.K., and Gruswitz, F. (2008). HOLLOW: generating accurate representations of channel and interior surfaces in molecular structures. Bmc Struct Biol *8*, 49.

Hodel, A., Kim, S.H., and Brünger, A.T. (1992). Model bias in macromolecular crystal structures. Acta Crystallographica Section A Foundations of Crystallography *48*, 851-858.

Holm, I., Persson, L., Pegg, A.E., and Heby, O. (1989). Effects of S-Adenosyl-1,8-Diamino-3-Thio-Octane and S-Methyl-5'-Methylthioadenosine on Polyamine Synthesis in Ehrlich Ascites-Tumor Cells. Biochem J *261*, 205-210.

Ikeguchi, Y., Bewley, M.C., and Pegg, A.E. (2006). Aminopropyltransferases: function, structure and genetics. J Biochem *139*, 1-9.

IUCr (2006). International Tables for Crystallography Volume C: Mathematical, physical and chemical tables, Volume C, First online edition (International Union of Crystallography).

Jefferies, J.M., Cooper, T., Yam, T., and Clarke, S.C. (2012). Pseudomonas aeruginosa outbreaks in the neonatal intensive care unit–a systematic review of risk factors and environmental sources. J Med Microbiol *61*, 1052-1061.

Johansson, E., Steffens, J.J., Lindqvist, Y., and Schneider, G. (2000). Crystal structure of saccharopine reductase from Magnaporthe grisea, an enzyme of the alpha-aminoadipate pathway of lysine biosynthesis. Structure *8*, 1037-1047.

Jones, T.A., Zou, J.Y., Cowan, S.W., and Kjeldgaard, M. (1991). Improved methods for building protein models in electron density maps and the location of errors in these models. Acta Crystallographica Section A Foundations of Crystallography *47*, 110-119.

Kabsch, W. (2010). Xds. Acta Crystallogr D Biol Crystallogr *66*, 125-132.

Kaltenegger, E., Eich, E., and Ober, D. (2013). Evolution of homospermidine synthase in the convolvulaceae: a story of gene duplication, gene loss, and periods of various selection pressures. Plant Cell *25*, 1213-1227.

Karplus, P.A., and Diederichs, K. (2012). Linking crystallographic model and data quality. Science *336*, 1030-1033.

Kelley, L.A., and Sternberg, M.J. (2009). Protein structure prediction on the Web: a case study using the Phyre server. Nat Protoc *4*, 363-371.

Kendrew, J.C., Bodo, G., Dintzis, H.M., Parrish, R.G., Wyckoff, H., and Phillips, D.C. (1958). A Three-Dimensional Model of the Myoglobin Molecule Obtained by X-Ray Analysis. Nature *181*, 662-666.

Kleywegt, G.J., Harris, M.R., Zou, J.Y., Taylor, T.C., Wahlby, A., and Jones, T.A. (2004). The Uppsala Electron-Density Server. Acta Crystallogr D Biol Crystallogr *60*, 2240-2249.

Laemmli, U.K. (1970). Cleavage of structural proteins during the assembly of the head of bacteriophage T4. Nature *227*, 680-685.

Laskowski, R.A., and Swindells, M.B. (2011). LigPlot+: multiple ligand-protein interaction diagrams for drug discovery. J Chem Inf Model *51*, 2778-2786.

Lee, J., Sperandio, V., Frantz, D.E., Longgood, J., Camilli, A., Phillips, M.A., and Michael, A.J. (2009). An alternative polyamine biosynthetic pathway is widespread in bacteria and essential for biofilm formation in Vibrio cholerae. J Biol Chem *284*, 9899-9907.

Lunin, V.Y. (1988). Use of the information on electron density distribution in macromolecules. Acta Crystallographica Section A Foundations of Crystallography *44*, 144-150.

Ma, J.C., and Dougherty, D.A. (1997). The Cation-π Interaction. Chem Rev *97*, 1303-1324.

Main, P. (1979). A theoretical comparison of the β,γ' and 2Fo–Fc syntheses. Acta Crystallographica Section A: Crystal Physics, Diffraction, Theoretical and General Crystallography *35*, 779-785.

Marshall, M.S., Steele, R.P., Thanthiriwatte, K.S., and Sherrill, C.D. (2009). Potential energy curves for cation-pi interactions: off-axis configurations are also attractive. J Phys Chem A *113*, 13628-13632.

Matthews, B.W. (1966). The extension of the isomorphous replacement method to include anomalous scattering measurements. Acta Crystallogr *20*, 82-86.

Mecozzi, S., West, A.P., and Dougherty, D.A. (1996). Cation-π Interactions in Simple Aromatics: Electrostatics Provide a Predictive Tool. J Am Chem Soc *118*, 2307-2308.

Metcalf, B.W., Bey, P., Danzin, C., Jung, M.J., Casara, P., and Vevert, J.P. (1978). Catalytic Irreversible Inhibition of Mammalian Ornithine Decarboxylase (E C 4 1 1 17) by Substrate and Product Analogs. J Am Chem Soc *100*, 2551-2553.

Mooij, W.T., Cohen, S.X., Joosten, K., Murshudov, G.N., and Perrakis, A. (2009). "Conditional Restraints": Restraining the Free Atoms in ARP/wARP. Structure *17*, 183-189.

Morikubo, N., Fukuda, Y., Ohtake, K., Shinya, N., Kiga, D., Sakamoto, K., Asanuma, M., Hirota, H., Yokoyama, S., and Hoshino, T. (2006). Cation-pi interaction in the polyolefin cyclization cascade uncovered by incorporating unnatural amino acids into the catalytic sites of squalene cyclase. J Am Chem Soc *128*, 13184-13194.

Morimoto, N., Fukuda, W., Nakajima, N., Masuda, T., Terui, Y., Kanai, T., Oshima, T., Imanaka, T., and Fujiwara, S. (2010). Dual biosynthesis pathway for longer-chain polyamines in the hyperthermophilic archaeon Thermococcus kodakarensis. J Bacteriol *192*, 4991-5001.

Murshudov, G.N., Vagin, A.A., and Dodson, E.J. (1997). Refinement of macromolecular structures by the maximum-likelihood method. Acta Crystallogr D Biol Crystallogr *53*, 240-255.

Nasrallah, G.K., Riveroll, A.L., Chong, A., Murray, L.E., Lewis, P.J., and Garduno, R.A. (2011). Legionella pneumophila requires polyamines for optimal intracellular growth. J Bacteriol *193*, 4346-4360.

Nikaido, H. (2009). Multidrug resistance in bacteria. Annu Rev Biochem *78*, 119-146.

Nowotarski, S.L., Woster, P.M., and Casero, R.A., Jr. (2013). Polyamines and cancer: implications for chemotherapy and chemoprevention. Expert Rev Mol Med *15*, e3.

Ober, D., and Hartmann, T. (1999a). Deoxyhypusine synthase from tobacco. cDNA isolation, characterization, and bacterial expression of an enzyme with extended substrate specificity. J Biol Chem *274*, 32040-32047.

Ober, D., and Hartmann, T. (1999c). Homospermidine synthase, the first pathway-specific enzyme of pyrrolizidine alkaloid biosynthesis, evolved from deoxyhypusine synthase. Proc Natl Acad Sci U S A *96*, 14777-14782.

Ober, D., Tholl, D., Martin, W., and Hartmann, T. (1996). Homospermidine synthase of Rhodopseudomonas viridis: Substrate specificity and effects of the heterologously expressed

enzyme on polyamine metabolism of Escherichia coli. The Journal of General and Applied Microbiology *42*, 411-419.

Ohnuma, M., Terui, Y., Tamakoshi, M., Mitome, H., Niitsu, M., Samejima, K., Kawashima, E., and Oshima, T. (2005). N1-aminopropylagmatine, a new polyamine produced as a key intermediate in polyamine biosynthesis of an extreme thermophile, Thermus thermophilus. J Biol Chem *280*, 30073-30082.

Park, J.H., Wolff, E.C., Folk, J.E., and Park, M.H. (2003). Reversal of the deoxyhypusine synthesis reaction. Generation of spermidine or homospermidine from deoxyhypusine by deoxyhypusine synthase. J Biol Chem *278*, 32683-32691.

Parkins, M.D., Gregson, D.B., Pitout, J.D., Ross, T., and Laupland, K.B. (2010). Population-based study of the epidemiology and the risk factors for Pseudomonas aeruginosa bloodstream infection. Infection *38*, 25-32.

Patterson, A.L. (1934). A Fourier Series Method for the Determination of the Components of Interatomic Distances in Crystals. Physical Review *46*, 372-376.

Pegg, A.E. (2009). Mammalian polyamine metabolism and function. Iubmb Life *61*, 880-894.

Pegg, A.E., and Casero, R.A., Jr. (2011). Current status of the polyamine research field. Methods in molecular biology *720*, 3-35.

Pegg, A.E., Tang, K.C., and Coward, J.K. (1982). Effects of S-adenosyl-1,8-diamino-3-thiooctane on polyamine metabolism. Biochemistry *21*, 5082-5089.

Pegg, A.E., Wechter, R., Poulin, R., Woster, P.M., and Coward, J.K. (1989). Effect of S-adenosyl-1,12-diamino-3-thio-9-azadodecane, a multisubstrate adduct inhibitor of spermine synthase, on polyamine metabolism in mammalian cells. Biochemistry *28*, 8446-8453.

Porter, C.W., Dworaczyk, D., Ganis, B., and Weiser, M.M. (1980). Polyamines and biosynthetic enzymes in the rat intestinal mucosa and the influence of methylglyoxal-bis(guanylhydrazone). Cancer Res *40*, 2330-2335.

Potterton, E., Briggs, P., Turkenburg, M., and Dodson, E. (2003). A graphical user interface to the CCP4 program suite. Acta Crystallogr D Biol Crystallogr *59*, 1131-1137.

Raju, R.K., Bloom, J.W., An, Y., and Wheeler, S.E. (2011). Substituent effects on non-covalent interactions with aromatic rings: insights from computational chemistry. Chemphyschem *12*, 3116-3130.

Ramachandran, G.N., Ramakrishnan, C., and Sasisekharan, V. (1963). Stereochemistry of polypeptide chain configurations. J Mol Biol *7*, 95-99.

Read, R.J. (1986). Improved Fourier coefficients for maps using phases from partial structures with errors. Acta Crystallographica Section A Foundations of Crystallography *42*, 140-149.

Read, R.J., Adams, P.D., Arendall, W.B., 3rd, Brunger, A.T., Emsley, P., Joosten, R.P., Kleywegt, G.J., Krissinel, E.B., Lutteke, T., Otwinowski, Z.*, et al.* (2011). A new generation of crystallographic validation tools for the protein data bank. Structure *19*, 1395-1412.

Redmond, T.M., Poliakov, E., Kuo, S., Chander, P., and Gentleman, S. (2010). RPE65, visual cycle retinol isomerase, is not inherently 11-cis-specific: support for a carbocation mechanism of retinol isomerization. J Biol Chem *285*, 1919-1927.

Regenass, U., Mett, H., Stanek, J., Mueller, M., Kramer, D., and Porter, C.W. (1994). CGP 48664, a new S-adenosylmethionine decarboxylase inhibitor with broad spectrum antiproliferative and antitumor activity. Cancer Res *54*, 3210-3217.

Reimann, A., Nurhayati, N., Backenkohler, A., and Ober, D. (2004). Repeated evolution of the pyrrolizidine alkaloid-mediated defense system in separate angiosperm lineages. Plant Cell *16*, 2772-2784.

Roveri, O.A., and Braslavsky, S.E. (2012). π-Cation interactions as the origin of the weak absorption at 532 nm observed in tryptophan-containing polypeptides. Photochemical & Photobiological Sciences *11*, 962-966.

Rupp, B. (2010). Biomolecular crystallography (Garland Science, Taylor & Francis Group, LLC).

Schneider, J., and Wendisch, V.F. (2011). Biotechnological production of polyamines by bacteria: recent achievements and future perspectives. Appl Microbiol Biotechnol *91*, 17-30.

Schrodinger, LLC (2010). The PyMOL Molecular Graphics System, Version 1.3r1.

Shah, P., and Swiatlo, E. (2008). A multifaceted role for polyamines in bacterial pathogens. Mol Microbiol *68*, 4-16.

Shaw, F.L., Elliott, K.A., Kinch, L.N., Fuell, C., Phillips, M.A., and Michael, A.J. (2010). Evolution and multifarious horizontal transfer of an alternative biosynthetic pathway for the alternative polyamine sym-homospermidine. J Biol Chem *285*, 14711-14723.

Sheldrick, G.M. (1990). Phase annealing in SHELX-90: direct methods for larger structures. Acta Crystallographica Section A Foundations of Crystallography *46*, 467-473.

Sillitoe, I., Cuff, A.L., Dessailly, B.H., Dawson, N.L., Furnham, N., Lee, D., Lees, J.G., Lewis, T.E., Studer, R.A., Rentzsch, R.*, et al.* (2013). New functional families (FunFams) in CATH to improve the mapping of conserved functional sites to 3D structures. Nucleic Acids Res *41*, D490-498.

Søndergaard, C.R., Olsson, M.H.M., Rostkowski, M., and Jensen, J.H. (2011). Improved Treatment of Ligands and Coupling Effects in Empirical Calculation and Rationalization of pKaValues. J Chem Theory Comput *7*, 2284-2295.

Stillman, T.J., Baker, P.J., Britton, K.L., and Rice, D.W. (1993). Conformational flexibility in glutamate dehydrogenase. Role of water in substrate recognition and catalysis. J Mol Biol *234*, 1131-1139.

Sussman, J.L., Harel, M., Frolow, F., Oefner, C., Goldman, A., Toker, L., and Silman, I. (1991). Atomic structure of acetylcholinesterase from Torpedo californica: a prototypic acetylcholine-binding protein. Science *253*, 872-879.

Tait, G.H. (1976). A new pathway for the biosynthesis of spermidine. Biochem Soc Trans *4*, 610-612.

Tait, G.H. (1979). The formation of homospermidine by an enzyme from Rhodopseudomonas viridis [proceedings]. Biochem Soc Trans *7*, 199-201.

Terwilliger, T.C., Grosse-Kunstleve, R.W., Afonine, P.V., Moriarty, N.W., Adams, P.D., Read, R.J., Zwart, P.H., and Hung, L.W. (2008). Iterative-build OMIT maps: map improvement by iterative model building and refinement without model bias. Acta Crystallogr D Biol Crystallogr *64*, 515-524.

Tholl, D., Ober, D., Martin, W., Kellermann, J., and Hartmann, T. (1996). Purification, molecular cloning and expression in Escherichia coli of homospermidine synthase from Rhodopseudomonas viridis. Eur J Biochem *240*, 373-379.

Umland, T.C., Wolff, E.C., Park, M.H., and Davies, D.R. (2004). A new crystal structure of deoxyhypusine synthase reveals the configuration of the active enzyme and of an enzyme.NAD.inhibitor ternary complex. J Biol Chem *279*, 28697-28705.

Vagin, A., and Teplyakov, A. (1997). MOLREP: an Automated Program for Molecular Replacement. Journal of Applied Crystallography *30*, 1022-1025.

Vorobiev, S., Su, M., Seetharaman, J., Maglaqui, M., Xiao, R., Kohan, E., Wang, D., Everett, J.K., Acton, T.B., Montelione, G.T., Tong, L., Hunt, J.F. Crystal Structure of the Q7MSS8_WOLSU protein from Wolinella succinogenes. To be Published.

Wallace, H.M., and Fraser, A.V. (2004). Inhibitors of polyamine metabolism: review article. Amino Acids *26*, 353-365.

Wang, B.C. (1985). Resolution of phase ambiguity in macromolecular crystallography. Methods Enzymol *115*, 90-112.

Wang, J., Cieplak, P., and Kollman, P.A. (2000). How well does a restrained electrostatic potential (RESP) model perform in calculating conformational energies of organic and biological molecules? J Comput Chem *21*, 1049-1074.

Weiss, M.S. (2001). Global indicators of X-ray data quality. Journal of Applied Crystallography *34*, 130-135.

Weiss, T., Bernhardt, G., Buschauer, A., Jauch, K.W., and Zirngibl, H. (1997). High-resolution reversed-phase high-performance liquid chromatography analysis of polyamines and their monoacetyl conjugates by fluorescence detection after derivatization with N-hydroxysuccinimidyl 6-quinolinyl carbamate. Anal Biochem *247*, 294-304.

Wendt, K.U., Poralla, K., and Schulz, G.E. (1997). Structure and function of a squalene cyclase. Science *277*, 1811-1815.

Wolff, E.C., Folk, J.E., and Park, M.H. (1997). Enzyme-Substrate Intermediate Formation at Lysine 329 of Human Deoxyhypusine Synthase. J Biol Chem *272*, 15865-15871.

Yamamoto, S., Nagata, S., and Kusaba, K. (1993). Purification and Characterization of Homospermidine Synthase in Acinetobacter-Tartarogenes Atcc-31105. J Biochem-Tokyo *114*, 45-49.

Yong, K., Zhang, J., and Main, P. (1990). Histogram Matching as a New Density Modification Technique for Phase Refinement and Extension of Protein Molecules. Acta Crystallogr A *46*, 41-46.

Zhong, W., Gallivan, J.P., Zhang, Y., Li, L., Lester, H.A., and Dougherty, D.A. (1998). From ab initio quantum mechanics to molecular neurobiology: a cation-pi binding site in the nicotinic receptor. Proc Natl Acad Sci U S A *95*, 12088-12093.

Zilberberg, M.D., and Shorr, A.F. (2013). Prevalence of multidrug-resistant Pseudomonas aeruginosa and carbapenem-resistant Enterobacteriaceae among specimens from hospitalized patients with pneumonia and bloodstream infections in the United States from 2000 to 2009. J Hosp Med *8*, 559-563.